Technische Universität Braunschweig

emg

Rahmondia Nanda Setiadi

Fluxgate Impedance Analyzer for Sensitivity and Noise Properties

Dissertation
Braunschweig 2018

Berichte aus dem **Institut für Elektrische Messtechnik und Grundlagen der Elektrotechnik**

Band **63**

Hrsg. Prof. Dr. Meinhard Schilling

Fluxgate Impedance Analyzer for Sensitivity and Noise Properties

Von der Fakultät für Elektrotechnik, Informationstechnik, Physik
der Technischen Universität Carolo-Wilhelmina zu Braunschweig

zur Erlangung des Grades eines Doktors

der Ingenieurwissenschaften (Dr.-Ing.)

genehmigte Dissertation

von Rahmondia Nanda Setiadi

aus Pekanbaru, Indonesien

eingereicht am: 25.06.2018

mündliche Prüfung am: 10.10.2018

1. Referent: Prof. Dr. rer. nat. Meinhard Schilling
2. Referent: apl. Prof. Dr. rer. nat. Frank Ludwig

Druckjahr: 2019

Dissertation an der Technischen Universität Braunschweig,
Fakultät für Elektrotechnik, Informationstechnik, Physik

Kurzfassung

Der Fluxgate-Sensor ist als präziser, rauscharmer, zuverlässiger Magnetfeldsensor bekannt, und wird seit Jahrzehnten entwickelt. Der Sensor wurde in Messsystemen verwendet, die eine hohe Präzision bei Magnetfeldmessungen erfordern, beispielsweise bei Satellitensystemen, bei der Navigation und bei der geologischen Erkundung. Obwohl für das Fluxgate viele Konkurrenten wie Hall-, GMR- und AMR-Sensoren vorhanden sind, wird die Entwicklung an Fluxgates für eine bessere Performance weiter geführt. Es gibt noch viele mögliche Entwicklungen an Fluxgate-Sensoren, um sie besser zu machen als die, die heutzutage kommerziell erhältlich sind. Das wichtigste und größte Potenzial ist die Verbesserung der Empfindlichkeits- und Rauscheigenschaften. Viele Anstrengungen wurden unternommen, um dies zu erreichen, wie eine Bearbeitung des Kernmaterials, ein Abstimmen der Spulen, ein neues Modell der Ausgangsspannung, die die Kernpermeabilität oder Spuleninduktivität beinhaltet, und die Optimierung der Elektroniksignalverarbeitung. Das neue Modell soll die gute Permeabilität, Induktivität oder andere Parameter für die beste Empfindlichkeit und Rauschleistung durch die Gestaltung der Geometrie enthalten.

Diese Arbeit beschreibt die Entwicklung eines neuartigen Fluxgate-Analysators zur Fluxgate-Sensorcharakterisierung. Dieser wird zur Modellierung des Fluxgate-Sensorausgangs verwendet, um die Parameter zu untersuchen, die den Fluxgate-Sensorausgang beeinflussen. Die Charakterisierung basiert auf der Impedanz von Fluxgate-Sensorspulen, die als Fluxgate-Sensorkern hochpermeables Material enthalten. Die Nichtlinearität der Kernpermeabilität wird zum entscheidenden und wichtigen Thema beim Entwurf des Impedanzanalysators. Das Gerät wurde so entwickelt, dass es den Eigenschaften des Fluxgate-Sensors entspricht, der eine niedrige Impedanz und eine hohe Kernpermeabilität aufweist. Aus diesem Grund wurde der Fluxgate-Analysator mit einer niedrigen Ausgangsimpedanz entworfen und kann einen sehr niedrigen Strom für die Fluxgate-Impedanzmessung bereitstellen. Ein Modell aus der Impedanzmessung wird verwendet, um die Fluxgate-Ausgangsempfindlichkeit zu berechnen und vorherzusagen. Zusammen mit anderen physikalischen Parametern wie Wicklungszahlen und -länge wird das Modell verwendet, um eine Gleichung zur Berechnung der Fluxgate-Ausgangsspannung und -empfindlichkeit zu erstellen.

Abstract

The fluxgate sensor is known as a precision, low noise, reliable magnetic field sensor, and has been developed for decades. The sensor has been used in measurement systems, which need high precision in magnetic field measurements such as in satellite systems, navigation, and geological exploration. Although there are lots of competitors to the fluxgate such as Hall, GMR, and AMR sensors, the development of fluxgate sensors is still continuing to get better performance. There are still many potential developments of fluxgate sensors, to make it better than what is nowadays commercially available. The main big potential is the development of sensitivity and noise properties. Many efforts have been done to obtain this such as treatment of the core material, tuning the coils, making a new model of output voltage involving the core permeability or coil inductance, and the electronics signal processing optimization. The new model is intended to obtain the good permeability, inductance, or any other parameters for the best sensitivity and noise performance by designing the geometry.

This thesis describes the development of a novel fluxgate analyzer for fluxgate sensor characterization, which is used for modeling the fluxgate sensor output to study the parameters that affect fluxgate sensor output. The characterization is based on the impedance of fluxgate sensor coils, which contain high permeability material as fluxgate sensor core. The non-linearity of the core permeability becomes the crucial and important topic in designing the impedance analyzer. The instrument has been designed to comply with the fluxgate sensor characteristics, which has low impedance and high core permeability. For that reason, the fluxgate analyzer has been designed with low output impedance and to be able to provide a very low current for fluxgate impedance measurement. A model from the impedance measurement is used to calculate and predict the fluxgate output sensitivity. Together with other physical parameters such as winding number and length, the model is utilized to set-up an equation to calculate the fluxgate output voltage and sensitivity.

Acknowledgements / Thanks

This dissertation would not have been possible without the guidance of my supervisors Professors Meinhard Schilling and Frank Ludwig. I am also indebted for the contributions of a great many people including: Felix Nording, Sebastian Draack, Jan Dieckhoff, Harald Schmidt, Kerstin Franke, Tanja Coenen, Ralf Behme, and Gabriela Kurbach.

I would like to acknowledge the Directorate General of Resources for Science, Technology and Higher Education - Ministry of Research, Technology and Higher Education of Indonesia for their financial support and Braunschweig International Graduate School of Metrology (B-IGSM).

My deepest gratitude goes to my family: my wife Risa Andriani, my son Muhammad Rafif Al Hadziq, my father Dasril, my mother Nurbaity. I would never have finished without their help and encouragement.

Glossary

AC	alternating current
ADC	analog to digital converter
AI	analog input
AMR	anisotropic magneto-resistance
AO	analog output
BJT	bipolar junction transistor
CMOS	complementary metal oxide semiconductor
DAC	digital to analog converter
DAQ	data acquisition
DC	direct current
DUT	device under test
EMF	electromotive force
EMG	Institute for Electrical Measurement Science and Fundamental Electrical Engineering
FG	fluxgate
FGM	fluxgate magnetometer
GBW	gain bandwidth product
GMI	giant magneto-impedance
GMR	giant magneto-resistance
GPS	global positioning system
IC	integrated circuit
LPF	low-pass filter
MAD	magnetic anomaly detector

MEG	magneto-encephalography
MEMS	micro-electro-mechanical sensor
MFL	magnetic flux leakage
MMF	magnetomotive force
MOSFET	metal-oxide-semiconductor field-effect transistor
MRI	magnetic resonance imaging
MT	magneto-telluric
NI	National Instruments
ODE	ordinary differential equation
Op-amp	operational amplifier
PA	power amplifier
PC	personal computer
PCB	printed circuit board
PSD	phase sensitive detector
PVC	polyvinyl chloride
SNR	signal-to-noise ratio
SQUID	superconducting quantum interference device
TMR	tunnel magnetoresistance
TTL	transistor-transistor logic
UXO	unexploded ordnance
VSM	vibrating-sample magnetometer

Symbols

A	m^2	cross-sectional area
B	T	magnetic flux density
B_s	T	saturation flux density
C_p	F	parallel capacitance
C_sc	F	self-capacitance
χ	1	magnetic susceptibility
d	mm	coil diameter
d_c	mm	fluxgate core distance
d_s	mm	fluxgate sensor diameter
d_wd	mm	winding diameter
f	Hz	frequency
f_0	Hz	base frequency
f_exc	Hz	excitation frequency
g	1	gate ratio
H	A/m	magnetic field
H_C	A/m	coercive magnetic field
H_exc	A/m	excitation magnetic field
H_ext	A/m	external magnetic field
H_T	A/m	threshold magnetic field
h	$\mathrm{m}^2\,\mathrm{kg/s}$	Planck's constant($6.63 \times 10^{-34}\,\mathrm{m}^2\,\mathrm{kg/s}$)
k	m/A	k factor ($= \mu_0 m / k_\mathrm{B} T$)
$k_\mathbf{B}$	J/K	Boltzmann's constant ($1.38 \times 10^{-23}\,\mathrm{J/K}$)
$k_\mathbf{L}$	1	Nagaoka's coefficient
L_nsat	H	non-saturated inductance
L_s	H	series inductance
L_sat	H	saturated inductance
l_c	mm	fluxgate core length
l_w	m	wire length
l_wd	m	winding length
M	H	net mutual inductance between M_1 and M_2
M_1	H	primary 1 and secondary mutual inductance
M_2	H	primary 2 and secondary mutual inductance
N	1	coil turn number
N_p	1	primary coil turn number
N_s	1	secondary coil turn number
n	1/m	turns density

Φ	Wb	magnetic flux
R	Ω	resistance
R_p	Ω	parallel resistance
R_ref	Ω	reference resistance
R_s	Ω	serial resistance
S	V/T	sensitivity
S_B	$\mathrm{T}/\sqrt{\mathrm{Hz}}$	magnetic flux density noise
S_f	1	shielding factor
S_sb	V/T	side-band sensitivity
S_v	$\mathrm{V}/\sqrt{\mathrm{Hz}}$	voltage density noise
T_exc	s	excitation current period
T_p	s	excitation current pulse period
θ	$^\circ$	angle
$U_\mathbf{ind}$	V	induced voltage
U_O	V	DC output voltage
u_O	V	output voltage
$\mu_\mathbf{0}$	T m/A	vacuum permeability ($4\pi \times 10^{-7}$ Vs/Am)
$\mu_\mathbf{r}$	T m/A	relative permeability
$\mu_\mathbf{A}$	T m/A	apparent permeability
ω	rad/s	angular frequency ($= 2\pi f$)
ω_0	rad/s	base angular frequency
ω_p	rad/s	angular frequency of excitation signal pulse

Contents

1 Introduction

1.1 Magnetic Sensor Overview

Magnetic sensors are devices, which can detect magnetic field by measuring its absolute value or relative change. Some magnetic sensors have the ability to detect the direction of magnetic field intensity. Based on this ability, magnetic sensor can be divided into two types, that is scalar magnetic sensors, which only measure the absolute value, and vector magnetic sensors, which measure magnetic magnitude and its direction. The proton magnetometer is an example of a scalar magnetic sensor and the fluxgate magnetometer (FGM) is an example of a vector magnetic sensor.

Magnetic sensors have been invented some decades ago [1], but it is still interesting for the researchers to improve the performance to an advanced device. Nowadays magnetic sensor has been used widely in many fields such as medical, geophysics, military, navigation, space research, industry, etc. Magnetic field sensor can even be found almost everywhere in our daily life. For example a magnetic sensor can be found in our PC at hard-disk system, electronic compass in our smart-phones, UXO trackers in battle field, MAD for submarines searching in sea warfare, magnetoencephalography (MEG) for brain signals monitoring, endoscope for interior body organ examining, MFL detector for oil pipelines, magnetometers equipped in Mars explorer, and as magnetometer in mine explorations [2]. The market share of magnetic sensor in the world is rapidly increasing, and will reach USD 2.54 billion in 2022 [3].

There are some main advantages of magnetic sensors in the applications: Firstly the magnetic sensor is a non-contact measurement device, which means the sensor can detect the object without any mechanical contact with it. So this could avoid damage that can be caused by the mechanical contact between object and measurement device. Secondly it's versatile, which can be used for many applications. For example, a magnetic sensor can be used as a sensor for many physical parameters such as displacement, velocity, current density, stress, and vibration using a specific magnetic

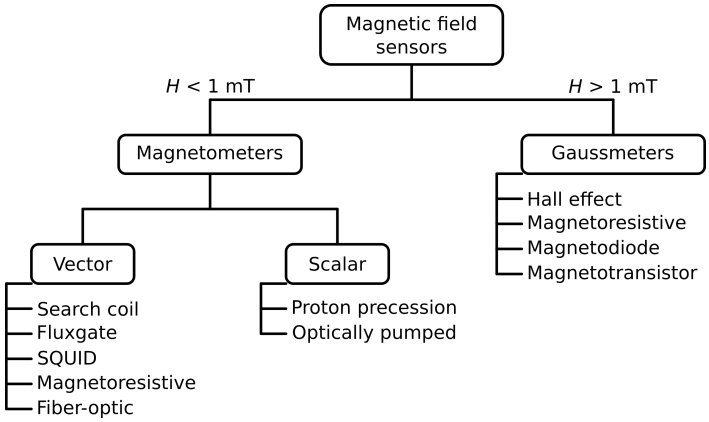

Figure 1.1: Magnetic sensor division based on its measuring ranges [4].

object, which converts these physical measurands to electrical signal. And the last, it is highly reliable and safe, it can be used in harsh environment that contains pollutions, vibrations, and lots of noise.

Magnetic field is measured using many different technologies and methods. Each technology and method has specific advantages and disadvantages, which make it suitable to be used for a particular purpose. The applications of magnetic sensor start from the simple applications such as detecting the presence of magnetic field to the advance applications that need high precision and resolution of a scalar and vector magnetic field [4]. Besides magnetic sensors can be divided into scalar magnitude and vector component types, magnetic sensors can also be divided into sensors that can measure high field and low field. High field is the field that exceeds 1 mT and low field is the field that is below 1 mT. Figure 1.1 shows the types of magnetic sensors based on the measuring range.

The induction coil and fluxgate sensor are the most widely used low-field vector magnetic sensor. They have many advantages such as rugged, reliable, simple in manufacturing process and relatively low-cost compared to other low-field magnetic sensors. The other low-field magnetic sensors such as fiber-optic magnetometer is still in the development in the laboratory to make it more rugged. The SQUID-based magnetometers, as the most sensitive magnetic sensors are more expensive, less rugged and less reliable because they mostly operate in a low temperature and need a special thermal control system.

The proton precession magnetometer is a popular scalar magnetometer. This magnetometer is widely used in the geological exploration and aerial mapping of geomagnetic field. The optically pumped magnetometer is more sensitive than the proton magnetometer, but its disadvantages are more expensive, not rugged and reliable as the proton magnetometer.

Hall effect sensor is the most common magnetic field sensor used in high

Table 1.1: Magnetic sensors characteristics [4–13].

Instrument	Range (mT)	Resolution (nT)	Bandwidth (Hz)
Induction coil	10^{-10} - 10^{6}	Variable	10^{-1} - 10^{6}
Fluxgate	10^{-4} - 0.5	0.1	dc to 10^{4}
SQUID	10^{-9} - 0.1	10^{-4}	dc to 10^{6}
Hall effect	0.1 - 3x10^{4}	100	dc to 10^{8}
Magnetoresistance	10^{-3} - 5	10	dc to 10^{7}
Proton precession	0.01 - 0.1	0.05	dc to 2
Optically pumped	0.01 - 0.1	0.005	dc to 10^{2}

field measurement. Its measurement range is up to 1 T and more. The anisotropic-magnetoresistance (AMR) sensors measure the field in the middle range between high and low-field. The other type of magneto-resistive (MR) sensor is the giant-magnetoresistance (GMR), which is more sensitive than the AMR and potentially replaces the fluxgate sensor in the medium sensitivity application due to its low-cost and easiness in fabrication. The magnetic sensors characteristics are shown in table 1.1.

A lot of literatures on magnetic sensors have been published by many researchers [5, 14–16]. When these publications are compared, it can be concluded that for long time the situation has been very stable and there are four main sensors dominating. They are SQUID sensor used for very small magnetic field, fluxgate (FG) sensor used for small magnetic fields, MR sensor used for medium values and Hall sensors used for high magnetic field. New principles and new sensors (for example GMI sensors, magneto-transistors, magneto-optical sensors, extraordinary magneto-resistance, TMR) are still not competitive to these well established four main principles. Old fluxgate principles are also in progress but it is mainly only on miniaturization or improvement of parameters [17].

At room temperature, fluxgate sensor is very sensitive and has low noise characteristics. Figure 1.2 shows the comparison of room temperature magnetic sensor noise. Fluxgate sensors can measure DC and low-frequency AC magnetic field up to 1 mT with a resolution of 100 pT, the linearity-error less than 10 ppm, and the frequency up to several kilohertz. The working principle of fluxgate sensors is based on modulation of the permeability of a soft magnetic core. This modulation causes changes in the dc flux of a secondary coil wound around the sensor core. The output voltage is obtained from the second or the other even harmonics of the excitation frequency, since the permeability reaches its minimum and maximum values twice for every excitation cycle [18].

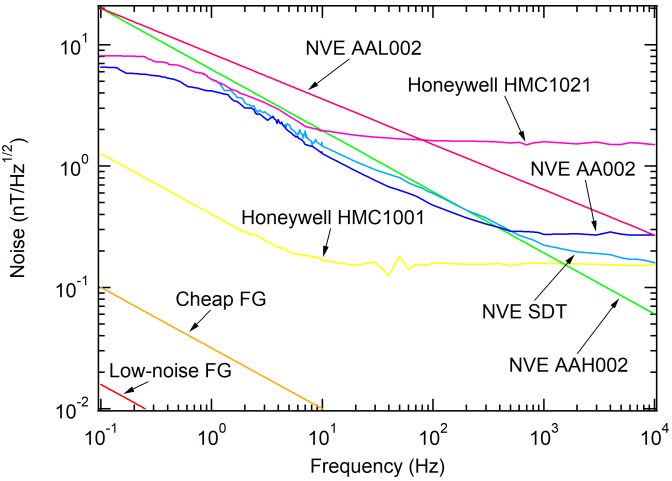

Figure 1.2: Noise spectrum of magneto-resistors and fluxgate sensors [18].

1.2 Motivation for the Fluxgate Sensor Analyzer

Further development of fluxgate magnetic sensors is aimed to build smaller, faster, cheaper, more sensitive, more reliable, and low noise fluxgate sensors, especially for high resolution reading and small noise measurement. Typical very low magnetic field ranging from 10^{-15} to 10^{-10} T currently are often measured by SQUIDs. However, it demands a cryogenic equipment, which restricts its portable and low power applications.

When the required resolution is in the range of 10^{-10} to 10^{-9} T, fluxgate sensors are the best choice because of their advantages in linearity, temperature stability and high sensitivity. The only weakness of the fluxgate sensors is the large size of the sensing element based on bulk ferromagnetic materials, which limits further miniaturization and low power portable applications. The other chance in fluxgate development is to suppress its noise level to the theoretical limit. So then its measuring resolution can be reduced from the current ability, which is about 1 - 10 pT.

Therefore, the main challenge in fluxgate sensor development is how to make its noise lower. To realize this aim, a novel instrument has been built for sensor characterization and FG sensitivity and noise measurement. Some sensors with different physical parameters have been manufactured and then characterized regarding electrical parameters such as the resistance, impedance, and inductance. From these parameters the direct influence on the noise might be analyzed, and as well the geometry influence of a fluxgate sensor to the noise level.

This work describes an instrument that could be used to analyze any fluxgate sensors characteristics of interest. The instrument automatically

runs measuring the characteristic and provides us the data for analysis. A FG analyzer with low output impedance and low excitation current capability is designed for fluxgate sensor characterization to analyze the impedance and symmetry of the geometric configuration. Impedance and geometry configurations are important parameters for examining their influence on fluxgate sensitivity and noise [19]. Impedance, which consists of ohmic resistance, inductance, and capacitance of the fluxgate are measured using the analyzer. Since the effort of future fluxgate sensor development is miniaturization and integration with the electronics [20], it implies the utilization of a small limited winding number of fluxgate sensor coils causing the impedance of the coils to lie in the range between 1 and 100 Ω. The core material of a fluxgate easily saturates even with low current due to its high permeability causing the change of core permeability, which in turn changes the impedance. The change of excitation current could happen because of the increase of coil impedance. In order to provide the same magnetic field, the excitation current must be kept constant. The other properties must also be considered, such as the dependence of permeability on the frequency and bias magnetic field strength [21, 22]. In addition, the influence of frequency sampling and sampled frequency ratio must also be considered.
This idea strongly motivates this work on developing and studying noise properties of fluxgate sensor. With the theory and experiment that were developed, a theory and relationship between sensor characterization and sensitivity and noise level of the sensor could be obtained. It is also expected, a good instrument could be made for sensor characterization.

1.3 Objectives and Significance of the Study

The main objective of this work is to investigate the performance of a racetrack fluxgate sensor in terms of sensitivity and noise properties, focusing on the design and characterization of the electrical parameters i.e. resistance, inductance, and also the geometry of sensor.
The aim of this work is to provide an instrument with special characterization purpose for fluxgate sensors that has special characteristics and can study the influence of this characteristics on fluxgate sensitivity and noise. The designed system is based on an auto-balanced amplifier, which generally offers wide impedance measurement range from millihertz to hundreds of megahertz [23]. The designed auto-balanced circuit is simpler compared to other designs described in [23–25]. It accommodates the impedances measurement with the ability of measuring low impedance with low current. The circuit also implements the identical signal processing stages for voltage and current output for high precision.
In this study, the parameters of self-made fluxgate sensor as the DUT, its equivalent circuit and the calculated impedance values are reported. The system design and characterization sections describe the measurement method, the electronic circuits design especially the auto-balance circuit and its characterization, the use of NI-DAQ PCI-6221 card from National Instrument and also the application of LabVIEW software to measure

and calculate the impedance of DUT. A calibration is performed using fixed resistances and calibrated instruments, then the calibration result is validated. The realized instrument is tested to measure the fluxgate sensor coils impedance. The result of fluxgate characterization is utilized to model the fluxgate impedance and to setup the equation for the fluxgate output voltage calculation.
The detailed objectives of the work are:

- To build an instrument consisting of a fluxgate sensor and FGM characterizer to analyze the fluxgate sensors regarding its electrical parameters, sensitivity and noise.
- To investigate the static and dynamic electrical parameter properties of racetrack fluxgate sensors using the novel FG analyzer and to study the effect of physical parameters, i.e. the number of coil turns and the geometry of sensor.
- To investigate the influence of the electrical parameters of a racetrack fluxgate sensor on the sensitivity and noise using the novel FG analyzer.
- To develop a racetrack fluxgate sensor with high sensitivity and low noise level as well as balanced performance including the size, geometry, and stability.

To obtain the goals, this work incorporates both theoretical and experimental research on the sensitivity and noise properties of fluxgate magnetic sensor. The main problems in the experimental study are the design and development of the instrument for sensor characterization, which is a trade-off between working on non-linear magnetic material core, which does not allow providing large signal and the need of large and clean signal for precision electrical parameter characterization. Besides that, the sensor design i.e. sensor length, diameter, turn number, etc., also determine the electrical parameter of the sensor.
For the theoretical study, analytical models have to be proposed to describe the method of impedance measurement of the fluxgate sensor and to predict the sensitivity and noise of the sensor system. Due to the complication of the problem, other sensor properties, such as temperature stabilities, operation range, linearity, etc., are not in the scope of the study. The results of the present study could provide a new design process for the low field magnetic sensors with improved sensitivity and noise level. The racetrack fluxgate sensors with optimum electrical parameters and geometry are promising for the applications in weak field detection. Also, the static and dynamic characterization of a racetrack fluxgate sensor may foster the understanding of its sensitivity and noise properties.

1.4 Organization of the Thesis

This dissertation is organized as follows. In the next chapter, we review the state-of-the-art of fluxgate magnetic sensors, which introduces their

classification, basic principles and mechanism, and applications. The main focus is on fluxgate magnetic sensor of parallel type with racetrack configuration. The latest research findings on racetrack fluxgate sensors are presented. Furthermore, the physical parameter of the fluxgate sensor and the factors that influence the sensitivity and noise sources, which are the key issues of the main objective are reviewed. Chapter 3 describes the proposed research approach of this work, the characterization tools, and experimental setups used in the study. The main report of this doctoral dissertation starts from Chapter 4, which presents the investigation of the static and dynamic characteristics of the built sensor with the influence of physical and electrical parameters such as number of turns, length, impedance, etc.
The theoretical work is presented in Chapter 4, which describes the noise measurement regarding sensor characteristics and electronics setting. The sensitivity of a racetrack fluxgate sensor is formulated. Comparison between theoretical results and experimental results is presented. This chapter also describes the design and development of a racetrack fluxgate sensor in detail from sensor head to readout circuit, as well as the testing results of sensitivity and noise level. Comparison of the main performance between our prototype and commercial off-the-shelf magnetometers is tabulated. Finally, the conclusions are provided in Chapter 5 summarizing the whole thesis contributions and proposing future work.

2 Literature Review

2.1 Magnetic Field Fundamentals

It is important to understand the basic of magnetic fields in order to know the basic principle used in the magnetic field measurements. The well-known source of magnetic field is a bar magnet, while the other commonly used source is an electromagnet. The magnetic field is a vector quantity, since it has a direction and a magnitude components. The strength of a magnetic field in an object depends on the density of its volume-distributed moments [4], which is known as magnetization M. It is defined as the moment per unit volume

$$\overrightarrow{M} = \frac{\overrightarrow{m}}{V}. \tag{2.1}$$

Magnetization is a material property, which can arise caused by an internal magnetic sources or induced by an external magnetic field. The other magnetic field vector quantity is $\overrightarrow{B}$, this quantity is called magnetic induction or flux density. This is the amount of magnetic flux in an area that is perpendicular to the magnetic field's direction. The relationship between magnetic field $\overrightarrow{H}$ and magnetic induction $\overrightarrow{B}$ is connected by a vacuum permeability constant μ_0 in free space,

$$\overrightarrow{B} = \mu_0 \overrightarrow{H}. \tag{2.2}$$

Magnetic materials can be classified as "Hard" and "Soft" magnetic. The permanent magnetization dominates in hard magnetic material, while the magnetization in soft material is dominated by induction, which follows the equation

$$\overrightarrow{M} = \chi \overrightarrow{H}. \tag{2.3}$$

Equation (2.2) can be modified for soft magnetic material to

$$\overrightarrow{B} = \mu_0(1+\chi)\overrightarrow{H} = \mu_0\mu_r\overrightarrow{H}, \tag{2.4}$$

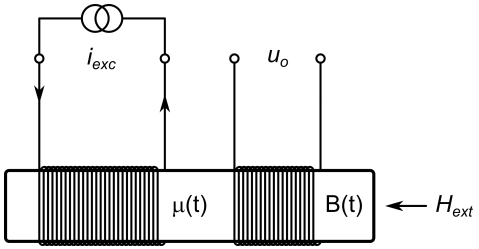

Figure 2.1: Basic fluxgate sensor [26].

where μ_r is the relative permeability and χ is the susceptibility of the material.

2.2 Fluxgate Sensor Introduction

The fluxgate sensor is a type of magnetic field sensor which can measure the magnitude and can detect the direction of magnetic field. It works based on magnetic induction, which utilizes the coils to excite and sense the external magnetic field through a symmetrical nonlinear magnetizing curve [14]. Its measuring range covers several pT to 100 μT with the resolution down to 10 pT [26]. The fluxgate sensor can be operated in DC or low-frequency magnetic field up to several kHz [27]. Depending on the excitation frequency, Tumanski et al. [14] assume that the operating frequency should not be higher than 1/5 of the excitation frequency. The fluxgate is the magnetic sensor that has high superiority performance among other room-temperature magnetic sensors. It relies on its high sensitivity, low noise and excellent accuracy [28]. The better magnetic sensor is only a SQUID magnetometer, which can measure the magnetic field down to several femtotesla and lower, besides, it has lower noise level than the fluxgate [26]. An AMR sensor performance is laying at one level below fluxgate sensors. Its resolution is better than 10 nT, but it is cheaper, smaller, and also has good linearity that is 0.05 % [26]. However, [29] has published a fluxgate sensor operated in high temperature up to 250°C, which confirms the application of fluxgate sensors in high temperature.

The simple configuration of a fluxgate sensor is shown in figure 2.1. It is seen that the basic fluxgate sensor consists of an excitation (primary) and a detection (secondary) coil. The core of a fluxgate sensor is made of soft magnetic material. In the operation, it is periodically brought to saturation in the magnetizing curve by an excitation field through the excitation coil. The core permeability changes due to the excitation field. The DC flux representing the measured DC field B_{ext} is modulated. The "Fluxgate" name is coming from the "gating" process that occurs when the core is in saturation [16].

2.2.1 Applications of Fluxgate Sensor

A fluxgate sensor has been widely used in many applications. The fluxgate sensor is chosen due to its favorable properties and low-cost [30]. With the continuous improvement, the applications of fluxgate sensors become wider. The improvements are including the sensor itself and the supporting devices in the electronic circuit such as amplifier, microcontroller, digitization, etc.

Navigation

The ring fluxgate sensor has been firstly used around 80 years ago [1], it has been initially used as an electronic compass sensor. A compass is an old instrument that uses the magnetic principle in its operation, it has been used by travelers for thousand years and is still being used until the present days for navigation in ships and aeroplane.
As an electronic compass, the fluxgate sensor mostly works on its direction pointing purpose than its magnitude value sensing. The high sensitivity of the fluxgate sensor makes a fluxgate compass becoming the most widely used magnetometer for high accuracy electronic compass [31]. In this application, a two axis fluxgate sensors is needed to detect the angle of the direction. These two sensors are placed on the horizontal plane, together with the known declination value the real direction can be determined [32]. The fluxgate for determining a position and location based on nanoparticle has also been developed by [33].

Geomagnetism

The fluxgate magnetometer is a traditional and the most widely used instrument in geophysical exploration due to its small size, precision, good sensitivity, low noise, and relatively low power consumption [34]. In geophysics application, the fluxgate is operated for susceptometry and magnetic field mapping. It is based on Earth magnetic disturbance in the soil. Each location has a different magnetic susceptibility compared to the surrounding environment. This phenomenon could be used for determining of soil properties in a location or site.
The fluxgate sensor application in geosciences is widespread in several applications for example in magneto-telluric (MT) imaging, which is used as a method to determine the conductivity structure of the Earth's crust and upper mantle. This method applies long-term (low frequency) observations, which enables monitoring the variations of conductivity up to several hundred meters deep below the surface and providing the information about the structure of crust and mantle [35]. The second example is in earthquake studies, the fluxgate sensor is used for collecting some data with long-term magnetic field measurements using MT methods and it helps in order to find faults and determine their geometry. The mapping results will give a description of fault plane, that will usually be more conductive due to the presence of contained fluids and therefore more identifiable [35].

The fluxgate sensor applications in geosciences also include examining the trace of eroded materials by measuring its magnetic susceptibility signature. It helps to determine their origin and the distance they have traveled from their point of origin. The fluxgate sensor can be used for this purpose, it can quickly supply the information about the type of rock from which sediments are derived and helping in the understanding of erosion processes [35].
The climatic conditions (temperature, rain, wind, etc.) and environment in nature will influence how some sediments are created and react. For example, in a dry and cold environment, sediments will be created without chemical process. If the same sediments are created in a warmer and wetter environment, it will be followed by chemical or biological processes that affect the nature of the minerals, causing a process of magnetic enhancement. Thus, magnetic susceptibility measurements using fluxgate systems help studying wind-blown dusts, which support in understanding climate change [35].
In archaeology, the fluxgate sensor is used to assess deep and shallow objects for a large-scale archaeological investigations. This is done by utilizing the combined potential field transformations on the signal [36].

Medical

In medical applications, the fluxgate is used as magnetic field detection located near an MRI instrument. Besides that, the fluxgate sensor is also used in magnetic nanoparticle detection in cancer research. An other medical application is in preventing potentially fatal accidents in MRI machine caused by an object inside the bore [37].
The other application of fluxgate sensors in medical is for detecting dust in the lungs from metal workers and miners as described in [38, 39]. Magnetic dust is not only detected in the lungs of metal workers, but also in general public space. Other possible medical applications are the tracking devices and systems in the human body. A magnetic material is used as an object detected in the body. This method can be used in the digestion system for digestive track [38]. The fluxgate usage as an heart's magnetic detector has been proposed by [40]. They replace the SQUIDs with the fluxgate sensor to measure the heart's magnetic field.

Space missions

The fluxgate sensors was first used in space research in the 1940s, and since that, space vehicles and satellites use fluxgates sensor to perform the research [41]. In space mission, a magnetic sensor mostly a fluxgate sensor is used to measure the orbit magnetic field due to its high sensitivity and low noise. Earth's magnetic field measurements in space-based are essential and needed to study the plasma processes around the Earth, which describe the solar and Earth connection. This incorporates the phenomenon in the nature of current systems and plasma waves during storms and sub-storms, which are thought to cause the acceleration and

loss of energetic particles in the Van Allen radiation belts, and determine the space weather [42].

Exploration

In exploring applications such as oil exploration, fluxgate sensors are sometimes used on the drilling system, which together with declinometer/inclinometer can be the guider of drilling system. The application of high temperature fluxgate sensor for drilling system was studied by [29]. Besides that, a fluxgate sensor is also used in the mapping of mineral core. Fluxgate sensor is used to detect the magnetic field beneath the Earth's surface by sensing physical properties of rocks (magnetization). This detecting process can help to find and locate minerals [43].

Industry

In industry fluxgate sensor can be used as proximity switch, displacement, position sensor, non-contact tachometers, for current measurement, etc. [44]. Magnetic methods of nondestructive evaluation can be used either to monitor material state and properties (such as residual stresses) or to find defects.

2.2.2 Existing Fluxgate Technologies

Traditional Fluxgate Sensor

The traditional fluxgate sensor is the original technology of the fluxgate sensor. This technology has been invented quite long time ago and still is the most studied until present days [45]. This kind of fluxgate sensor use enameled wire for the coil and wound on a core material. Many versions have been developed such as single rod, förster, vacquier, ring core, and racetrack [19, 46–49]. None of these kinds has absolute superiority over the others. Each type of sensors has its advantages and disadvantages.

Micro-fluxgate

The micro-fluxgate sensor is a fluxgate sensor based on MEMS technologies, usually integrated with the read-out circuit [50]. The micro sensor is made by semiconductor technology and realized in a small space. The process commonly used is the CMOS process. The micro-fluxgate sensors have small size, light weight, are integrated, and show lower sensitivity compared to conventional fluxgate sensors. But the power consumption is still high at several dozen of mW makes the micro-fluxgate uncompetitive compared to others [51]. Moreover, the complexity of micro-fluxgate fabrication is high and the performance degrades with the smaller size of the core [52].
It is described in [53] that the MEMS technology brings advantages as follows: small size, light weight, high sensitivity, and integration of signal processing circuits. It can be used in applications of bio-nanoparticle

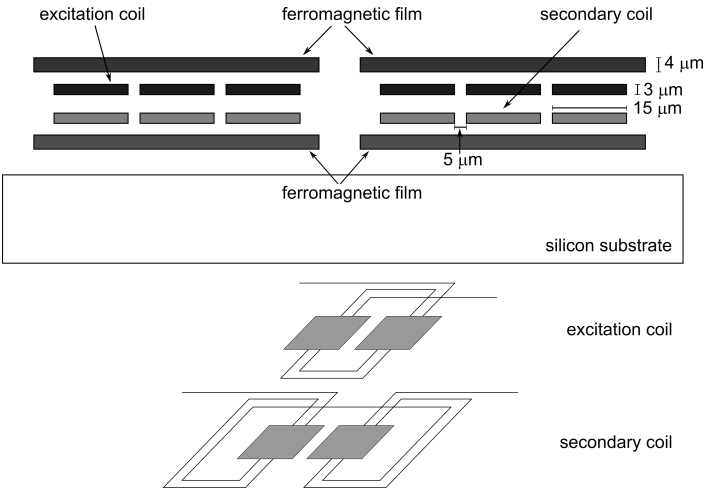

Figure 2.2: Micro-fluxgate sensor [52].

detection, GPS positioning, nano/pico-satellite attitude control and for game control equipment, etc. But on the other hand the MEMS technology also provides some disadvantages due to the limitation of the size and saturation magnetizing principle of the operation, especially in signal-to-noise ratio and power. The small size of micro-fluxgate causes low sensitivity due to its small winding number and cross-sectional area.

PCB Technology

PCB fluxgate offers simplicity in sensor manufacturing. It reduces the complexity in traditional fluxgate sensor manufacturing process [54]. In PCB fluxgate, the coil wire is replaced by PCB track, which is printed on the PCB. The PCB fluxgate sensor usually consists of several layers to create turns by combining those layers. Some of the PCB benefits are stability of the sensor's parameters (as there are no wound or moving parts), low dimensional demands, and ease of mass-production [55]. But the PCB fluxgate sensors also have some disadvantages for example the limitation in their parameters like the low number of turns of the coils created by PCB technology [55].
The result of a PCB fluxgate sensor is described in [56]. From this paper the sensitivity of the sensor is 1800 and 13100 V/T for un-tuned and tuned pick-up coil, respectively. The noise density from the sensor built here is about 0.2 $nT/\sqrt{Hz}$ @ 1Hz. This sensor is built without feedback, so the linearity is still poor and has a small measurement range. It is also described in [55] that they built a PCB fluxgate sensor with the sensitivity reached up to 120.000 V/T and the noise of 20 $pT/\sqrt{Hz}$ @ 1 Hz.

Planar Fluxgate

The planar fluxgate sensors come as a solution in reducing the size and weight of fluxgate magnetic sensors. These needs are very important in military and aerospace technologies as well as in microelectronics industry [20]. Therefore, the trends of future development of fluxgate is emphasized on this miniaturization and allow them to be used in the microelectronics technology. The study for small and reliable fluxgates started in the mid 90's with the report by Vincueria et al., of a fluxgate sensor based on planar technology [57].
The development of planar fluxgate is intended to be used in many applications such as industrial, automotive, military, household instruments, etc., in where the sensitivity and the noise are not so important compared to the cost and the simplicity in manufacturing [57].
Some problems should be solved to actualize the miniaturization of fluxgate sensor, generally there are two main problems, they are the miniaturization of coils and the placement of ferromagnetic core in the sensor. The efforts of the miniaturization of coils consist of utilizing planar coils in several layers with the deposited magnetic core and the use of many fabrication processes to make coils enclosing a ferromagnetic thin film core [20].

2.2.3 Performance Comparison

Until now the performance of fluxgate sensors is still lead by the standard traditional technology, which its resolution down to the order of 1 nT and the noise of about 10 pT/$\sqrt{Hz}$ @ 1 Hz. It could not be competed by the other technologies, where micro-fluxgate sensor has larger noise due to the small size [26] and the PCB technology has low sensitivity due to limitation on the coil winding number.
Micro-fluxgate sensors bring a new development in fluxgate sensor, which in standard traditional sensor is not fix and difficult to be manufactured. Micro-fluxgate minimizes the size of sensor and standardizes the manufacturing process. The researchers have succeeded reducing the size of the fluxgate sensor and it works well, but the performance of the sensor is not as good as that of standard fluxgate sensor. The micro-fluxgate sensor still has inferiority if compared to standard fluxgate sensor especially in sensitivity and noise performance.

2.3 Fluxgate Sensor Basics

2.3.1 Fluxgate Principle

The basic configuration of a fluxgate sensor consists of two coils of which the first coil acts as an excitation or primary coil and the second acts as a pick-up or secondary coil as shown in figure 2.1. Both coils are wound on a high permeability core material, which has the symmetrical nonlinear magnetizing curve [18, 30]. The excitation coil generates excitation field

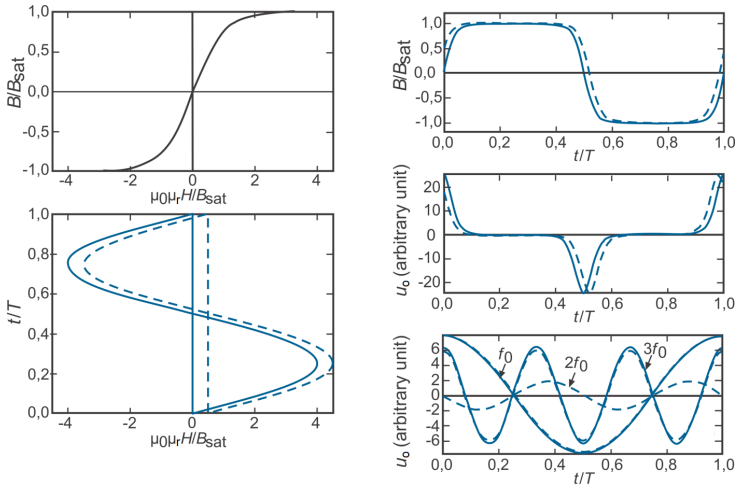

Figure 2.3: Principle of FG sensor [59].

as a reference signal, the pick-up coil senses the modulated external field and converts it to an electrical signal. The general equation for induction sensors is

$$u_{ind} = N_s A \mu_0 \mu_r \frac{dH(t)}{dt} + N_s H \mu_0 \mu_r \frac{dA(t)}{dt} + N_s A H \mu_0 \frac{d\mu_r(t)}{dt}. \quad (2.5)$$

The first term is the equation for search coil, the second one is for rotating coil sensor where $A(t)$ is the effective area that is perpendicular to the magnetic field, and the last term is the basic fluxgate equation [58]. The basic principle of fluxgate sensor is shown in figure 2.3. The presence of an external magnetic field introduces the second harmonic (and other even harmonics) signal that arises at the secondary output signal. While when there is no external magnetic field the even harmonics vanish, only odd harmonics remain.

2.3.2 Modeling of Magnetization Curve

Some simulations are needed to analyze, design and optimize a fluxgate sensor. In order to simulate the fluxgate sensor a mathematical model and calculation accuracy for magnetic core is very important. There are a lot of approaches to model the magnetic hysteresis loop, which can be generally divided into three groups [60]: (1) Macroscopic magnetization. This approach ignores the underlying physics of the material behavior, such as tri-linear model, tangent function model, arctangent function model [61], and Preisach model [62] et al.; (2) Micro-magnetic theory. This approach is originated from complex hysteresis theory, however it is difficult to apply

in real engineering materials; (3) Semi-macroscopic magnetization. This approach combines the microstructural parameters with the macroscopic magnetization curves, this is adopted by Globus model [63] and Jiles-Atherton model [64]. The Jiles-Atherton model is originated from the physical process of magnetic hysteresis and described by a first-order differential equation. Its simplicity in mathematical expressions and more accuracy make it widely used in hysteresis model in applications [65].
Up to present time, fluxgate sensor sensitivity analysis has been studied intensely, but a simple analytical equation was not yet available [66–71]. A simplified and linearized hysteresis model has been presented by Gordon et al. in [66]. A nonlinear polynomial hysteresis model is presented by Marshall in [67]. Primdahl utilized an actual hysteresis curve of a material reproduced by the means of a coordinate measuring table for a theoretical analysis of the fluxgate output [68]. Burger divided the hysteresis loop of the core into relatively small linear segments in which the slope is assumed to remain constant [69]. In 2000, Deak et al. employed the Landau-Lifshitz-Gilbert equation for a single-crystal fluxgate core for a dynamic response model proposal [70]. In 1970, Primdahl presented a comprehensive analysis of the fluxgate mechanism [68]. The output signal of the fluxgate magnetometer is given by [72]

$$U = -2N_s A H_{ext} \frac{d\mu_a}{dH} \frac{dH}{dt} = -2N_s A H_{ext} \frac{1}{(1 + D\mu)^2} \frac{d\mu}{dH} \frac{dH}{dt}, \tag{2.6}$$

where μ_a is the apparent permeability and D is the demagnetizing factor that involving the internal field of the magnetic core. The function of $H(\mu = dB/dH)$ is rather nonlinear, even more near the saturation fields. As the consequence, according to equation (2.6), the response function must also be nonlinear [66]. A. L. Geiler et al. [72] has studied a model for magnetic core. As shown in equation (2.6), the nonlinearity in the fluxgate response via a functional dependence of μ on H near saturation should be incorporated. Therefore, a model of the magnetization curve near saturation is needed and then continued using equation (2.6) to get the response of the sensor.

3rd Order Polynomial

One of the models used for the magnetization curve is 3$^{\text{rd}}$ order polynomial [73]. This polynomial is implemented to approximate the magnetic induction from the magnetization curve as shown in equation (2.7):

$$B = a \cdot h - b \cdot H^3. \tag{2.7}$$

For a double core fluxgate, the measured field H_{ext} and the excitation field H_{exc} is summed between core 1 and 2 as

$$H_{1,2} = H_{ext} \pm H_{exc} = H_{ext} + A \sin(\omega t) \tag{2.8}$$

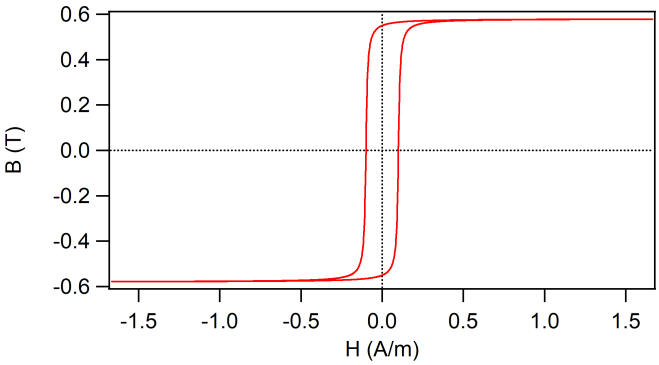

Figure 2.4: Magnetization curve of fluxgate sensor core [59].

then substitute to the equation (2.7);

$$B_{1,2} = a \cdot (H_{ext} \pm A\sin(\omega t)) - b \cdot (H_{ext} \pm A\sin(\omega t)^3) \tag{2.9}$$

$$\begin{aligned} B_{1,2} = {} & a \cdot H_{ext} - b \cdot H_{ext}^3 - \frac{3}{2} b \cdot A^2 H_{ext} \\ & \pm (a \cdot A - 3b \cdot A \cdot H_{ext}^2 - \frac{3}{4} b \cdot A^3)\sin(\omega t) \\ & + \frac{3}{2} b \cdot A^2 \cdot H_{ext}\cos(2\omega t) \pm \frac{1}{4} b \cdot A^3 \sin(3\omega t) \end{aligned} \tag{2.10}$$

the core should have equal cross-section S, then the flux is summed between core 1 and 2 we get

$$\Phi = S \cdot (B_1 + B_2) \tag{2.11}$$

$$\begin{aligned} \Phi = {} & 2S \cdot (a \cdot H_{ext} - b \cdot H_{ext}^3 - \frac{3}{2} b \cdot A^3 \cdot H_{ext} \\ & + \frac{3}{2} b \cdot A^2 H_{ext}\cos(2\omega t)) \end{aligned} \tag{2.12}$$

and the second harmonic of excitation frequency term is only at

$$\Phi(t) = 3S \cdot b \cdot A^2 \cdot H_{ext}\cos(2\omega t) \tag{2.13}$$

Arc Tangent

Another model used to approximate the magnetization curve is an arc tangent function. It is based on the "S" shape of this function, which is similar to the magnetization curve shape. Inspired by that similarity, Wang et al. [74] and A. L. Geiler et al. [72] propose this function to

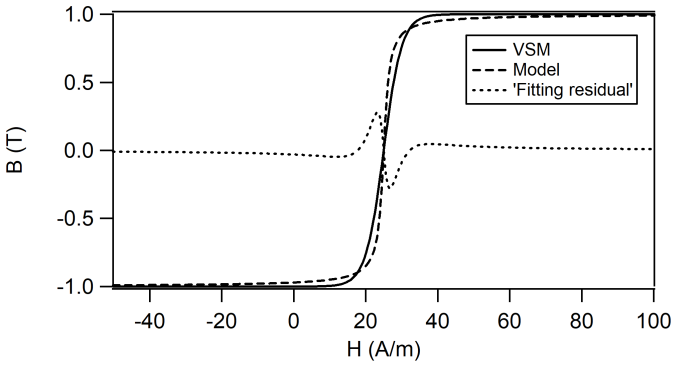

Figure 2.5: Permalloy magnetization curve fitting, showing large fitting errors near saturation [72].

describe the magnetization curve of magnetic materials using equation 2.14:

$$B(H_{ext}) = \frac{2B_s}{\pi} \tan^{-1}\left(\frac{H_{ext} \pm H_C}{H_T}\right) \tag{2.14}$$

As a threshold field (H_T), it has to be overcome in order to saturate the sample magnetically. Its presence is analogous to an internal local uniaxial anisotropy field and its magnitude is constant and uniform throughout the sample. Figure 2.5 is an example of B as a function of H for a permalloy film where $B_S = 1$ T, $H_T = 4.7$ A/m, and $H_C = 28$ A/m from [72]. A DC hysteresis loop using this approximation is performed for an illustration. It could be different if an AC hysteresis loop is applied. A. L. Geiler et al. [72] has made some calculations and measurements for the hysteresis loop. The calculated curve from the model is compared with the actual hysteresis curve of the sample measured by VSM. There is a difference between the calculated and measured curves about 15% near the saturation.
Since equation (2.14) uses a simple analytical equation to model hysteresis loops with only one fitting parameter, it makes some failures in fitting near the saturation. To correct the fitting, the non-uniform distribution of the following form is applied

$$H_T = a + b\left(\frac{\Gamma/2}{(\Gamma/2)^2 + (H - H_0)^2}\right) \tag{2.15}$$

where a, b, Γ, and H_0 are some fitting parameters for a scaled Lorentzian function and resulting the fitting curve as shown in figure 2.6. By modifying the hysteresis models with both equation (2.14) and (2.15), the permalloy hysteresis is obtained as shown in figure 2.6. In this case, the maximum error obtained near the saturation is 5% [72].

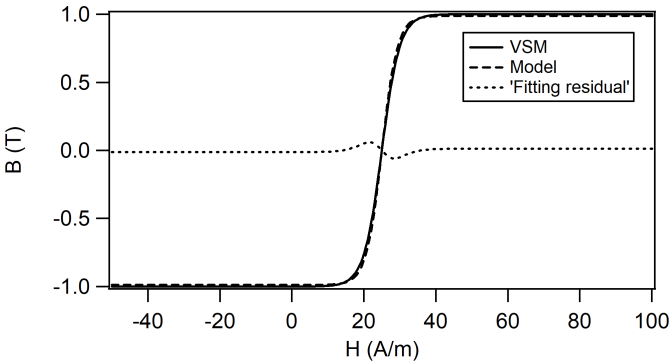

Figure 2.6: Improved Permalloy magnetization curve fitting with the modified hysteresis model that incorporates both equation (2.14) and (2.15) [72].

Types of Fluxgate Sensor

Fluxgate sensors can be classified in two types: parallel and orthogonal fluxgate sensors. The rod, ring, and racetrack fluxgate sensor are the types of parallel fluxgate, while the wire-core and cylindrical core are the types of orthogonal fluxgate. The rod is an open-loop magnetic path fluxgate, while the ring and racetrack are closed-loop magnetic path fluxgates. The rod fluxgate sensors are shown in figure 2.7. The rod fluxgate can be divided into several subtypes regarding the coil winding. There are single rod (figure 2.7a), double rod with common secondary coil (Vacquier) (figure 2.7b), and double rod with separated secondary coils (Förster) (figure 2.7c). The orthogonal fluxgate sensors consist of wire-core (figure 2.7d) and cylindrical core (figure 2.7e). The advantage of a rod fluxgate is a low demagnetization factor due to the small ratio of cross-section and length, which is in the direction of measured field. The disadvantage of the rod fluxgate is that concerning the open magnetic path in the core, this makes the level of saturation varies along the core, raising problems with sensor offset. To deal with this, the secondary coil is placed not to enclose the noisy and unsaturated core ends [73].

The ring core fluxgate is a closed-loop core sensor. Its excitation coil is directly wound on the core, while the secondary coil is usually wound to enclose the ring core and excitation coil. The ring core fluxgate sensor is depicted in figure 2.8 The ring core fluxgate core has a high demagnetization factor. Its demagnetization is higher than the demagnetization of rod-sensor. The main advantage of ring core sensor is on the low power consumption needed to magnetize the core to saturation due to the closed-loop magnetic path [14]. This sensor also exhibit lower noise due to its symmetrical geometry [75, 76]. The other closed-loop path sensor is the racetrack fluxgate sensor, which is a compromise of low demagnetization

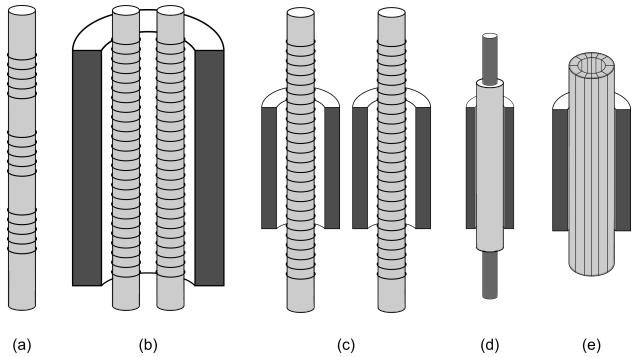

Figure 2.7: Fluxgate sensors with open-cores [14]: parallel fluxgate sensor; single-core (a), Vacquier (b), and Förster (c), and orthogonal fluxgate sensor; wire-core (d) and cylindrical core (e).

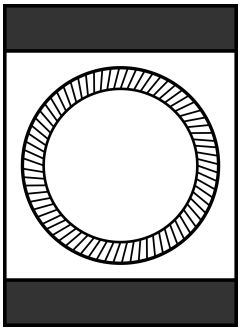

Figure 2.8: Ring core fluxgate sensor [14].

in rod core and low power and noise in ring core sensor. As the combination of rod and ring core sensor, the racetrack sensor has more advantages compared to the other sensors. It has high sensitivity, low noise, and is not influenced by perpendicular fields. The racetrack sensor is shown in figure 2.9.

2.3.3 Modeling of Racetrack Fluxgate

The type of fluxgate sensor that is used in this work is the racetrack fluxgate, which is actually a Vacquier type fluxgate with a closed-path magnetic core. The closed-path magnetic core is intended to suppress the unwanted excitation signal and also to reduce the noise due to strong excitation signal. One of the closed-path magnetic core examples is a ring-shape core. The ring-shape core has a rotational symmetry, so the

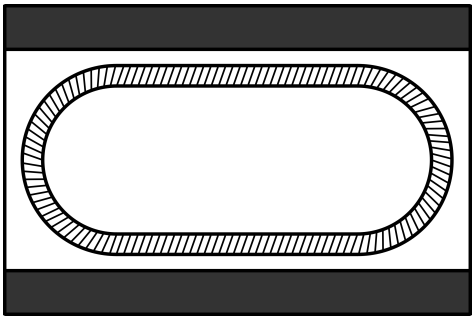

Figure 2.9: Racetrack fluxgate configuration [14].

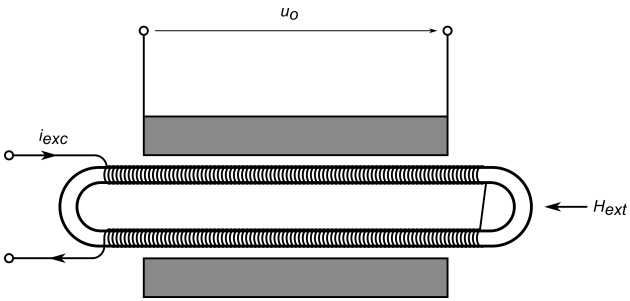

Figure 2.10: Racetrack fluxgate sensor [26].

pick-up coil can be rotated freely to get the best sensitivity and suppress the unwanted excitation signal [73]. However, it has the disadvantage of relatively high demagnetization reducing its sensitivity when compared to rod fluxgate sensor. Because of that, to reduce the demagnetization factor of the closed-path core, it is designed as a racetrack shape core of the fluxgate sensor.
The sensitivity of the racetrack sensor is higher than the ring core fluxgate and less sensitive to perpendicular fields, due to the lower demagnetization factor (figure 2.10). The racetrack, on the other side, still has the advantages of the closed-type sensors; low-noise as low as 6 pT/$\sqrt{Hz}$ at 1 Hz was reported for sensor having 65 mm long racetrack amorphous core [48].

2.3.4 Demagnetization

The demagnetization factor is an important parameter for fluxgate sensors and has been studied for fluxgate sensors characterization in many publications. Demagnetization itself is occurred due to the internal field oriented against the external field. Thus, when a ferromagnetic material

is placed in a homogeneous magnetic field H_{ext}, the magnetic field in the ferromagnetic material H_F is smaller than the external field H_{ext} [49]. Estimating the average demagnetization factor of a particular sensor core and detection coil is not simple. Some researches have studied and published the theory and experimental results in support of the demagnetization factor. The results indicate that the long rod sensor is superior compared to more compact sensors like ring core. Despite of this, it is reported that the ring core sensor has better performance than the other sensors in term of signal-to-noise ratio [75, 77].
The magnetic field in the ferromagnetic object can be written as

$$H_F = H_{ext} - DM_F \tag{2.16}$$

where D is a demagnetization factor (ranging between 0 and 1), and $M_F = \chi H_F$ is the magnetization. Then equation (2.16) becomes

$$H_F = \frac{H_{ext}}{1 + D\chi} = \frac{H_{ext}}{1 + D(\mu - 1)} \tag{2.17}$$

The demagnetizing field is homogeneous only in the case of ellipsoidal objects. Then, the demagnetization is independent of the permeability and only depends on the object geometry. The demagnetization factor is the most important property for a fluxgate sensor designer in determining the direction of the sensor sensitivity axis [49].

2.3.5 Apparent Permeability

Because of zero demagnetization factor for a very long rod core, the magnetic field H_F in such a core is equal to the longitudinal external magnetic field H_{ext}. The output voltage of a fluxgate sensor with a cross-sectional area A for this core follows equation (2.18).

$$U_o = N\mu_0 H_F A \frac{d\mu_r(t)}{dt} \tag{2.18}$$

If the shape of the core is different from the long rod core, the demagnetization factor has to be considered. The demagnetization occurred in the core causes the change on the permeability. The change tends to decrease the permeability. This is then called the apparent permeability. So that, the apparent permeability is strongly related with the demagnetization factor of the core. The demagnetization factor modifies the permeability to be the apparent permeability as shown in [49, 76, 78]

$$\mu_A = \frac{\mu_r}{1 + D(\mu_r - 1)}. \tag{2.19}$$

This will change the equation of the sensor output. Substituting and differentiating this permeability into the output voltage yield a new equation of output voltage

$$U_o = -N\mu_0 H_{ext} A \frac{1 - D}{[1 + D(\mu_r(t) - 1)]^2} \frac{d\mu_r(t)}{dt}. \tag{2.20}$$

From the equation above, it can be seen that the demagnetization factor affects the sensitivity of the sensor output. If the demagnetization is zero then the output will be maximum and if the magnetization factor is 1 then the output will be zero. Thus, the demagnetization factor also plays an important role in the noise performance of the fluxgate sensor, since the noise performance is correlated with the fluxgate output voltage and sensitivity.

2.4 Fluxgate Excitation

The excitation circuit type used in this study is the series resonance circuit, which is driven by a voltage source. The other type is the parallel resonance excitation driven by a current source. These circuits are shown in figure 2.11. The current peak from the series resonance is independent

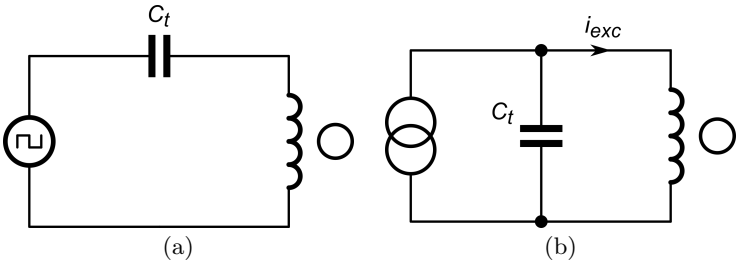

Figure 2.11: Fluxgate excitation circuits: (a) Series resonance and (b) parallel resonance [79].

of the voltage source waveform and the current excitation can be excited with a low voltage source [79]. The fluxgate excitation circuit generally consists of a tuning capacitor (C_t) and the fluxgate excitation coil itself. The circuit schematic of excitation is shown in figure 2.12. The impedance of the fluxgate primary coil is

$$Z_s = R_s + j\omega L_s. \tag{2.21}$$

where R_s is the series resistance of the coil and L_s is the series inductance of the coil. Here, the capacitance of the coil is ignored, since the effect of the capacitance is very small at the excitation frequency used.
The implementation of the tuning capacitor connected in series with the primary coil is aimed to provide a high excitation current to the fluxgate. Then the impedance of the resonance circuit can be written as [80]

$$Z_r = \frac{1}{j\omega C_t} + Z_s = \frac{1 + j\omega R_s C_t + (j\omega)^2 L_s C_t}{j\omega C_t}, \tag{2.22}$$

or

$$Z_r = \frac{(s - s_1)(s - s_2)}{j\omega C_t}. \tag{2.23}$$

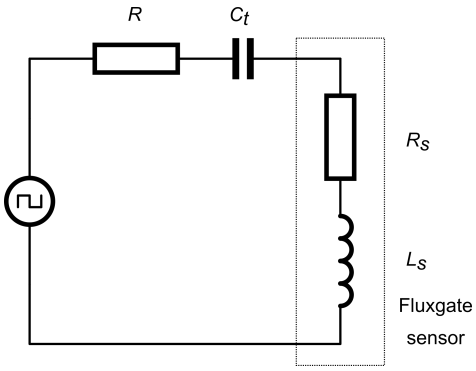

Figure 2.12: Excitation circuit of fluxgate sensor [80].

where

$$s_1 = \frac{-R_s}{2L_s} + \sqrt{\frac{R_s^2}{4L_s^2} - \frac{1}{L_s C_t}}, \tag{2.24}$$

and

$$s_2 = \frac{-R_s}{2L_s} - \sqrt{\frac{R_s^2}{4L_s^2} - \frac{1}{L_s C_t}}. \tag{2.25}$$

From the numerator of (2.22), the damping factor ξ is written as

$$\xi = \frac{R_s}{2}\sqrt{\frac{C_t}{L_s}}. \tag{2.26}$$

The damping factor ξ in equation (2.26) should be smaller than unity in order to maximize the peak current in the excitation coil at the saturation condition. Therefore, from (2.26) we can write

$$\xi = \frac{R_s}{2}\sqrt{\frac{C_t}{L_{sat}}} < 1, \tag{2.27}$$

then

$$C_t < \frac{4L_{sat}}{R_s^2}, \tag{2.28}$$

where L_{sat} is the series inductance at the saturation condition. From equation (2.28) it is seen that the inductance of the fluxgate coil should be characterized to get proper current peak value and to obtain better sensitivity of fluxgate sensor. The inductance measurements in [80], as shown in figure 2.13 have been conducted to determine the proper resonance circuit of the excitation by determining the tuning capacitance C_t.

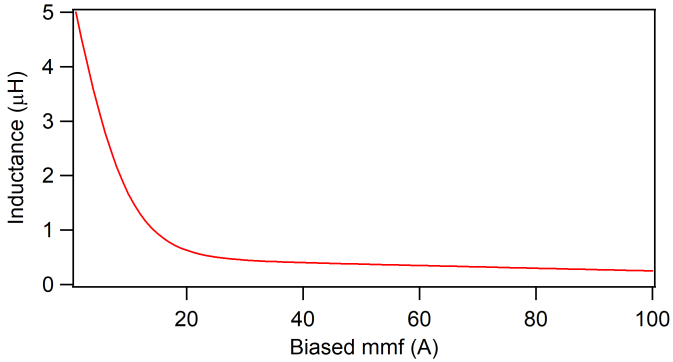

Figure 2.13: Measurement of inductance with biased dc voltage, modified from [80].

2.5 Fluxgate Sensitivity and Stability

The sensitivity of fluxgate sensor is measured in open loop condition. This condition eliminates the sensitivity influenced by the electronics and purely from the sensor as its property [19]. The sensitivity of fluxgate sensor is derived by [19] as

$$S \approx 4N_s A f \mu_{eff} \tag{2.29}$$

where N_s is the secondary coil turn number, A is the secondary coil cross-section area, and μ_{eff} is the effective relative permeability. The sensitivity of a fluxgate sensor is influenced by many factors. Some considerations to increase the sensitivity, as explained in [5, 81], are:

- the ratio of the resistance and inductance should be kept small.
- the drive frequency should be as high as possible limited by the properties of the core, by the maximum excitation field and response time of the ferromagnetic material.
- a large number of secondary coil N_s is preferred. The high number of N_s leads to higher L which leads to higher sensitivity with the adjustable C, but higher N_s also leads to higher R and stray capacitance, which caused the effects of harmfulness to sensitivity, stability, and sensor size, especially at high frequency.
- the duty cycle of the excitation should be chosen carefully. The trade-off of sensitivity and the power consumption should be considered.
- the gate ratio g is a critical factor in the fluxgate sensitivity. It is defined as the ratio of the original inductance L_{nsat} to the saturated inductance L_{sat}. The gate ratio depends on the effective

differential permeability and on the sensor geometry. The gate ratio is also influenced by the demagnetization factor, the geometry and construction of the core and sensor winding.

- the shape of the hysteresis curve also influences the fluxgate sensitivity. The magnetic field and magnetic induction (B-H) curve should be in square for maximum sensitivity, because this produces the highest induced electromotive force (emf) for a given value of the magnetic field. For minimum power consumption, the core material should have low coercivity and saturation values.

The fluxgate sensor stability is influenced by the critical resistances of fluxgate coils. This critical resistances are studied by [82] and the equation is obtained to determine this resistance as shown in

$$R_c \geq \frac{L_{sat}}{T_{exc}} \sqrt{g} \frac{3\sqrt{g}+1}{\sqrt{g}+3} \ln g \tag{2.30}$$

with

$$g = \frac{L_{nsat}}{L_{sat}} \tag{2.31}$$

If the resistance is smaller than this critical resistance, the fluxgate will be unstable. The tuned output fluxgate is often applied to get higher sensitivity of fluxgate sensor, which has been studied by [83].

2.6 Fluxgate Sensor Noise

2.6.1 Thermal Noise

Thermal noise is the noise that exists in every electronic devices. It is the basic form of noise, which has white spectrum coming from the effect of thermal, so that it is also called white noise. It is sometimes also known as Johnson noise, which is a natural consistency of fluctuation-dissipation theorem [84]. Thermal noise is generated by the motion of free electrons in a lossy element due to the dissipation produced caused by an external thermal sources. It can be generated in a resistance due to temperature even when the resistance is not connected in a electronic circuit. The noise power of the thermal noise is constant within the bandwidth that usable in the electronic circuits. The maximum noise power of a thermal noise source is given by

$$P_n = k_B T \Delta f, \tag{2.32}$$

where P_n is the maximum noise power, T is the absolute temperature, and Δf is the bandwidth.
An example of thermal noise is the noise in an electrical resistor with resistance R, it can be described in voltage fluctuations. With the voltage

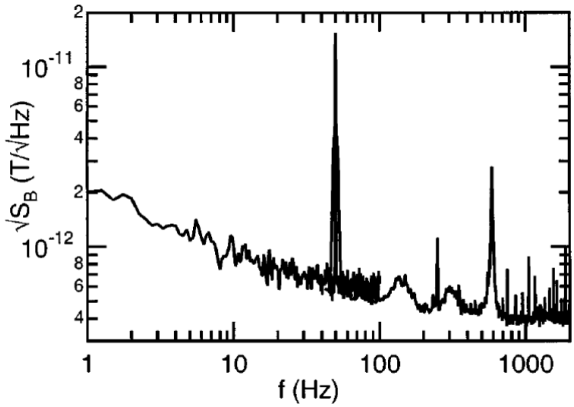

Figure 2.14: Noise spectrum of racetrack fluxgates [19].

V across the resistor, the power dissipated in the resistor is determined by

$$P = V^2/R. \tag{2.33}$$

The voltage fluctuations of noise is random and unpredictable, so that the noise voltage is given in the rms value, that is

$$V_n = \sqrt{4kTR\Delta f}, \tag{2.34}$$

resulting the noise spectral power $S_v(f) = 4kTR$. At room temperature, a 10 kΩ resistor operating in a 1 MHz bandwidth yields a thermal fluctuation of about $S_v^{1/2} = 12.9nV/\sqrt{Hz}$, and a noise voltage over the bandwidth V_n of 12.9 μV [84].
It is predicted in [85] that the theoretical limit of fluxgate sensor white noise with the size of 2×10^8 m^3 is 100 $fT/\sqrt{Hz}$. The white noise varies with the lossy susceptibility of the core and inversely with the volume [85]. Colmar Hinnrichs et al. [19] have shown that the white noise level of different fluxgate sensors depends on its geometry. It is concluded that the length and the width of fluxgate sensors affect the demagnetizing field and determine their sensitivity. It is also concluded that the main source of white noise level is the current fluctuations in the core material. By optimizing the operation of their best sensor, they achieve a low white noise of about $\sqrt{S_B}$(1 kHz) = 390 fT/$\sqrt{Hz}$ and $\sqrt{S_B}$(1 Hz) = 2 pT/$\sqrt{Hz}$. This result is lower than commercially available fluxgate sensors. The noise spectrum is shown in figure 2.14. This achievement shows the potential of this type of fluxgate sensor to be used in low noise and low frequency measurement. The scaling of the geometry in small dimensions for the same demagnetization factors should be implemented to maintain

this low noise level for smaller sensors, despite the fact that the noise is usually increasing with the reduced sensor size. The lower noise is required in biomagnetic application. Therefore, a further improvement is needed to achieve the noise below 100 fT/$\sqrt{Hz}$, where the signal-to-noise ratio is sufficient to detect a smaller magnetic field from human heart [19].

2.6.2 Flicker Noise

Flicker noise normally occurs in electronic devices as a result of many sources like impurities in a conductive channel, generation and recombination noise in a transistor due to base current, and imperfect contact between two materials. It is always related and generated in the presence of a direct current. This noise is a low frequency noise because it increases at low frequency and its power spectral density is proportional to the square of flicker noise current and inversely proportional to the frequency. Therefore, flicker noise is sometimes called as *1/f noise*. It is also called *pink noise*, this name comes from the optical analog of pink light, which its power density increases at the lower frequency [2, 86].
It has been shown by [87] that the low frequency noise of the fluxgate sensor is not caused by the signal conditioning and feedback loop electronics, nor by excess noise in the excitation current. They predict that the main source of the noise is generated within the sensor core. A model has been given to distinct the behavior of 1/f and white noise. The equation for the flicker noise of an orthogonal fluxgate has been proposed as given by [87]

$$S_B^{1/2} = k_{1/f} \cdot \frac{MLE(I_{ac}, I_{dc}) + S_{v_w}^{1/2}}{S(I_{ac}, I_{dc})} \cdot \alpha_N^{-1} \tag{2.35}$$

where $S(I_{ac}, I_{dc})$ is the open loop sensitivity for I_{ac} and I_{dc} bias, *MLE(I_{ac}, I_{dc})* is the energy dissipated in the minor loop, $S_{v_w}^{1/2}$ is the white noise, α_N is the coefficient of the noise reduction obtained using N wires referred to single wire sensor ($\alpha_N \cong 1$ for $N_w = 1$), and $k_{1/f}$ is a generic constant [87].

2.6.3 Barkhausen Noise

In a hysteresis loop of a ferromagnetic material, the magnetization curve has the random discontinuous increments while magnetizing the material with a varying external magnetic field. It is occurred due to an effect of magnetic domain walls movements in the material with structural disorder and impurities [88, 89]. This phenomenon is called magnetic Barkhausen noise (MBN) (figure 2.15) [90, 91]. This noise phenomenon can be seen on the output voltage obtained from a pick-up coil in the magnetization process of the ferromagnetic material [92]. Barkhausen noise is present in a ferromagnetic material especially the core material of fluxgate sensor. This noise is considered to have a big contribution together with the Nyquist noise of the circuitry among the limiting factors

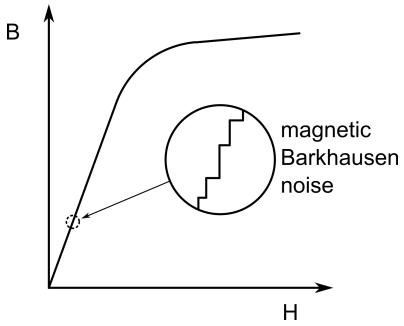

Figure 2.15: Random discontinuous increments in magnetization curve [88].

of the fluxgate sensitivity [93]. A relationship between Barkhausen noise and the excitation current was described in [87], where the Barkhausen noise increases with the excitation current. And it was also found that the increase of the sensitivity is lower than the noise when the excitation current increases. To quantify the contribution of the Barkhausen noise, a method to measure the area of the circumferential B-H loop has been proposed by [87].

2.6.4 Domain Wall Motion

In most non-magnetic materials, the magnetic moments inside the materials are all not oriented in the same direction, they are oriented in random so that the net sum is zero because they cancel each other. In ferromagnetic materials, the magnetic moments form a region called domains, which is a region inside of a material which has the magnetic moments aligned in the same direction. A magnetic domain wall is a boundary-region or interface between two magnetic domains (regions) that have different magnetization orientations [94]. One of the factors that influence the fluxgate noise is the domain wall motion [95, 96], which limits conventional fluxgate resolution. Other sources of noise are from the excitation current and signal processing of the fluxgate [87].

The theoretical noise limit of the fluxgate sensor is studied in [85] where they found that the noise limit is less than 100 fT/$\sqrt{Hz}$. The lowest achieved fluxgate noise is obtained by [19] with the noise of $\sqrt{S_B}$(1 kHz) = 400 fT/$\sqrt{Hz}$. Unlike the SQUID magnetometer or other low noise magnetic field sensors, the limiting noise of fluxgate sensor is not well understood [47].

2.7 Impedance Measurement Principle

Impedance is an important parameter, which is commonly used to characterize an electronic circuits, components, the materials used to make components, or any objects under study [97]. Impedance (Z) is defined as the total opposition of a device or circuit reacts to the excitation of an alternating current (AC) for a given frequency. The impedance is represented as a complex quantity, which is graphically shown on a vector plane. An impedance vector consists of a real part (resistance, R) and an imaginary part (reactance, X). Impedance can be expressed using the rectangular-coordinate form of $R + jX$. It can also be expressed in the polar form as a magnitude and phase angle: $|\mathrm{Z}|\angle\theta$,

$$Z = R + jX => |Z|\angle\theta. \tag{2.36}$$

Since the magnitude of impedance is similar to the resistance in DC, it can be obtained by measuring the amplitude of the voltage and current. To find the impedance components, the phase angle between the voltage and current is required. This phase angle will determine the real and imaginary part of the impedance, where the real part is

$$ReZ = |Z| \cos\theta, \tag{2.37}$$

and the imaginary part is

$$ImZ = |Z| \sin\theta. \tag{2.38}$$

In reality, there is no pure resistive or reactive components. The impedance always consists of these two components

3 Methodology and Measurement System

3.1 Design of Fluxgate Sensor

The fluxgate sensor used in this study is a racetrack fluxgate sensor with high sensitivity and low noise [18]. The Vitrovac 6025Z [98] from Vacuumschmelze is used for the core with thickness of 25 μm, width of 1 mm, 3 layers, relative permeability (μ_r) of 10^5 [99] and saturation induction of 0.58 T. The fluxgate sensor consists of three coil windings; they are two primaries (excitation) with opposite winding sense, a secondary (detection), and a compensation coil. All the coil windings are wound using 0.1 mm enameled copper wire. The geometric configuration is shown in figure 3.1.

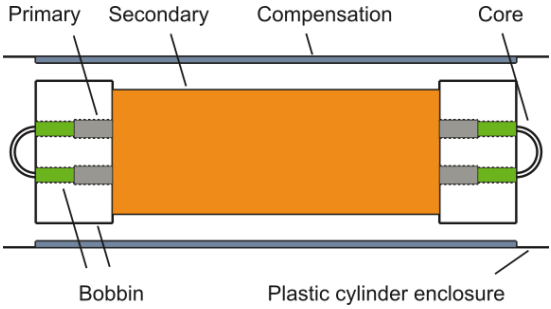

Figure 3.1: Fluxgate sensor geometric configuration.

The coil configuration circuit of the fluxgate sensor is depicted in figure 3.2. It is seen in figure 3.2(a) that both primary coils are not internally connected. The primary coils must be connected in such a way that they

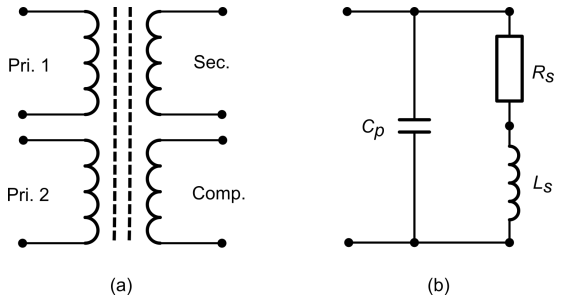

Figure 3.2: (a) Fluxgate coils configuration and (b) the equivalent circuit for each coil.

generate a magnetic field in the opposite direction, so that the generated excitation field from one coil cancels the other in the secondary coil. Each coil in the sensor is equivalent to the circuit in figure 3.2(b), where each coil consists of series ohmic resistance, inductance, and parallel capacitance. At very low frequency the ohmic resistance dominates the impedance. The reactance is increasing as the frequency increases. The influence of parallel capacitance is very small, therefore for relative low frequency it does not affect the reactance.
The primary coils are shown in figure 3.3. There are four versions of

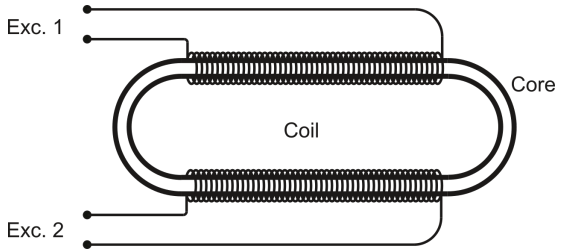

Figure 3.3: Excitation coil.

fluxgate sensors are made regarding the size and the secondary winding number. They are summarized in table 3.1. The primary coil is just made with one layer winding to avoid non-uniformity. By using 0.1 mm enameled copper wire for the coils, the possibilities of the excitation coil winding numbers are shown in the table. The lower winding number is possible due to imperfections during winding process on the bobbin. This excitation winding is wound on a 2 mm diameter PVC bobbin.
The secondary winding length is shorter than the excitation winding and placed on the middle of excitation winding. Its length are shown in the table. In order to get high sensitivity, the winding of the secondary coil consists of more than one layer. The limit of layer number is determined by

Table 3.1: Fluxgate sensors physical parameters.

Version	l_{N_p} (mm)	N_p	l_{N_s} (mm)	N_s	Sec. layer	l_{N_c} (mm)	N_c
1	25	250	20	600	4	35	285
2	25	250	20	900	6	35	285
3	55	550	50	1716	2	65	536
4	45	450	40	2741	2	55	475

the diameter of the compensation coil and the trade-off between sensitivity and parasitic capacitance. The secondary coil winding numbers are listed in the table and the illustration of the secondary coil is shown in figure 3.4. The compensation coil of the fluxgate is wound as the outermost

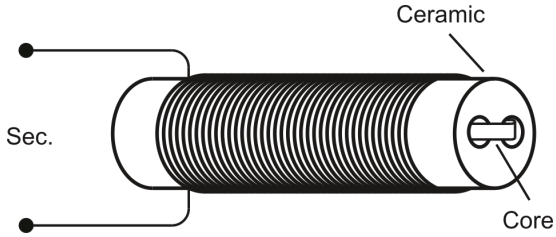

Figure 3.4: Secondary coil.

winding and encloses the others. This compensation coil is wound on the inner wall of a clear plastic tube. The compensation coil placement is quite difficult because it must be placed on the inner wall of the tube. To do this, firstly the coil is wound on a bobbin and then it must be moved to the inner wall of the tube without any damage on the coil. To make it successful, we need to make it sticky enough between turns and use some lubricant before moving it from the bobbin into the tube.
The compensation coil diameters of all versions are the same, that is 10 mm. However, the compensation coil lengths are different for each version, since the coil must enclose the secondary and excitation coils. The compensation coil length of the first, second, and third version are about 35, 65, and 55 mm, respectively, and all versions consist only of one layer. Thus, its turn number is about 285, 536, and 475 turns, respectively. The illustration of the compensation coil is shown in figure 3.5. Both primary coils are wound on the racetrack core with a 2 mm diameter PVC bobbin, which has a hole inside for core placement. The secondary coil encloses both primary coils embedded in a ceramic Alsint^{TM} 99.7 with a diameter of 7 mm. This ceramic bobbin has two holes side by side for the excitation coil placement. These holes stand with 2.5 mm distance and determine the distance between the two excitation coils. Since the bobbin for the secondary coil is fixed, the distance between the excitation coils could not

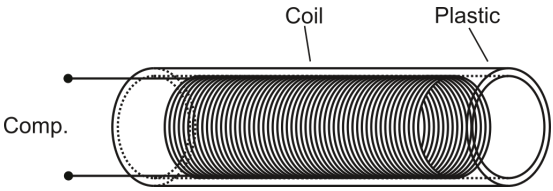

Figure 3.5: Compensation coil.

be changed except by replacing it with the another bobbin with different size. The compensation coil as the outermost coil attached to the inner wall of a clear plastic tube encloses both the primary and secondary coils. The two excitation coils are placed inside the secondary bobbin and the core material is then inserted inside these coils to form a racetrack. It connects the core from one excitation coil to the other excitation coil. This is different with the rod core sensor, which does not have a connection from the end of one core to the other. The core tape material is inserted with three layers. All the sensor coils are then glued together using resin to fix it. The coils cabling leaves each coil to have a pair cables, which for the excitation coil connections are done on the main PCB using relays. It is done in this way to vary the measurement conditions from in series or anti-series connection of the excitation coils. The size of the finished sensors itself is 40 mm in length and 12 mm in diameter for the first version, 70 mm in length and 12 mm in diameter for the second version, and 60 mm in length and 12 mm in diameter for the third version. The finished racetrack fluxgate sensors are shown in figure 3.6.

Figure 3.6: Finished fluxgate sensors.

3.2 Fluxgate Analyzer Principle

3.2.1 Hysteresis Loop

Hysteresis loop measurement of the fluxgate core is aimed to analyze its magnetization characteristics. The hysteresis loop measurement is performed by providing an AC current to a coil wound on a permalloy core. The output voltage is measured on another coil also wound on the same core. The AC current that is fed into the first coil is linear or in triangle waveform so the increment steps are constant. The measurement setup is depicted in figure 3.7. The field that is applied to the coil is

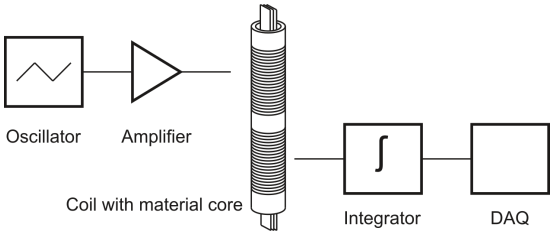

Figure 3.7: Hysteresis loop measurement setup.

proportional to the current i. The coil that is used here is a solenoid, so the field that excited the core is

$$B = \mu_0 \mu_r i n, \tag{3.1}$$

where n is the turn density. From the equation, it can be seen that the field generated in the core is proportional to the current flow in the primary coil. To measure the flux density in the core, the secondary coil was used. Based on Faraday's law, it obeys (3.2)

$$u = N \frac{d\Phi}{dt} \tag{3.2}$$

$$u = NA \frac{dB}{dt} \tag{3.3}$$

$$B_{hys} = \frac{1}{NA} \int u dt. \tag{3.4}$$

From the equations, the flux density in the core can be measured. The current is applied with a constant increment. The output voltage from the second coil is then measured. The magnetic field could be derived from the applied current and the flux density is derived from the output voltage of the secondary coil. The incremented current can be obtained from the incremented voltage source, and the current is measured at the same time. The driver signal is generated from an analog output of an National Instruments (NI) card. The shape of signal is chosen as triangle

waveform, which can be changed by a LabVIEW program. The output voltage at the secondary coil is acquired through an analog input of the NI card and processed by a LabVIEW program. The resulting data, that is magnetic field H and flux density B, could be plotted on a graph. The amplifier circuit for hysteresis loop test is the same as the circuit from figure 3.18, and for the current sensing it also uses the circuit from figure 3.19. The output voltage from the secondary coil is processed using the circuit from figure 3.23. Signal generation for hysteresis loop measurement is programmed using LabVIEW. The signal waveform is in triangle form, the maximum amplitude of the signal is below 10 mA. It should not be too big, because with the excitation coil parameter the core is already in saturation when the current in the coil reaches around 2 mA.

3.2.2 Coil Properties Characterization

The coil properties characterization comprises impedance measurement. It is performed using a circuit that delivers a reference signal to the DUT and collects the response signal at the output circuit. The reference signal can be either a voltage or current, and as the result the response is the current or voltage. Voltage and current method can be swapped through the switching mechanism, which allows the terminal change between the reference resistance (R_{ref}) and DUT. The circuit consists of a signal divider, a driver, and an auto-balanced circuit. The driver and auto-balanced circuits with a buffer are needed in order to operate the circuit with currents up to 1 A. The driver feeds the DUT with the signal from a signal source, which is generated from an analog output channel from the NI card. This driver works as a constant voltage or current source, this keeps the voltage or current across the DUT constant according the source. Then, the auto-balanced circuit makes a compensation for its input signal at the output. The block diagram of impedance measurement setup is depicted in figure 3.8. The coil properties characterization is mostly

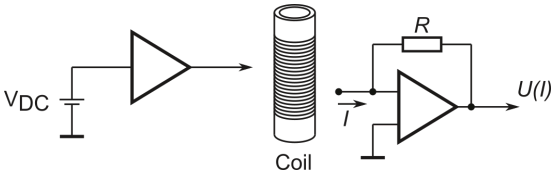

Figure 3.8: Resistance measurement setup.

performed in the unsaturated condition of the core. It would ensure the measurement to take place without the influences of core saturation, which cause incorrect measurement. Thus, the applied signal is small enough for avoiding the deformed excitation signal caused by the onset of the saturation effects [100]. Figure 3.9 shows the deformed excitation caused by the saturation effect. From the initial experiment, the saturation effect would appear at high current and/or low frequency. In this case, the

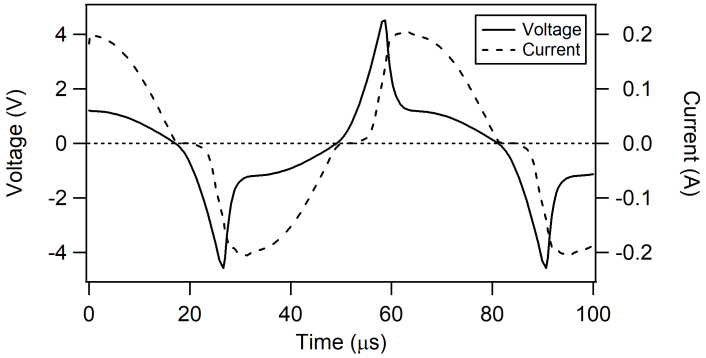

Figure 3.9: Deformed excitation signal due to saturation onset [100].

current is reduced to the limit, where the saturation effect disappears (i.e 1 mA) without omitting low frequency measurement.

DC Resistance

The ohmic DC series resistance of the coil R_s can be calculated through

$$R_s = \frac{\rho l_w}{A} \tag{3.5}$$

where l_w is the wire length, and A is the cross-sectional area of the wire. For the used enameled copper wire with 0.1 mm diameter, the resistance per length unit is 2.164 Ω/m. The length of wire in the fluxgate coils is calculated using

$$l_w = \frac{N\pi d}{\cos\theta} \tag{3.6}$$

N is the coil turns number, d is the coil diameter, and θ is the pitch angle of the coil, which is about 1°.
Resistance measurement is performed by providing voltage to the fluxgate coils and the current that arises in the coils is measured. Resistance measurement employs a DC voltage injected to the coil. The driver feeds the coil with a constant voltage and resulting the current inversely proportional to its resistance at the auto-balanced circuit. It obeys equation (3.7)

$$U_i = I \cdot R_{dc}, \tag{3.7}$$

where U_i is the input voltage to the device, I is the current, and R_{dc} is the resistance of the device. Due to the input voltage that flows in the DUT, the current arises depending on the DC resistance of DUT. The current

from the DUT is fed into the auto-balanced circuit. It then converts the current to output voltage, which is determined by equation (3.8)

$$U_o = I \cdot R_{ref}. \tag{3.8}$$

U_i and U_o are known from the measurement, while R_{ref} is also known because it is set, then R_{dc} could be calculated from

$$R_{dc} = \frac{U_i}{U_o} R_{ref}. \tag{3.9}$$

Impedance

Impedance is one of the coil parameters, which describes a measure of reaction to alternating current (AC). The impedance is an extension concept of resistance in AC circuits. It involves the relation not only between the amplitude of voltage and current but also the comparison of phase between them. An impedance measurement signal is shown in figure 3.10.

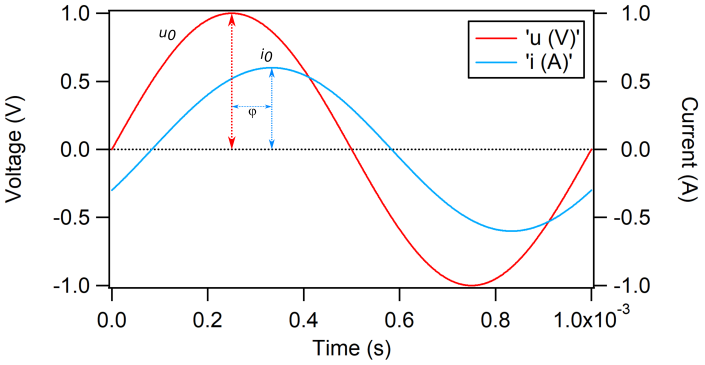

Figure 3.10: Impedance measurement signal.

Impedance is defined as the ratio between complex amplitudes of voltage and current and it is also notated as complex number. The magnitude of the impedance is the ratio of the magnitudes of voltage and current, and the phase of the impedance is the phase shift between voltage and current. Impedance is represented with complex number $\tilde{Z}$, which can be represented in polar or cartesian form. In polar form, the impedance is represented as

$$\tilde{Z} = Ze^{j\varphi} \tag{3.10}$$

and in cartesian form it is represented as

$$\tilde{Z} = R + jX. \tag{3.11}$$

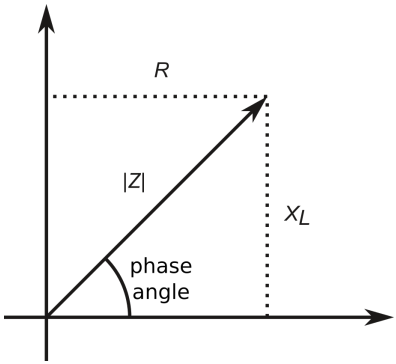

Figure 3.11: Complex impedance.

The real part R is the resistance and the imaginary part X is reactance. It is sometimes easier to work with polar form like in multiplying and dividing, and sometimes easier using cartesian form when working on adding and subtracting. When substituted in Ohm's law, it is becoming

$$\tilde{Z} = \frac{\tilde{Z}}{\tilde{I}} = \frac{u_0 e^{j(\omega t+\varphi_1)}}{i_0 e^{j(\omega t+\varphi_2)}} = Z e^{j\varphi} \tag{3.12}$$

where

$$Z = \frac{V}{I} \tag{3.13}$$

and

$$\varphi = \varphi_1 - \varphi_2. \tag{3.14}$$

The impedance may vary depending on the frequency, and its value can be calculated from

$$|Z| = \sqrt{R^2 + X^2} \tag{3.15}$$

where

$$X = X_L - X_C \tag{3.16}$$

$$X_L = \omega L \tag{3.17}$$

and

$$X_C = \frac{1}{\omega C}. \tag{3.18}$$

Self-Capacitance

The self-capacitance of a solenoidal coil C_{sc} can be calculated by Medhurst [101].

$$C_{sc} = \frac{4\varepsilon_0}{\pi} l[1 + 0.8249(d/l) + 2.329(d/l)^{3/2}] \tag{3.19}$$

where ε_0 is the free space permittivity, l is the coil length, and d is the coil diameter. In this study the capacitance is not taken into account, because it is very small and has minor effect in the frequency range applied.

Inductance

Inductance measurement is performed by measuring the magnitude comparison and phase difference of the voltage and current from the coil. Since the impedance of the coil can be obtained from magnitude comparison, the inductance can be calculated with the known phase difference between voltage and current.
As long as the core is not driven into the saturation regime and for the excitation frequencies, where the skin effect on the ferromagnetic core is negligible, the equivalent circuit model is simple. For much higher excitation frequencies (f >100 kHz) apart of eddy currents, the complex permeability changes with frequency also due to limited domain wall mobility and other viscous effects. In this case the inductance of coil does not change because the permeability is constant due to low excitation current and low frequency employed. But if the core is driven into the saturation regime or driven with high frequency, the change of permeability must be considered. The inductance of a solenoid-shaped coil can be approximated through [102]

$$L_s = \frac{\mu_0 \mu_A N^2 A}{l} \times k_L \tag{3.20}$$

where L_s is the series inductance, μ_A is the apparent permeability of the core, A is the core cross-sectional area, l is the coil length, and k_L is the Nagaoka's coefficient.
Inductance is associated with the imaginary part of the impedance. The complex diagram of inductance is depicted in figure 3.12. The imaginary value of inductance is positive, then the impedance equation of an inductive device could be written as

$$Z_L = R_L + jX_L, \tag{3.21}$$

where Z_L is the inductor impedance, R_L is the resistance of the inductor, and X_L is the reactance of the inductor. If the impedance is converted to polar form, it is becoming

$$Z_L = |Z|(\cos\varphi + j\sin\varphi), \tag{3.22}$$

and the inductor reactance is

$$X_L = |Z|\sin\varphi, \tag{3.23}$$

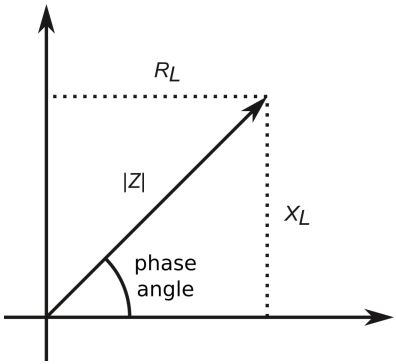

Figure 3.12: Complex diagram of inductance.

from the equation above and the inductance of the coil can be measured with known impedance and phase difference.

Mutual Inductance

Faraday's law of magnetic induction states that a changing magnetic flux through a coil of wire with respect to time will induce an EMF in the wire. In a coupled circuit, there are two coils of wire; a primary coil that is connected in series with the voltage source, and a secondary coil that is not connected to any voltage source. The secondary coil receives energy only by induction. The EMF in the secondary coil affects the voltage across the primary coil due to reflected impedance if there are two coils with a cylindrical form with a radius R_{av} and a length l, the distance between the centers of two coils d_{coil}, and the number of turns (N) of the coils 1 and 2 is the same. The magnetic field produced by coil 1 (current I_1) at the center of coil 2 is given by

$$B = \frac{\mu_0}{2\pi}\frac{NA}{d_{coil}^3} I_1 \tag{3.24}$$

for $d_{coil} \gg R_{av}$ using the Biot-Savart law. The voltage induced in coil 2 is

$$V_2 = -N\frac{d\Phi}{dt} = -NA\frac{dB}{dt} = \frac{-\mu_0 N^2 A^2}{2\pi d_{coil}^3}\frac{dI_1}{dt} \tag{3.25}$$

where the magnetic flux is $\Phi = BA$ and A is the cross-sectional area of the solenoid ($A = \pi R_{av}^2$). Thus, the mutual inductance M defined by $V_2 = -MdI_1/dt$ is given by

$$M = \frac{\mu_0 N^2 A^2}{2\pi d_{coil}^3}, \tag{3.26}$$

and the ideal self-inductance L_0 is given by

$$L_0 = \frac{\mu_0 N^2 A}{l} \tag{3.27}$$

for sufficiently long l, where l is the length of the solenoid, μ_0 ($4\pi \times 10^{-7}$Tm/A) is a permeability, and N is the total number of turns. Thus, we have

$$k = \frac{Al}{2\pi d_{coil}^3} = \frac{R_{av}^2 l}{2d_{coil}^3} \tag{3.28}$$

since $M = kL_0$, The constant k is dependent only on the geometry of the coils. The mutual inductance M is related to the self inductance L by

$$M = k\sqrt{L_1 L_2} \tag{3.29}$$

where k is a constant and smaller than 1 [103].

3.2.3 Sensitivity and Noise Characterization

Sensitivity

The side-band sensitivity of the sensor is directly measured at the output of the sensor and it is measured with the presence of an AC external field. The side-band sensitivity appears beside the second harmonics of the excitation frequency. The difference to the second harmonic is the frequency of the external applied field. If the excitation frequency is 15.625 kHz and the frequency of external applied field is 63 Hz, then the side-band frequency is 31.25 kHz ± 63 Hz.

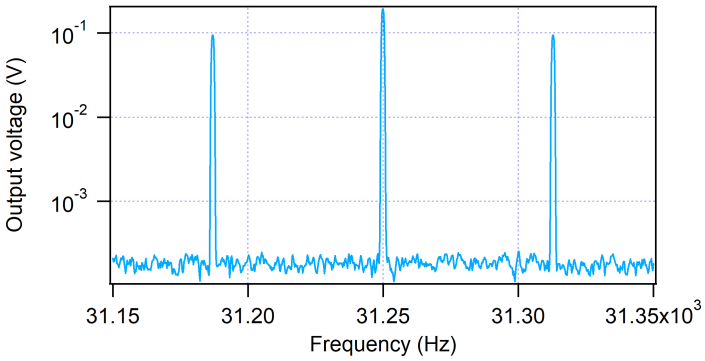

Figure 3.13: Side-band output voltage measurement.

The side-band sensitivity S_{sb} is calculated from

$$S_{sb} = \frac{U_{eff,2f_0 \pm f_m}}{B_{eff,2f_0 \pm f_m}} \tag{3.30}$$

where U_{eff} is the effective voltage, and B_{eff} is the effective field. U_{eff} value is derived from the side-band amplitude and B_{eff} is derived from the coil constant of field generating solenoid. The current that flows in the solenoid and the sensitivity of electronic output are also measured. The frequency of the signal at this point is brought back to the source field frequency because of the processing in the phase sensitive detector and integrator. The output sensitivity S is determined by

$$S = \frac{U}{B}, \tag{3.31}$$

where U is the voltage and B is the magnetic flux density.

Symmetry

The excitation coils have the same size and they are positioned symmetrically with respect to the secondary coil. The symmetrical design allows the field from both excitation coils being the same respect to secondary. The symmetry of coils coil can be measured through mutual inductance measurements.

Noise Level

The noise level of the fluxgate sensor is the total noise from all contributors. Noise level measurement is conducted in a good shielded environment. When characterizing the sensor, it is placed inside the shielding box and no external field applied. The noise level can be calculated from

$$S_B^{1/2} = \frac{S_v^{1/2}}{S}. \tag{3.32}$$

In a fluxgate sensor system, the noise is fed back in a loop. The noise from the sensor might be converted to voltage noise in the amplifier, and then this noise coupled back to the sensor through the compensation coil, which has a coil factor. The noise from the electronic is converted back to field noise in the sensor. Noise feedback is the conversion process of

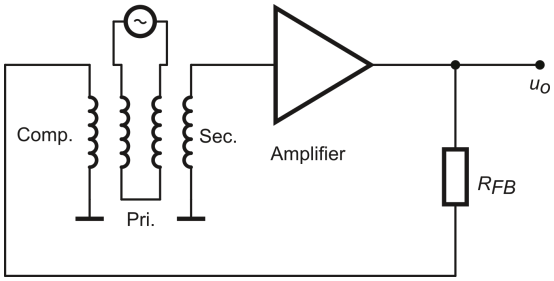

Figure 3.14: Noise loop.

the noise from voltage form to current form, then to field form and back to voltage form. If the noise limit of the sensor is around 100 fT/$\sqrt{Hz}$ and the sensitivity of the sensor is 2×10^5 V/T, then the output noise at the electronic should not be more than 20 nV/$\sqrt{Hz}$. The feedback resistor, compensation coil resistance and compensation coil factor should be determined to match with the noise limit of the sensor:

$$\sqrt{S_v} = \sqrt{S_{B_C}} \cdot S \tag{3.33}$$

where $\sqrt{S_v}$ is the voltage noise, $\sqrt{S_{B_C}}$ is the noise of magnetic field at the compensation coil, and S is the sensitivity of the fluxgate sensor.

3.3 Measurement System

The measurement system consists of hardware and software. The hardware is divided into three parts, that is an electronic circuits for the impedance characterization of the fluxgate sensor, the fluxgate magnetometer (FGM) system, and the DAQ card. The performance evaluation of the FGM system is carried out on its sensitivity and noise, these are the very important parameters in magnetic sensor evaluation. These parameters specify the quality of the fluxgate sensor. The software has a combination of the impedance and performance function. Its operation can be selected on the PC through the software. The block diagram of the hardware is depicted in figure 3.15. The hardwares of fluxgate impedance

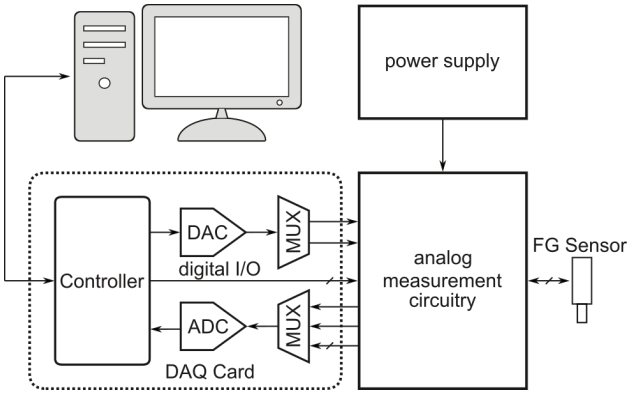

Figure 3.15: Block diagram of measurement system.

and FGM performance are alternately connected to the fluxgate sensor using a relay switching system. Therefore, the fluxgate impedance and FGM performance characterization can not be done at the same time. The realized measurement system is shown in figure 3.16.

Figure 3.16: Photograph of measurement system.

3.3.1 Electronics for Impedance Characterization

Voltage Divider and Driver Circuit

Impedance measurement of a fluxgate sensor is carried out by providing an excitation signal to the DUT and obtaining the output response signal from the DUT. Here, the excitation signal can be swapped between constant voltage and current signals to allow a voltage or current mode measurement. An electronic circuit is needed to characterize the DC resistance, impedance, inductance, and mutual inductance of the fluxgate coils. The characterization of these parameters can be done using the same circuit since these measurements have the same basic principle. Because the DUT is a low impedance device, the driver circuit must have low output impedance, so that the voltage signal can be delivered to the DUT without loading and distortion. For the current measurement, an auto-balanced circuit with low output impedance has also been used. The impedance measurement block diagram is depicted in figure 3.17. When the voltage mode measurement is implemented, the fluxgate is driven with a voltage source and the output current is measured. The same procedure is also applied for current mode measurement, but the driving and response signal are on the opposite parameters to the voltage mode measurement. The DC resistance measurement uses the DC signal and the other measurements use the AC signal. As a consequence, the circuit should be able to provide DC and AC signals. The driver circuit is built by using MOSFETs. The op-amp were used to drive the MOSFETs with negative feedback at the op-amp. The transistor circuit is used as the constant current source of the first stage of the MOSFET. This MOSFET pair ensures that the voltage bias at the second stage is the same with its characteristics because originated from the same MOSFET. Due to the feedback setting, this circuit is a non-inverting circuit.

The circuit consists of an input signal divider, a driver for the DUT, an auto-balanced circuit, and a signal processing for each output for U_i

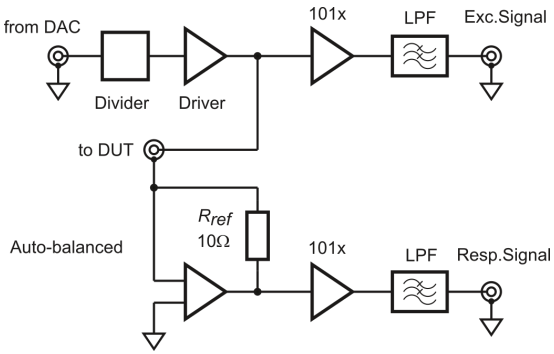

Figure 3.17: Block diagram of analog measurement circuitry with the 2nd order LPF and its -3dB frequency of 33 kHz.

or $\hat{u}_i$ and I_o or $\hat{i}_o$. A voltage divider at the input with an attenuation factor of 1/101 is used for dividing the large signal from the DAC. We prefer to use a large signal from DAC instead of a small signal to provide better SNR without distortion at the output when using small signals. The driver is designed to have low output resistance below 1 Ω to deliver the currents up to 1 A although in our experiment the current has not been more than 100 mA. The output driver and auto-balanced circuit are built with a combination of two op-amps TL071, four MOSFET transistor pairs IRF530 and IRF9530, and some passive components for bias current source. The use of MOSFET as the driver is aimed to take its advantages over BJT in this application. The main advantage is its very low drain-source on-resistance (R_{DS}). This allows the voltage drop (V_{DS}) becoming smaller than V_{CE} on BJT and providing larger currents and output voltage range. The other advantages are the protection diode on the MOSFET and its better temperature stability. The driver circuit has two pairs of MOSFETs, where the first one is aimed to shift the op-amp's output to MOSFET's threshold voltage V_{th} to avoid distortion at the MOSFET's output, and the second one is aimed at driving the load. As mentioned above, the two first parts of the impedance characterization circuit are the divider and driver. The circuits of these parts are shown in figure 3.18.

Auto-balanced Circuit

The second part is the auto-balanced circuit. It generates the response signal from the fluxgate sensor. The auto-balanced circuit is shown in figure 3.19. An auto-balanced circuit converts the current that flows in the DUT to a voltage using a feedback resistor R_{ref} with a value of 10 Ω. The use of an auto-balanced amplifier ensures that the current output is a ground-referenced signal and the phase is shifted by 180 degrees. The phase shift is shifted back 180 degrees by software in the LabVIEW.

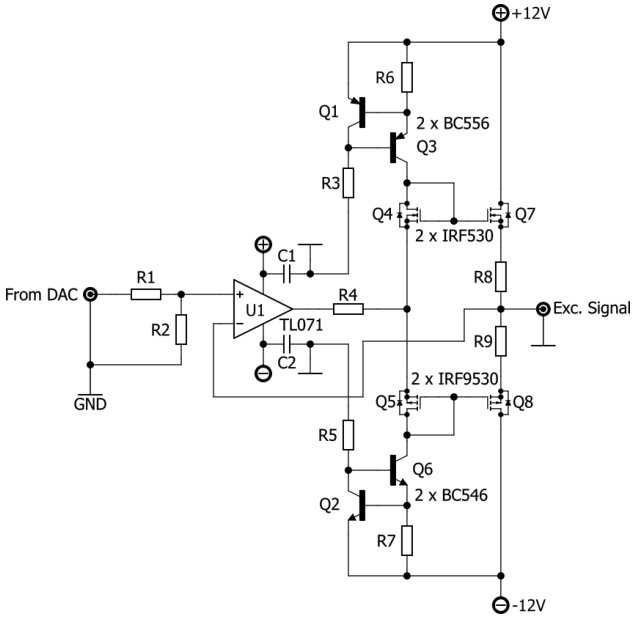

Figure 3.18: Divider and driver circuit.

The power MOSFET is also used as the power stage of the auto-balanced circuit to bear the load instead of the op-amp. The reason of using these power MOSFETs here is the same as the MOSFET in the driver circuit. The trans-impedance circuit converts the current from the DUT to a voltage. Because the configuration of the circuit is inverting, the polarity of the output voltage will be shifted by 180 degrees. The schematic diagram of the voltage divider, driver, DUT and R_{ref} placement, and auto-balanced circuit are shown in figure 3.20.

Signal Processing Circuit

Signal processing circuits for excitation and response signals are made with identical stages to ensure the frequency responses are the same within the working frequency range. Each circuit consists of a voltage amplifier with non-inverting gain of 101 for compensating the attenuation at the divider circuit and one anti-aliasing filter for removing the noise above the maximum applied frequency. Two op-amps with high GBW and low noise characteristic are used for the voltage amplifier and filter. The OPA2228 op-amp is chosen because of its high GBW of 33 MHz and low noise of 3.5 nV/$\sqrt{Hz}$ at 10 Hz. The filter used is a second order Butterworth with a corner frequency of about 33 kHz. The circuit is shown in figure 3.21. To evaluate the similarity of the circuits, a dynamic signal analyzer

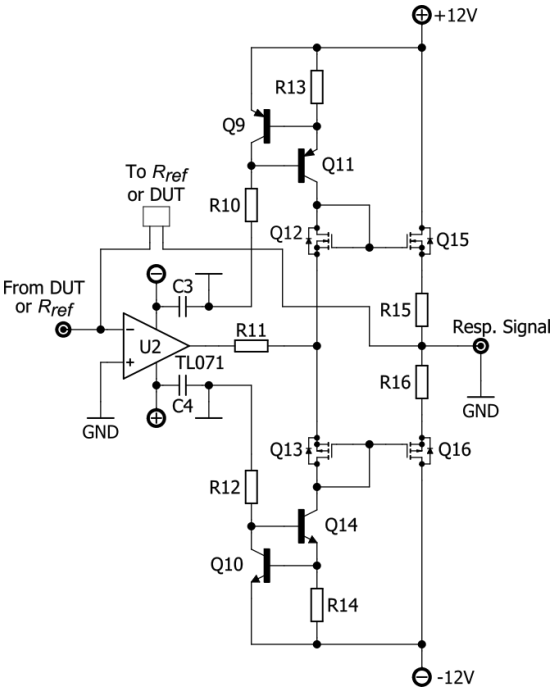

Figure 3.19: Auto-balanced circuit.

Agilent 35670A has been employed. The frequency response of the signal processing is compared. In figure 3.22 the gain and phase difference of the signal processing circuits are shown. The gain difference is a little bit below zero with the average value of -0.04 dB and relatively constant along the bandwidth of the circuit (0 to 33 kHz) as can be seen in figure 3.22. The figure also shows the phase difference of the circuits. It is laying at zero and relatively constant along the bandwidth of the circuit. Therefore, the circuits does not affect the absolute impedance and phase measurement in the frequency range. However, the bandwidth of the circuit covers the aimed frequency range for fluxgate sensor inductance measurement, which is ranging from 0 to 31.25 kHz. This ensures that there is no circuit influence on the inductance measurement.

Mutual Inductance Signal Processing

Mutual inductance measurement employs two coils so that their mutual inductance is measured. Different from inductance measurement, mutual inductance obtains the voltage from the second coil. Thus, there are two coils employed. The current is fed into the first coil, and the voltage is

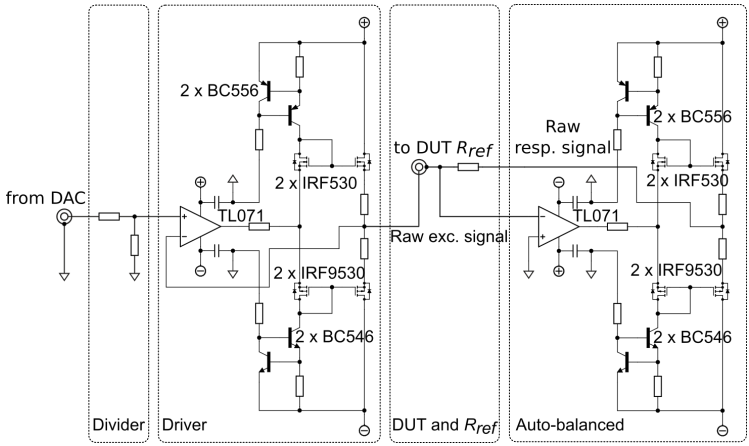

Figure 3.20: Detailed schematic diagram of voltage divider, driver, DUT and R_{ref} placement, and auto-balanced circuits.

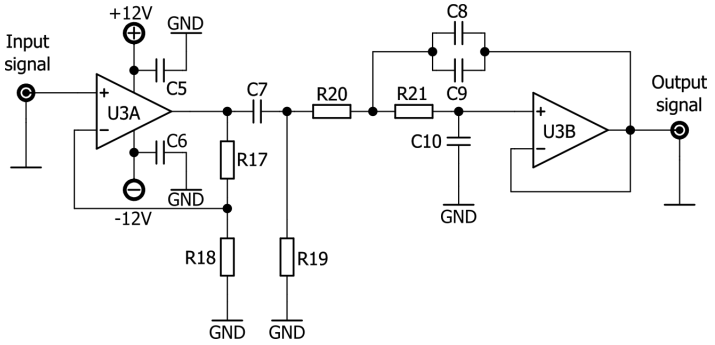

Figure 3.21: Signal processing circuits.

obtained from the second coil. In order to measure the mutual inductance, a signal processing circuit was also provided to process the output voltage from the second coil. This circuit is generally the same with the signal processing circuit in figure 3.21. But there is one additional resistor at the input provided as the input load. The circuit is depicted in figure 3.23. All the output voltage of the above circuits is filtered using a Butterworth low-pass filter with Sallen-Key topology. The pole of this low-pass filter can be calculated from

$$f_p = \frac{1}{2\pi\sqrt{R_{26}R_{27}(C_{14}\|C_{15})C_{16}}} \tag{3.34}$$

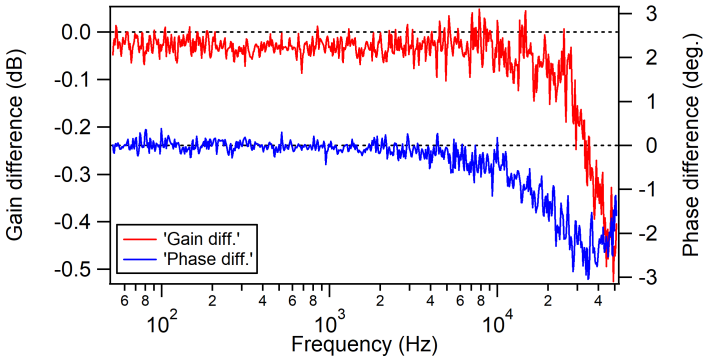

Figure 3.22: Gain and phase difference of signal processing circuits.

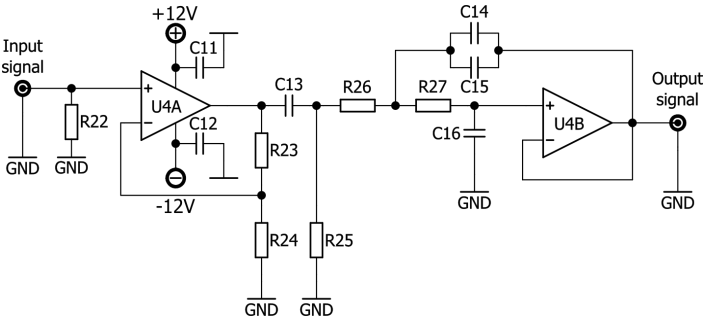

Figure 3.23: Buffer circuit for mutual inductance measurement.

It is seen that C_{14}, C_{15} and C_{16} must have the same value in order to create a quality factor Q value of 0.7071 for Butterworth filter characteristics.

3.3.2 Electronics for Sensitivity and Noise Characterization

The electronic circuit for fluxgate sensor sensitivity and noise characterization is the electronic circuit with which the fluxgate sensor operates as a FGM system. This electronic circuit converts the external magnetic field to an output voltage. The sensitivity and the noise of the fluxgate are measured via the output voltage. The main parts of circuits are a signal generator for the excitation and a signal processor for the sensor output signal processing.

Excitation Circuit

The excitation signal is generated from a quartz crystal. The use of quartz is aimed to ensure that the signal has a stable and accurate frequency and also has low jitter. The signal output is in square waveform with TTL level. The frequency of the quartz is 4 MHz, then divided to the kilohertz regime using a CMOS frequency divider to meet the desired operation frequency of fluxgate sensor. In this study the used excitation frequency is 15.625 kHz and the phase sensitive detector operates at 31.25 kHz. Figure 3.24 shows the excitation signal generator circuit. The maximum excitation

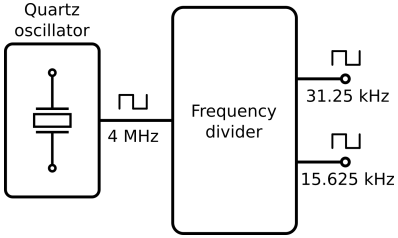

Figure 3.24: Clock source and divider block diagram of excitation circuit.

current is about 1 A_{pp}, a driver is needed to buffer the excitation current. A H-bridge MOSFET as shown in figure 3.25 is implemented as the driver for the excitation signal. The excitation current is adjustable and can be done by controlling the voltage source on the MOSFET. Since the driver is in H-bridge configuration, the output voltage of the excitation is $2V_{CC}$.

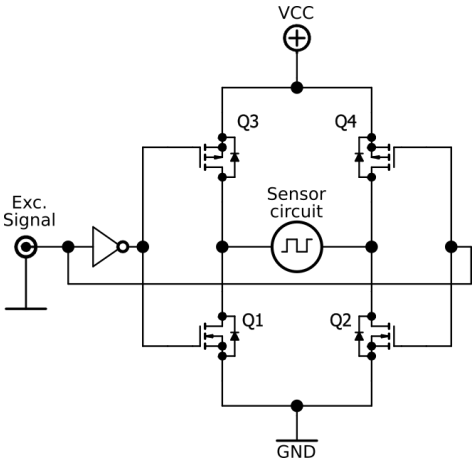

Figure 3.25: Excitation signal driver circuit.

Excitation Tuning

The excitation coil has its own impedance characteristics. It has a specific resonance frequency due to its characteristic. A tuning is needed to maximize the current peak and to narrow the current signal as it is the best for the fluxgate sensitivity and energy consumption [104]. Therefore, a combination of resistor and capacitor circuit are utilized to change the signal shape. The parallel capacitor tuning is suitable for current source mode excitation, while the series capacitor tuning is suitable for voltage source mode excitation. Therefore, the series capacitor tuning is used in this study, since the voltage source mode is chosen.

Phase Sensitive Detector

The signal from the sensor is tuned to match it to the $2f_{exc}$ frequency. The tuning uses a capacitor in parallel with the secondary coil. Sometimes a resistor is used in parallel to reduce the quality factor Q of the circuit to make it more stable. The effect of correct tuning can be seen from the height similarity of sideband signal magnitude at $2f_{exc}$ frequency, since the sideband signal is symmetric with respect to this frequency. An

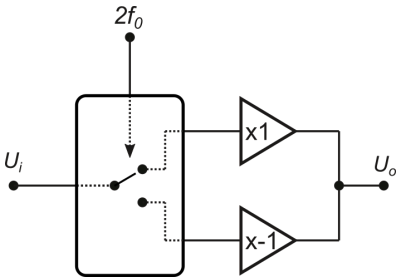

Figure 3.26: Phase sensitive detector block diagram.

amplifier buffers the signal from the tuning circuit and amplifies the signal with the gain of 3. This amplifier is needed to ensure that the signal is buffered before it is fed to the phase sensitive detector (PSD). At the PSD the second harmonic of the signal is extracted based on $2f_{exc}$ referencing frequency. The second harmonic signal is then added and integrated to a DC signal. As the feedback circuit it uses a voltage to current converter. The current from this circuit drives the compensation coil to compensate the field to be measured.

Integrator

An integrator is used to convert the rectified signal from the PSD to a DC voltage. It is built from a second order Butterworth low-pass filter with a cutoff frequency being much smaller than the $2f_{exc}$ frequency. Figure 3.27 shows the integrator circuit for the sensor system.

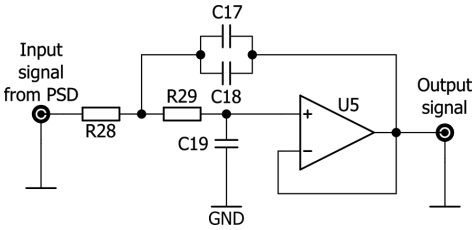

Figure 3.27: Integrator circuit.

Voltage to Current Converter

The voltage to current converter converts the output voltage to a current for feedback on the compensation coil. The circuit of the voltage to current converter is shown in figure 3.28. The feedback current is determined by

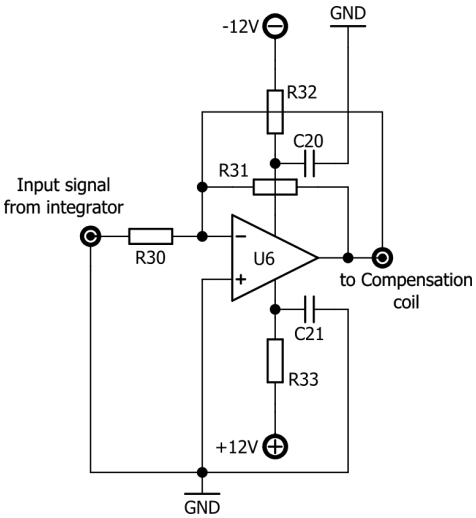

Figure 3.28: Voltage to current converter circuit.

the compensation coil constant and the converter resistance R_{30}. First, a field measuring range should be determined. The maximum current can be obtained from the field range using the coil constant:

$$i_{fb,max} = \frac{B_{max}}{k_{comp}} \tag{3.35}$$

Then, the converter resistance R_{30} can be calculated from the maximum current and the maximum output voltage:

$$R_{fb} = \frac{U_{o,max}}{i_{fb,max}} \tag{3.36}$$

3.3.3 Switching Circuit

The switching circuit connects the sensor either to the sensor impedance characterizer or to the FGM system characterizer. This circuit consists of 12 relays arranged in matrix form that connect four coils in the sensors to both characterizers. Therefore, in one plugging connection, both characterizations can be performed automatically using the LabVIEW program started from the display.
The switching circuit is shown in figure 3.29. There are three rows and four columns of relays. In the application, any coil in the sensor could be connected to any circuit with the logics that control the relays. The sensor characterizer, which consists of signal source, auto-balanced, and mutual inductance signal processing circuit are connected to the first two rows of relays, while the FGM system characterizer circuits are connected to the third row of relays. For example, the pick-up coil could be connected to

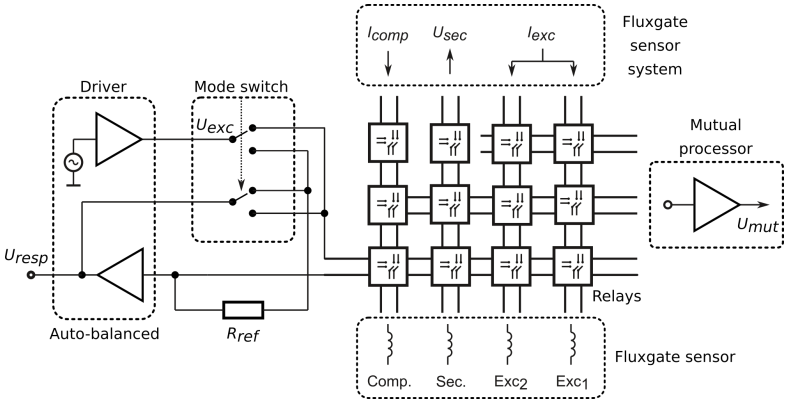

Figure 3.29: Switching system for impedance, sensitivity and noise measurement.

the voltage source when measuring DC resistance, impedance, inductance, and mutual inductance. But, when measuring mutual inductance from the first coil, the pick-up coil should be connected to the output voltage processor, and the first coil is connected to the voltage source. Then, the third connection is its functionality as fluxgate output signal source from the sensor.
The relays are controlled by TTL logics from the DAQ card through a serial to parallel converter. The serial bus is intentionally used to save the

Table 3.2: Function codes for switching relays.

Function	Code	
	Decimal	Binary
Pri. 1 resistance & impedance	1	0000 0000 0001
Pri. 2 resistance & impedance	2	0000 0000 0010
Sec. resistance & impedance	4	0000 0000 0100
Comp. resistance & impedance	8	0000 0000 1000
Pri. 1 - pri. 2 mutual inductance	33	0000 0010 0001
Pri. 1 - sec. mutual inductance	65	0000 0100 0001
Pri. 1 - comp. mutual inductance	129	0000 1000 0001
Pri. 2 - sec. mutual inductance	66	0000 0100 0010
Pri. 2 - comp. mutual inductance	130	0000 1000 0010
Sec. - comp. mutual inductance	132	0000 1000 0100
Open loop FGM	1280	0101 0000 0000
Closed loop FGM	3328	1101 0000 0000
Open loop FGM - pri. coils reversed	1792	0111 0000 0000
Closed loop FGM - pri. coils reversed	3840	1111 0000 0000

line. The converter is built by two TTL ICs 74HC595, where one IC can provide one byte parallel line data. The relay index is started from the right-bottom corner to the left in figure 3.29. Thus, the last index is the relay at the left-upper corner. Therefore, if the inductance measurement of excitation coil 1 is desired, then the binary code of converter output must be 0000 0000 0001. The codes of operation are summarized in Table 3.2.

3.3.4 DAQ System

The analog circuit is controlled by a program using LabVIEW, which runs on a PC. The interface NI-DAQ PCI-6221 card is employed for data acquisition. Figure 3.15 shows the block diagram of the system. In the figure, there is a card for data acquisition, which contains a 16-bit ADC and a 16-bit DAC with a sample rate and an update rate of 250 ksps/ch and 833 ksps/ch, respectively. No internal amplification is used here. One channel of the DAC and two channels of the ADC are needed for the measurement. The DAC is used as an excitation voltage source and the ADC's channels are used for voltage and current acquisition.

3.3.5 Magnetic Field Source

A solenoid is used as the source of the test magnetic field for the fluxgate sensitivity and noise characterization. The solenoid is driven using an op-amp. Its signal offset, amplitude, waveform, and frequency can be set from the LabVIEW program. An NI card is used to drive the op-amp through an analog output channel. The solenoid bobbin is made of

PVC material, which is without magnetic influence. The diameter of the solenoid is 50 mm and the length is 100 mm. Enameled copper wire with 0.25 mm diameter is used as the coil wound in one layer. The winding of the solenoid contains 364 turns. The magnetic field generated by this solenoid is characterized using a Hall effect gaussmeter FW Bell 5180 in order to know its coil factor. Based on the measurement as shown in figure 3.30, the obtained coil factor of the solenoid is around 4.03 μT/mA. It is seen that the measurement result contains a magnetic field offset coming from the residual Earth magnetic field. Since the magnetic field source

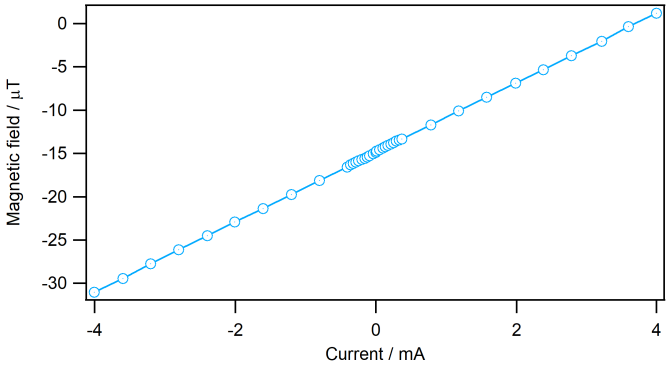

Figure 3.30: Coil constant measurement.

is an air core solenoid, therefore the permeability constant is free space permeability. The resulted magnetic flux could be calculated through the equation

$$B = \mu_0 i l, \tag{3.37}$$

where l is the flux line length. Based on this equation, the coil constant could be also calculated. With the values provided above, the coil constant obtained from the calculation is 4.58 μT/mA. This value is rather larger than the measured one due to the non-ideal solenoid used, which is not long enough, so that the homogeneity of the generated magnetic field at the center is not achieved.

3.3.6 Magnetic Shield

Magnetic fields from a power source with flux densities in the range of 1 - 100 μT could arise around electrical device as the power source containing switching system and transformers. The generated magnetic field can cause interference on nearby electrical equipment, such as jitter on video display units (VDU) on a computer [105]. One way of reducing the magnetic fields from such electric installations is to apply a shield around the sources.

A magnetic shield is used to reduce the background magnetic field and protect the measuring equipment and experiments from environmental DC and AC magnetic field disturbances. Magnetic shielding is usually realized as a case that encloses the system and made from permalloy [106, 107]. The shielding factor is defined as the ratio of the magnetic field magnitude without and with shielding for the same field and location. It is shown in equation 3.38 [107–109].

$$S_f = \frac{B_0}{B_i} \tag{3.38}$$

The best shielding for obtaining the same and high shielding factor in all directions is a spherical shield [110]. In contrary, the spherical shielding is more expensive than the flat edge permalloy. However, there have been made some spherical shielding with successful realizations of permalloy sheets [111, 112], but the majority of large size shields are box-shaped. For the same wall thickness, the shielding factor of a high-permeability enclosure is inversely proportional to the size of the shield [113]. The static shielding factor of a single cubic shielding layer at the central point can be estimated by using [108]

$$S_{f_{cube}} \approx 1 + 0.8 \left(\frac{\mu_r d}{L} \right). \tag{3.39}$$

When characterizing the fluxgate sensor, the measurement is performed in a shielding case to minimize the influence of magnetic fields from outside that can cause errors. The shielding case is made from the mumetal with high permeability. The cubic shape is chosen for the geometry of shield with the length, width, and height of 15 cm. The measurement of the shielding factor is performed using a large square Helmholtz coils and a commercial fluxgate sensor Mag-03MCL100 from Bartington Instruments [114]. The implemented frequency is ranging from 1 Hz to 10 kHz with logarithmic increments, and the signal amplitude is kept constant at 1 V_{pp}. The measurement result is shown in figure 3.31. It is seen from the graph that the shielding factor decreases with increasing frequency. It decreases from around 200 at 1 Hz to around 10 at 10 kHz. This phenomenon is seen rather odd, since the shielding factor should increase by the increasing frequency due to eddy current. This phenomenon is probably caused by the geometry of the shielding case and a quite big hole on one side of the case that is parallel to the magnetic field source [115].

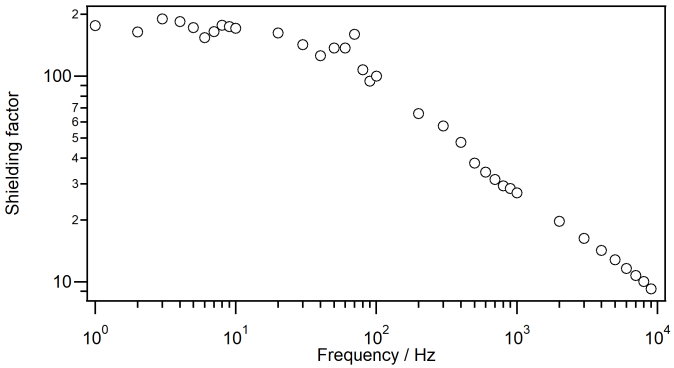

Figure 3.31: Shielding factor measurement.

4 Measurement Results

4.1 Fluxgate Sensor

Several fluxgate sensors were made and utilized to measure their properties. Several fluxgate sensors were built and characterized in the experiment. The fluxgates are varied with different primary and secondary coil configurations and also with different geometries. The coils are wound using a winding machine, whose speed can be adjusted and which has a counter to count the winding number.
When constructing the fluxgates, the primary coils are wound first, then the secondary coil and compensation coil. The primaries are fitted into the two holes inside the Alsint^{TM} ceramic and then the core material is inserted into the two primaries to form a racetrack. The secondary coil is wound on the ceramic before the primaries are fitted. The compensation winding is placed inside a plastic tube as the tube is the outermost shield of the fluxgate body. After the compensation coil is fitted, the secondary coil with the primaries are inserted into the compensation coil. They are all glued with resin to fix all the coils in the sensor's body.

4.2 Fluxgate Impedance Measurement

A fluxgate analyzer (FG Analyzer) with low output impedance and low excitation current capability is designed for fluxgate sensor characterization to analyze the impedance and symmetry of the geometric configuration. Impedance and geometry configurations are important parameters for examining their influence on fluxgate sensitivity and noise [19]. Impedance, which consists of ohmic resistance, inductance, and capacitance of the fluxgate are measured using the analyzer. Since the effort of future fluxgate sensor development is miniaturization and integration with the electronics [20], it implies the utilization of small limited winding numbers of fluxgate sensor coils causing the impedance of the coils to lie in the range below 100 Ω. The core material of fluxgate easily saturates even at low currents due

Table 4.1: Physical parameters of the used fluxgate sensors for impedance measurement.

Coil	FG-02			FG-03		
	N	l_{wd}(mm)	d_{wd}(mm)	N	l_{wd}(mm)	d_{wd}(mm)
Pri. 1	208	25	2	208	25	2
Pri. 2	208	25	2	208	25	2
Sec.	621	20	7.7	929	20	7.7
Comp.	263	35	9.7	300	35	9.7

to its high permeability causing the change of core permeability, which in turn changes the impedance. The change of excitation current could happen because of the increase of coil impedance. In order to provide the same magnetic field, the excitation current must be kept constant. The other properties must also be considered, such as the dependence of permeability on frequency and bias magnetic field strength [21, 22]. In addition, the influence of the ratio of sampling frequency and sampled frequency must also be considered.
The aim of the work is to provide an instrument with special characterization purpose for fluxgate sensors, which has special characteristics. The designed system is based on an auto-balanced amplifier, which generally offers a wide impedance measurement range from millihertz to hundreds of megahertz [23]. The designed auto-balanced circuit is simpler compared to other design described in [23–25]. It accommodates the impedances measurement with the ability of measuring low impedance with low current. The circuit also implements the identical signal processing stages for voltage and current output for high precision. The ohmic resistance, impedance, and inductance of each coil in the fluxgate sensor are measured. The parameters of the used sensor for fluxgate impedance measurement are listed in table 4.1.

4.2.1 Calibration

Although the circuit's influence on the impedance measurement could be neglected, a calibration is still needed to accommodate the offset and the frequency-dependent gain and phase difference reading errors at the fixed DAQ sample rate [116]. Since only one range of R_{fb} is used, the error caused by the range switching is not taken into account. The measurement system calibration employs the linear measuring system with an offset as described in [117, 118]. Rewriting the equation of the calibration provides

$$Z_o = c_1 Z_i + c_2, \tag{4.1}$$

where Z_o is the output value, Z_i is the input value, c_1 is the coefficient as calibration factor, and c_2 is a constant as offset error. This general equation is implemented to calibrate the ohmic resistance and inductance

measurements. To validate the calibration and to see how large the error is, the error calculation is carried out through the following equation

$$Error = \left(\frac{Measured\ value - Ideal\ value}{Ideal\ value} \right) \times 100, \tag{4.2}$$

where *Measured value* is the value after calibration and *Ideal value* is the calibrated value of the multimeter and the impedance analyzer.

4.2.2 DC Resistance

DC Resistance Measurement

DC resistance measurements are performed utilizing a LabVIEW program in the PC using equation (4.4). The DC resistance is measured by providing a steady DC excitation signal (U_i or I_o) into the coil and the DC response signal (I_o or U_i) is then measured. The measurement process is carried out by increasing the excitation signal. Here, the constant voltage excitation signal is used because some coil resistances are high enough to require higher voltage if constant current is applied. The input voltage range is ranging from negative to positive values of the input voltage setting point. It is made bipolar involving positive and negative values in order to eliminate the offset effects caused by the EMF. For each measurement 100 data points are collected and the excitation voltage is evenly distributed between -U_i and +U_i. By using this method, it's expected that the measurement results would have a small error due to a large enough number of measurement data. In the operation, a delay of 0.5 s between the subsequent data points is implemented to let U_i or I_o settle. It is intended to make a break between the measurements in order to ensure that the analog input channel is stable. To average the measurement result, the voltage and the current are saved in an array, then the slope of U_i and I_o is calculated using the *Linear Fit* function from LabVIEW. It yields the slope and error, where the inverse of the slope is the measured ohmic resistance. The slope itself is calculated based on [119]

$$Slope = \frac{\sum(x_i - \bar{x})(y_i - \bar{y})}{\sum(x_i - \bar{x})^2}. \tag{4.3}$$

The reference resistor value is determined by the resistance of the DUT. The sensor coils of the measured device have a resistance in the range of 1 to 100 ohm. Therefore, to operate the measurement with 0.01 A current limit would set the maximum input voltage from 10 mV to 1 V. So the reference resistor should be set to 10 ohm to generate 100 mV output. The DC resistance is calculated using Ohm's law

$$R = \frac{U_i}{I_o} \tag{4.4}$$

where R is the ohmic resistance, U_i is the DC voltage, and I_o is the DC current.

DC Resistance Measurement Calibration

The ohmic resistance calibration is carried out at a temperature of 22°C using several fixed resistances with a tolerance of 1%, they are short (0 Ω), 1 Ω, 10 Ω, and 50 Ω. These values were taken because the impedance of fluxgate's coils we measure is in this range. From the measurement we obtain a linear equation for each resistance, the slope inverse represents the measured resistance value. The curves for resistance measurements are shown in figure 4.1.

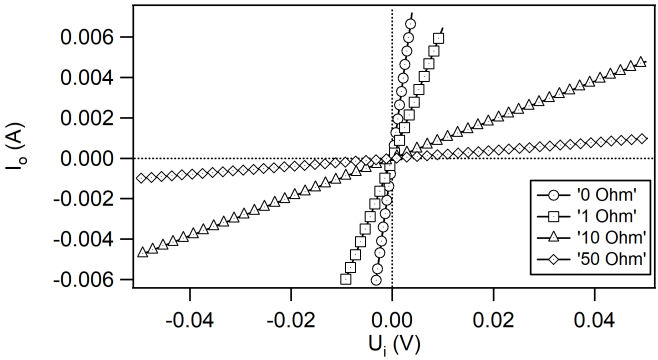

Figure 4.1: I(U) curve of ohmic resistance measurement.

The measured resistance values obtained from the slopes inverse are 0.54 Ω, 1.54 Ω, 10.46 Ω, and 50.67 Ω for 0 Ω, 1 Ω, 10 Ω, and 50 Ω, respectively. The measurement uncertainty of slopes for 95% confidence interval are 0.0003 Ω, 0.0005 Ω, 0.0008 Ω, and 0.0114 Ω. The uncertainty values are small enough and have the tendency to increase by the increase of the resistance values. The calibration curve is obtained by fitting the measured and reference data using linear equation with offset as formulated in (4.1). The obtained c_1 and c_2 values are 1.0031 and 0.504 with the uncertainty of 0.00694 and 0.177, respectively. The uncertainty of c_2 is larger than c_1. This is caused by the system offset error, which is larger than the slope error. The linear calibration curve is shown in equation (4.5)

$$Z_o = 1.0031 \cdot Z_i + 0.504. \tag{4.5}$$

The fitting curve of data is shown in figure 4.2. To obtain the calibrated resistance value from the measurement, equation (4.5) must be inverted to be

$$Z_i = \frac{Z_o - 0.504}{1.0031}. \tag{4.6}$$

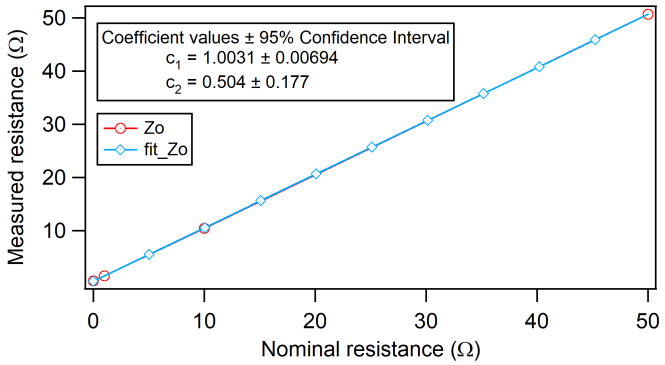

Figure 4.2: Linear calibration curve of DC resistance and its fitting curve.

DC Resistance Measurement Validation

By applying equation (4.6) to the resistance measurement values, we obtain the calibrated results and the residuals. The residuals are shown in figure 4.3. The uncertainty of the slopes inverse together with the uncer-

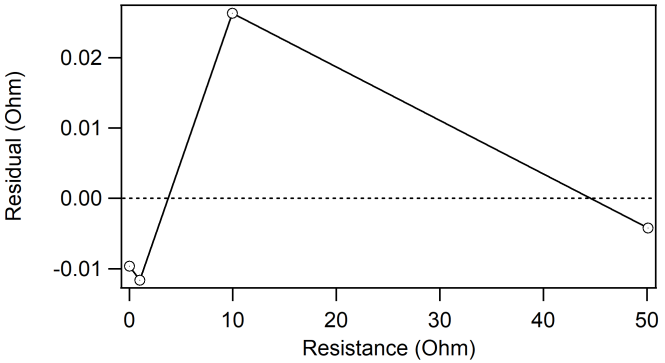

Figure 4.3: Residual of measured and calibrated resistance.

tainty of analog input form the uncertainty of the resistance measurement, that is

$$u^2(Z_o) = u^2(Z_{slope}) + u^2(AI). \tag{4.7}$$

where $u(Z_{slope})$ is the slope inverse uncertainty and $u(AI)$ is the analog input uncertainty derived form the card's analog input uncertainty [120] with the maximum value of 0.0062 Ω. The resistances tolerance enters the

combined uncertainty through the calibration equation, since the equation is determined using the sample resistances. Therefore, the combined uncertainty is the combination of the slopes inverse, analog input, resistances tolerance, c_1, and c_2 uncertainties according to the rules in [121, 122], that is

$$u_c^2(Z_i) = (u^2(Z_o) + u^2(R_{tol}) + Z_o^2 \cdot u^2(c_1) + u^2(c_2) + 2Z_o u(c_1)u(c_2)r(c_1, c_2)), \tag{4.8}$$

where $u_c(Z_i)$ is the combined uncertainty, $u(Z_o)$ is the resistance measurement uncertainty as shown in (4.7), $u(R_{tol})$ is the reference resistances uncertainty, $u(c_1)$ is the uncertainty of c_1, $u(c_2)$ is the uncertainty of c_2, and $r(c_1, c_2)$ is the correlation between c_1 and c_2. The contribution of the tolerance of the resistances dominates the combined uncertainty. While the contributions of the other sources are much smaller than it. By inserting the value and uncertainty of measurement result to equation (4.8) and taking the maximum value gives the calibration result uncertainty of 0.59 Ω at 50 Ω. From the uncertainty values, it can be seen that the combination uncertainty is dominated by the uncertainty of the reference resistance used, which is 1%, while the correlation uncertainty contribution is very small compared to the combined uncertainty.
To validate the calibration, the results obtained from equation (4.6) are compared to the resistance values from the measurements using a multimeter Hewlett Packard (HP) 34401A. The measurement results of the reference are 0.0295 Ω, 1.0305 Ω, 9.9692 Ω, and 50.0931 Ω for 0 Ω, 1 Ω, 10 Ω, and 50 Ω, respectively. The uncertainty of the multimeter is (0.01% of reading + 0.004% of range) for one year at 23°C ± 5°C [123]. It is comparable to the uncertainty of the slopes inverse measurement, but much smaller than the uncertainty of the calibration. The comparisons yield some close values between the calibrated and the results from the multimeter, and yet the differences lay within the range of the calibration uncertainty. The systematic error by temperature changes has not been determined so far, because the measurements are accomplished in a stabilized temperature environment.

DC Resistance Measurement Results

The results of DC resistance measurements of the fluxgate coils are summarized in table 4.2. This measurement only employs FG-03 for convenience. There are some differences between the results from calculation and the results from measurements, which are carried out using the FG Analyzer and multimeter HP 34401A, respectively. The largest difference is seen on the compensation coil with the value of 0.52 Ω between the resistance from the calculation and the measurement with the multimeter. The smallest difference is seen for the primary coil 1 with the value of 0.06 Ω. It is also seen that the differences between the FG analyzer and HP 34401A are still within the range of the combined uncertainties of the FG analyzer (u_{FG}). u_{HP} is the combined uncertainty of HP 34401A multimeter. Both u_{FG} and u_{HP} include the reference resistance uncertainty in the calculation.

Table 4.2: Fluxgate coil resistances.

Coil	Calculation (Ω)	FG Analyzer (Ω)	u_{FG} (%)	HP 34401A (Ω)	u_{HP}[123] (%)
Pri. 1	2.83	2.87	1.2	2.89	1.02
Pri. 2	2.83	2.90	1.2	2.89	1.02
Sec.	48.64	48.93	1.2	48.86	1.02
Comp.	19.79	19.28	1.2	19.27	1.02

4.2.3 Impedance Measurement

Impedance Measurement

The impedance is measured by exciting an AC signal into the coil and the output response is measured. An absolute impedance is simply calculated by using obtained voltage and current signal amplitude

$$|Z| = \frac{|\hat{u}_i|}{|\hat{i}_o|}. \tag{4.9}$$

The impedance is measured with increasing frequency, which is ranging from 10 Hz to 10 kHz.

Impedance Measurement Calibration

The impedance measurement calibration utilizes the general equation of calibration (4.1). The calibration is carried out by using several samples of fixed reference resistances. The calibration incorporates the measurement results of reference resistance from an impedance analyzer Agilent 4294A.

Impedance Measurement Validation

The validation of calibrated impedance measurement is done by comparing the measurement result with the measurement result from the impedance analyzer Agilent 4294A.

Impedance Measurement Results

The impedance measurement results of fluxgate primary coils are shown in figure 4.4. These results are obtained from the primary coils of fluxgate sensors FG-02 and FG-03. It is shown that the impedance is increasing with increasing frequency. It's obviously true, since the coil reactance is dominated by the inductance effect in this frequency range.

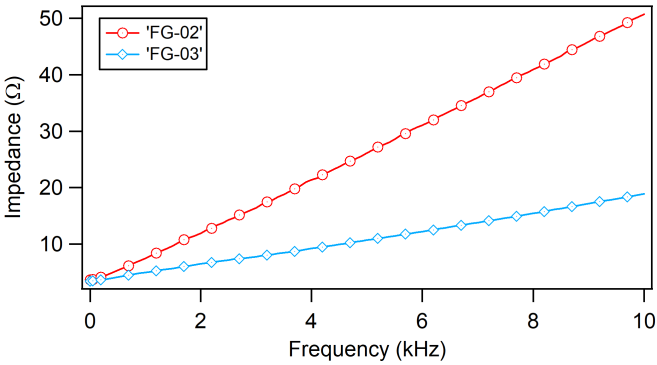

Figure 4.4: Impedance measurement results.

4.2.4 Inductance Measurement

Inductance Measurement

The inductance is measured with the same procedure as for the impedance, but the phase difference is also measured since it is included in the inductance calculation as shown in equation (4.13). The measured parameters are processed using the *Frequency Response Function* from LabVIEW. This function directly measures the absolute magnitude ratio and phase difference between $\hat{u}_i$ and $\hat{i}_o$. All the inductance measurements with the fluxgate sensor are performed in a magnetic shielding with a shielding factor of 200. Thus, the earth magnetic field should have been reduced to about 250 nT and it does not affect the inductance measurements beyond the measurement uncertainty. Impedance is calculated based on the complex impedance

$$Z = \frac{|\hat{u}_i| e^{j\omega t}}{|\hat{i}_o| e^{j(\omega t - \varphi)}} \tag{4.10}$$

where Z is the impedance, $\hat{u}_i$ is the voltage signal, $\hat{i}_o$ is the current signal, ω is the angular frequency, t is time, and φ is the phase difference between the voltage and current. From the impedance result, we can obtain the inductance, which is the imaginary part of impedance

$$Z = R + j(\omega L) \tag{4.11}$$

$$Z = |Z| e^{j\varphi} = |Z|(\cos\varphi + j \sin\varphi) \tag{4.12}$$

$$L = \frac{|Z| \sin\varphi}{2\pi f} \tag{4.13}$$

where L is the inductance, R is the resistance, $|Z|$ is the absolute impedance, and f is the frequency. Thus, in this design the absolute magnitude ratio

and the phase difference between voltage and current are measured to obtain the inductance of coil. With these parameters the inductance can be determined through equation (4.13).

Inductance Measurement Calibration

The same reference resistances are used to determine the inductance from linear expression. The use of resistance for inductance calibration is intended for avoiding the imaginary part of the impedance, thus the impedance is not changed by the increase of frequency. Equation (4.1) is used again to create the calibration equation. Different to the DC resistance calibration, the c_1 and c_2 constants are determined using a pair of one reference impedance together with a zero impedance (Z_i = 0 Ω) [117]. But, in order to increase the accuracy, three pairs of the reference and zero impedance are used. They are 1 Ω and 0 Ω, 10 Ω and 0 Ω, and 50 Ω and 0 Ω. The impedance references have both real and small imaginary values although the resistances are used. Therefore, both values are included in the calculation. For each pair, c_2 is simply obtained by inserting zero impedance to the equation as shown in equation (4.14):

$$Z_o(0) = c_1 \cdot Z_i(0) + c_2 \tag{4.14}$$

$$Z_o(0) = c_2 \tag{4.15}$$

c_1 can be determined by inserting the obtained c_2 and the reference impedance to the equation. For 1 Ω reference impedance, it yields

$$Z_o(1) = c_{1,1} \cdot Z_i(1) + Z_o(0). \tag{4.16}$$

$$c_{1,1} = \frac{Z_o(1) - Z_o(0)}{Z_i(1)}. \tag{4.17}$$

$c_{1,1}$ is the obtained c_1 for the first pair. The same procedure is performed for the other two pairs resulting in $c_{1,2}$ and $c_{1,3}$. The three obtained c_1 values from the pairs are then averaged, while the c_2 value remains constant and gives the systematic offset. Due to the frequency-dependence of gain and phase shift, the calibration is performed at each applied frequency. All parameters in the calculation are in complex form. From the calculations, we obtain the inverted calibrating equations for three sample frequencies, they are

$$\begin{aligned} Z_i &= (0.9817 + j0.0020) \cdot (Z_o - (0.5159 + j0.0001))\ (100Hz), \\ Z_i &= (0.9821 + j0.0230) \cdot (Z_o - (0.5161 + j0.0025))\ (1kHz), \\ Z_i &= (0.9585 + j0.2280) \cdot (Z_o - (0.5328 + j0.0200))\ (10kHz). \end{aligned} \tag{4.18}$$

It is seen from equation (4.18) that the real and imaginary part change by the change of frequency. The impedance calibration curves are shown in figure 4.5. All curves look similar although they have different equation. The differences of the equations are very small, so it cannot be observed visually.

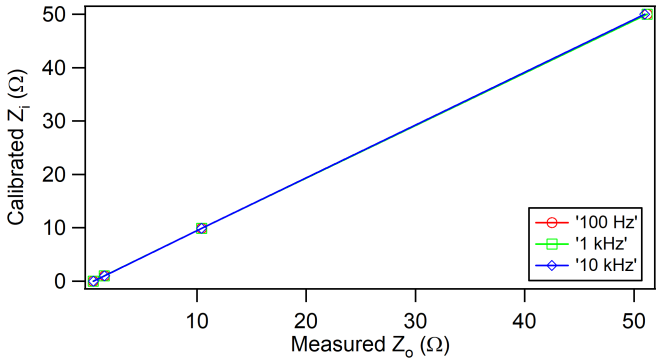

Figure 4.5: Linear calibration curves of impedance for different frequencies.

By fitting the impedance calibration curves, the uncertainties are obtained and combined according to [121] as shown in (4.19)

$$\begin{aligned} u_c^2(Z_i) &= (u^2(AI) + u^2(R_{tol}) + Z_o^2 \cdot 0.0083^2 + 0.216^2 \\ &\quad + 2Z_o \cdot 0.0083 \cdot 0.216 \cdot r(c_1, c_2))\ (100Hz), \\ u_c^2(Z_i) &= (u^2(AI) + u^2(R_{tol}) + Z_o^2 \cdot 0.0082^2 + 0.213^2 \\ &\quad + 2Z_o \cdot 0.0082 \cdot 0.213 \cdot r(c_1, c_2))\ (1kHz), \\ u_c^2(Z_i) &= (u^2(AI) + u^2(R_{tol}) + Z_o^2 \cdot 0.0069^2 + 0.180^2 \\ &\quad + 2Z_o \cdot 0.0069 \cdot 0.180 \cdot r(c_1, c_2))\ (10kHz). \end{aligned} \tag{4.19}$$

$u_c(Z_i)$ is the combined uncertainty, the resistance tolerance $u(R_{tol})$ is included as the calibrator of the equation, the third and the fourth terms on the right side are the c_1 and c_2 uncertainties, respectively, and the $r(c_1, c_2)$ is the correlation between c_1 and c_2.

Inductance Measurement Validation

The inductance measurements for the fixed inductances with the values of 0.1 mH, 1 mH, and 10 mH are performed at 100 Hz, 1 kHz, and 10 kHz to validate the calibration results. Table 4.3 shows the measurement results and its comparisons to the measurement results from the impedance analyzer Agilent 4294A for those check frequencies. The relative uncertainty of the used impedance analyzer is 0.08% [124]. The uncertainties of the fixed inductances measurement are shown in figure 4.6. It is clearly shown that the obtained maximum measurement uncertainties are not more than the FG Analyzer combined uncertainty (u_{FGL}) of 2%. u_{AGL} is the combined uncertainty of Agilent 4294A impedance analyzer. Both u_{FGL} and u_{AGL} include the reference resistance uncertainty in the calculation.

Table 4.3: Fixed inductance measurement at check frequencies.

L	Measured Inductance (mH)							
	FG Analyzer				Agilent 4294A			
(mH)	100 Hz	1 kHz	10 kHz	u_{FGL}	100 Hz	1 kHz	10 kHz	u_{AGL} [124]
0.1	0.099	0.098	0.097	2%	0.099	0.098	0.096	1.08%
1	0.98	0.978	0.97	2%	0.983	0.977	0.972	1.08%
10	9.914	9.897	9.902	2%	9.91	9.91	9.91	1.08%

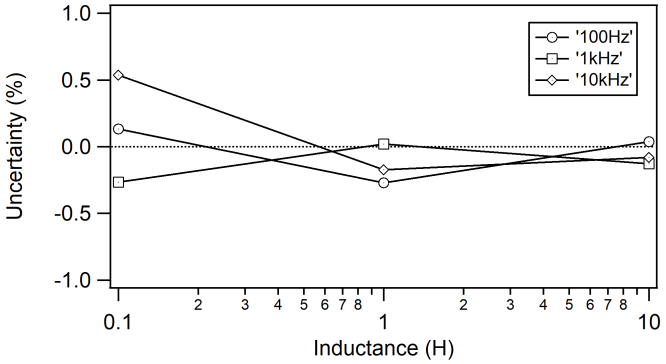

Figure 4.6: Inductance measurement error using FG Analyzer.

Inductance Measurement Results

The fluxgate coil inductances from the calculations give different values for each coil. Based on the calculation with a relative permeability (μ_r) of 10^5 [99], the inductances of primaries, secondary, and compensation coils of FG-03 are 5.437 mH, 135.5 mH and 8.078 mH, respectively. The results from the measurements give different values, where the inductances of primaries, secondary, and compensation coils at the frequencies above 6 kHz are about 0.350 mH, 0.98 mH, and 0.625 mH, respectively. This happened because the core initial permeability is much lower than the permeability provided in the manufacturer's datasheet. This can be caused by the mechanical treatment during fluxgate sensor manufacturing [125]. In addition, the apparent permeability is lower than the initial permeability due to the geometry of the fluxgate sensor, by the demagnetization factor [49]. Based on the permeability measurement with 10 kHz and 3.6 V excitation on primary coils with the set up from [126], the apparent permeability of the core is about $\mu_{r,c} = 5888$. It is theoretically comparable to the permeability derived from the inductance of the primary coils, which is $\mu_{r,p} = 5809$.

The measurement results of the fluxgate coil inductances are shown in figure 4.7. In this figure, the inductance measurement of all coils in the fluxgate sensor is presented using the FG Analyzer and the impedance analyzer Agilent 4294A. The measurements are carried out with different excitation magnitudes for different coil. The primary coils are excited with 0.2 mA current, and the secondary and compensation coils are excited with 5 mV voltage. The last two coils are excited with the voltage source because of its high impedance.

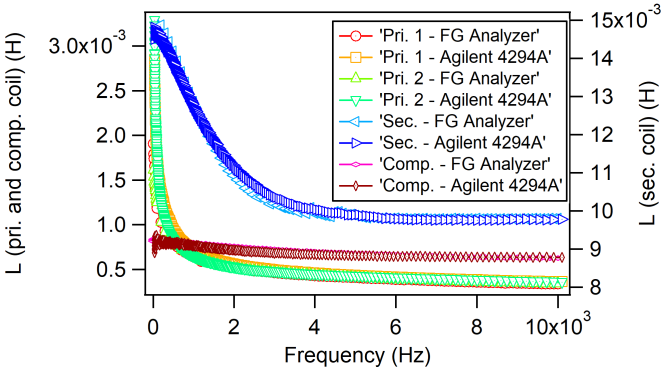

Figure 4.7: Inductance of FG sensor coils.

It is seen here that the resulting curves of the primaries, secondary, and compensation coil are coincident for the measurements using the FG Analyzer and Agilent 4294A. This proves that the FG Analyzer gives the correct measurement results.
Besides that, each curve also shows a decreasing trend. The decrease rate is different for each coil. The largest decrease is observed for the primary coils, where the smallest decrease is observed for the compensation coil. It is caused by the current applied to the coils. For low frequency and above a certain current, the inductance is a function of applied current, and decreases rapidly as the frequency increases. The inductance is independent of the applied current for the excitation, which is below this certain current. For frequency around 10 kHz, the inductance is less dependent on the applied current [127]. This frequency dependence is mainly caused by the eddy current, which requires more current to get the same magnetic flux density. This is also observed by [128]. The changes of the inductance are mainly caused by the changes of the core permeability. The changes of permeability of soft magnetic materials including both real and imaginary due to frequency and temperature are analyzed by [129]. It is observed that the real permeability drops with the increase of frequency, while the imaginary permeability increases to a peak at a characteristic frequency. It is caused by the eddy current shielding, which reduces the internal field compared to the surface field and increases the phase lag between the internal and excitation fields.

Figure 4.8 shows the curves of apparent inductance of the primary coil 1 coil for several applied currents measured with FG Analyzer. The applied currents are 0.05 mA, 0.1 mA, 0.15 mA, 0.2 mA, 0.25 mA, and 0.3 mA. The differences of the measured inductance for each applied current are clearly seen at low frequency. The measured inductance in this range is current-dependent, where the inductance is proportional to the applied current. The magnitude of the measured inductance decreases as the current decreases, and also decreases as the frequency increases. The smallest tested current is 0.05 mA. It shows a relatively constant inductance over the applied frequency range. Below this current, the inductance is independent of the applied current. It indicates that the maximum current allowed for correct inductance measurement in this frequency range requires lower excitation currents than the Agilent 4294A can provide. Using the FG Analyzer to analyze a fluxgate sensor gives more accurate results than using Agilent 4294A, which has the minimum current of 0.2 mA [130].

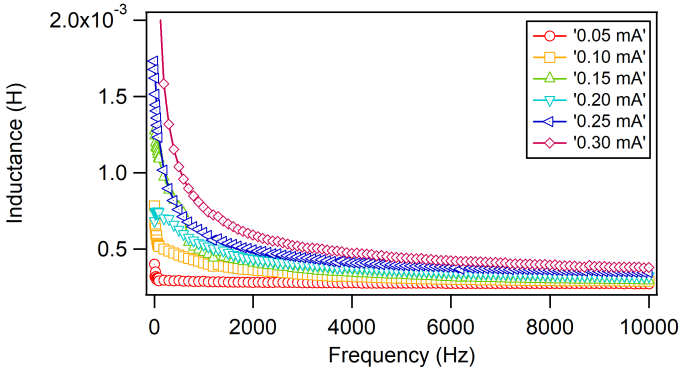

Figure 4.8: Apparent inductance of primary coil with varied current.

4.3 Sideband Sensitivity

Many studies have been accomplished to improve the fluxgate sensitivity and lower the noise. The fundamental limit of fluxgate sensitivity has been studied by [85]. They predicted the noise from the core is less than 100 fT/$\sqrt{Hz}$ for a fluxgate with the volume of 2×10^{-8} m^3. The influence of geometry on the sensitivity and noise of fluxgate has also been studied by [19, 131]. They varied the geometry of a race-track fluxgate and obtained the geometry influence on the sideband sensitivity on the sensor alone. This is conceptually an important point, since this allows to optimize the sensor independently from its electronics. There have been many efforts with different methods to increase the sensitivity and suppress the noise, but there is no comprehensive formulation to predict

the fluxgate sensitivity and its input noise yet. In this study, the approach of fluxgate sensitivity based on the current and time dependence of the coils inductance is implemented. The model can later be used to improve the sensitivity.

4.3.1 Fluxgate Sensor Properties

Fluxgate Configuration

As mentioned before, the fluxgate sensor used in this experiment is of racetrack type sensor. It consists of three coils, they are the primary coil 1, primary coil 2, and secondary coil. The primary coils are wound on each side around a racetrack shaped core and these primary coils are enclosed by one secondary coil. The Vitrovac 6025Z [98] from Vacuumschmelze is used for the core with thickness of 25 μm, width of 1 mm, 3 layers, relative permeability (μ_r) of 10^5 [99] and saturation induction of 0.58 T. The geometrical configuration of the fluxgate sensor is shown in figure 4.9.

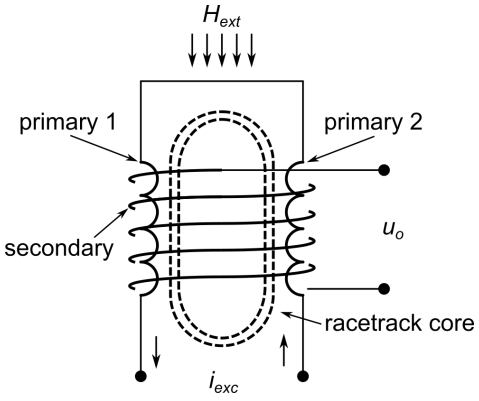

Figure 4.9: Fluxgate sensor geometric configuration.

The coils of the fluxgate are made of copper wire and wound as the solenoid-shaped winding, they are characterized by the physical properties such as resistance, inductance, and capacitance. Each coil in the fluxgate can be described by an equivalent circuit, which includes resistance, inductance, and capacitance as depicted in figure 4.10.

Fluxgate Impedance for Sensitivity Measurement

The series DC resistance of the coil affects the current flowing in the coil. Thus, it should be taken into account in order to calculate the current to determine the magnetic field produced by the coil. The series DC resistance of the coil can be calculated from the known physical parameters i.e wire resistivity, length, and cross-sectional area using equation (3.5).

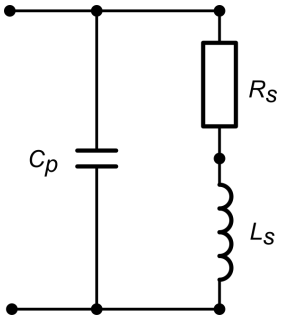

Figure 4.10: Fluxgate coil equivalent circuit.

The inductance of the coils can be calculated using the solenoid inductor equation (3.20) [102].
The parallel capacitances (C_p) of the primary coils are not considered and included in the calculation. Since its winding generally consists of only one layer, the capacitance value is very small and it does not affect the impedance in the frequency range used. Typical self resonance frequencies lie well above the modulation frequency of the fluxgate. This is more crucial for the secondary coil, where the winding contains usually more than one layer, and thus the capacitance has to be considered.

4.3.2 Fluxgate Output Voltage

Second Harmonic Output

The fluxgate sensor operates based on the time dependent change of core permeability, which is periodically saturated by the excitation current. Because the permeability changes with the applied magnetic field, so does the inductance. Therefore, the inductance of the coils with a large length to diameter ratio can be written as

$$L(i) = \frac{N^2 A}{l} \times \mu(i). \tag{4.20}$$

$L(i)$ is the current-dependent inductance, $\mu(i)$ is the current-dependent permeability, i is the excitation current, and l is the effective length of the core, which is equal to $2l_c + \pi d_c$ for racetrack fluxgate [19]. In principle, the fluxgate core is deeply saturated to ensure that it is free from remnant magnetization and thus leaves out the memory effects [131]. The core as magnetic material has a relationship between magnetic field and flux density, which is described by the magnetization curve. Here, the arctangent function is used to model the magnetization curve of the core:

$$B = \frac{2aB_s}{\pi} arctan[b(H \pm H_{ext}) + c]. \tag{4.21}$$

B is the flux density, B_s is the core saturation flux density, H is the excitation field, H_{ext} is the low frequency external field, and a, b, and c are the adjustment constants for saturation induction, magnetic field, and coercivity, respectively. The slope of magnetization curve reflects the permeability of material. It has a maximum value at zero field and a minimum value at saturation. Therefore, the current-dependent permeability of the core is

$$\mu(i) = \frac{dB}{dH} = \frac{2abB_s/\pi}{1 + [b(H(i) \pm H_{ext}) + c]^2}, \tag{4.22}$$

the sign of H_{ext} depends on its direction with respect to the coils. It is positive when it is in the same direction and vice versa. Then the inductance of the coil can be expressed as

$$L(i) = \frac{N^2 A}{l} \frac{2abB_s/\pi}{1 + [b(H(i) \pm H_{ext}) + c]^2}. \tag{4.23}$$

The output voltage at the secondary coil is obtained by applying Faraday's law. The output voltage at the secondary coil is then defined as

$$u_o = -N_s \frac{d\Phi}{dt}, \tag{4.24}$$

where u_o is the output voltage, N_s is the secondary coil turns number, and Φ is the magnetic flux. The modeled output voltage refers to the unloaded condition since it is just using the second harmonic sideband sensitivity of the fluxgate sensor alone without electronics. Because the circuit is unloaded, the current at the secondary coil is assumed to be zero. The one and only energy is coming from the mutual inductance of both primary coils and the secondary coil. Therefore, the unloaded output voltage is derived from the difference of mutual inductance between both primaries and secondary coils. The mutual inductance of the coils is current-dependent, so equation (4.24) becomes

$$u_o = -M(i) \frac{di}{dt}. \tag{4.25}$$

M is the net difference between M_1 and M_2:

$$M(i) = M_1(i) - M_2(i) \tag{4.26}$$

$M_1(i)$ is the mutual inductance between primary coil 1 and secondary coil, and $M_2(i)$ is the mutual inductance between primary coil 2 and secondary coil. With the assumption of coupling factors k_1 and k_2 of the mutual inductance to be $k_1 = 1$ and $k_2 = 1$, then M_1 and M_2 can be written as [132]

$$M_1(i) = k_1 \sqrt{L_{p1}(i) L_s(i)} = \sqrt{L_{p1}(i) L_s(i)}, \tag{4.27}$$

and

$$M_2(i) = k_2\sqrt{L_{p2}(i)L_{sec}(i)} = \sqrt{L_{p2}(i)L_{sec}(i)}, \tag{4.28}$$

where $L_{p1}(i)$ is the primary coil 1 current-dependent inductance, $L_{p2}(i)$ is the primary coil 2 current-dependent inductance, and $L_{sec}(i_s)$ is the secondary inductance. If the excitation field on primary coil 1 has the same direction as the external field then the sign of H_{ext} is positive, and likewise for primary coil 2, which its excitation field is in the opposite direction with the external field causing a negative sign of H_{ext}. The sign of H_{ext} of $L_s(i_s)$ depends on with which primary coil it is multiplied:

$$L_{p1}(i) = \frac{N_{p1}^2 A}{l}\frac{2abB_s/\pi}{1+[b(H(i)+H_{ext})+c]^2}, \tag{4.29}$$

$$L_{p2}(i) = \frac{N_{p2}^2 A}{l}\frac{2abB_s/\pi}{1+[b(H(i)-H_{ext})+c]^2}, \tag{4.30}$$

$$L_{sec}(i) = \frac{N_s^2 A}{l}\frac{2abB_s/\pi}{1+[b(H(i)\pm H_{ext})+c]^2}. \tag{4.31}$$

The current i in primary coil 1 and primary coil 2 is the same because the coils are connected in series and the coils parallel capacitance is very small and is neglected. The change of L_{sec} with time depends as well on the core permeability change caused by the primary coil current $i(t)$. M_1 and M_2 can be written as

$$M_1(i) = \frac{N_s}{N_{p1}}L_{p1} \tag{4.32}$$

and

$$M_2(i) = \frac{N_s}{N_{p2}}L_{p2}. \tag{4.33}$$

N_{p1} and N_{p2} are the primary coil 1 and primary coil 2 turn numbers, and N_s is the secondary coil turns number. If $N_{p1} = N_{p2} = N_p$, M is obtained by using (4.26), (4.32), and (4.33).

$$M = \frac{N_s}{N_p}\left(L_{p1}(i) - L_{p2}(i)\right). \tag{4.34}$$

By applying (4.29) and (4.30) to (4.34), one obtains

$$M = \frac{N_s}{N_p}\frac{N_p^2 A}{l}\times \left(\frac{2abB_s/\pi}{1+[b(H(i)+H_{ext})+c]^2} - \frac{2abB_s/\pi}{1+[b(H(i)-H_{ext})+c]^2}\right). \tag{4.35}$$

Since H_{ext} is much smaller than $H(i)$, H_{ext} at the denominator can be neglected. Thus,

$$M = -2H_{ext}\frac{N_s}{N_p}\frac{N_p^2 A}{l}\frac{(4ab^2 B_s/\pi)(bH+c)}{[1+(bH+c)^2]^2}, \tag{4.36}$$

$$= -2H_{ext}\frac{N_s}{N_p}\frac{dL_p}{dH}. \tag{4.37}$$

By inserting (4.37) in (4.25), the fluxgate output voltage is obtained

$$u_o(t) = 2H_{ext}\frac{N_s l}{N_p^2}\frac{di}{dt}\frac{dL_p(t)}{di}. \tag{4.38}$$

This expression is similar to the general fluxgate output voltage as shown in [26]:

$$v_o(t) = NA\mu_0 H_{ext}\frac{d\mu_r(t)}{dt}. \tag{4.39}$$

The difference is just the use of inductance instead of permeability parameter. The output voltage $u_o(t)$ is a combination signal of even harmonics. If one even harmonic output voltage is desired, the amplitude of harmonic can be obtained using a Fourier series:

$$u_o(t) = u_{o_0} + \sum_{n=1}^{\infty}(u_{o2nf_0,1}\cos 2n\omega_0 t + u_{o2nf_0,2}\sin 2n\omega_0 t) \tag{4.40}$$

Because the output is an odd function signal, only the last term of (4.40) will remain. Then, the second harmonic output can be calculated through

$$u_{o2f_0} = \frac{4}{T_{exc}}\int_0^{T_{exc}/2} u_o(t)\cdot\sin 2\omega_0 t\ dt. \tag{4.41}$$

Then, the second harmonic sensitivity of (4.41) is

$$S_{sb} = \frac{u_{o2f_0}}{\mu_0 H_{ext}} \tag{4.42}$$

where μ_0 is the vacuum permeability.

Apparent Inductance

The apparent inductance in (4.38) is a current-dependent inductance. Since the magnetic field saturates the core when the current is large, the core permeability and primary coil inductance drop to a minimum value. A function of current-dependent inductance is needed to describe $u_o(t)$. Therefore, the inductance must be measured in order to calculate the output voltage using equation (4.38). The inductance measurement must

be carried out in the excitation current variations until saturation. Providing an offset current on the current signal of inductance measurement can bring the core into saturation. The offset current is varied from zero to the value where the core saturates. The offset current increment value is 0.1 mA and the current signal is set low to avoid direct saturation and its value is also 0.1 mA [133]. The inductance value at zero offset current might be much lower than the result from calculation with the provided parameter from core datasheet. This could happen because the measured inductance is the apparent inductance, which already incorporates the influencing factors such as the core demagnetization and geometry. The measurement is performed in static condition. In spite of that, the result would not be much different from the measurement at the excitation frequency because it is still in low frequency regime [134].
From the current-dependent inductance measurement, the function of current-dependent inductance can be obtained. With the substitution of this function to equation (4.38), the output voltage of the secondary coil can be determined. The inductance of coil as a function of the magnetic field or excitation current is shown in equation (4.23) and it is similar to the core permeability behavior (4.22). Therefore, a similar model is needed to express the inductance function. By adopting equation (4.23), the current-dependent inductance function can be approximated with the assumption of $H_{ext} = 0$ and $c = 0$. If

$$\frac{N^2 A}{l} \frac{2abB_s}{\pi} = p, \tag{4.43}$$

and

$$\frac{bN}{l} = q. \tag{4.44}$$

Then,

$$L(i) = \frac{p}{1 + (qi)^2}, \tag{4.45}$$

and

$$\frac{dL(i)}{di} = -\frac{2p \cdot q^2 \cdot i}{[1 + (qi)^2]^2}, \tag{4.46}$$

p and q are constants, which can be obtained by curve fitting method of current-dependent inductance measurement result, and i is the incremented static current. Once the function is obtained, it can be substituted into (4.38). p is proportional to B_s, N^2, and q is proportional to susceptibility.

Excitation Current

The excitation coil is generally excited with a square voltage signal. The excitation circuit is shown in figure 4.11. The excitation signal drives

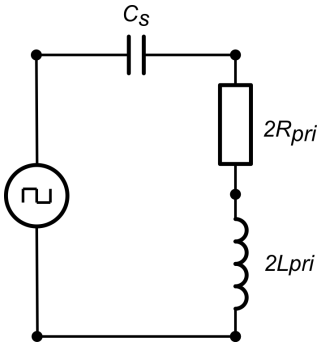

Figure 4.11: Primary coil excitation circuit.

the primary coils, which are connected in series. A capacitor is placed in series to increase the current and blocks the DC current. In order to calculate the fluxgate output signal, the excitation signal function is needed as shown in (4.38) and (4.46). This signal is analyzed by using an oscilloscope. By observing the shape of the excitation signal on the oscilloscope, it can be known that it looks like a sinusoidal signal, but has a sharp rising edge and gradual falling edge, which make a deviation from symmetry. Nevertheless, its shape can still be approximated by the sinusoidal signal pulse and resulting only a very small deviation. This approximation error would have a very small influence on the result, since the period and the maximum values are still the same. The time and amplitude values that are needed for the approximation can be obtained from the measurement from oscilloscope. Once these values are obtained, these can be inserted to (4.47). Figure 4.12 shows the excitation signal and its sinusoidal signal approximation.

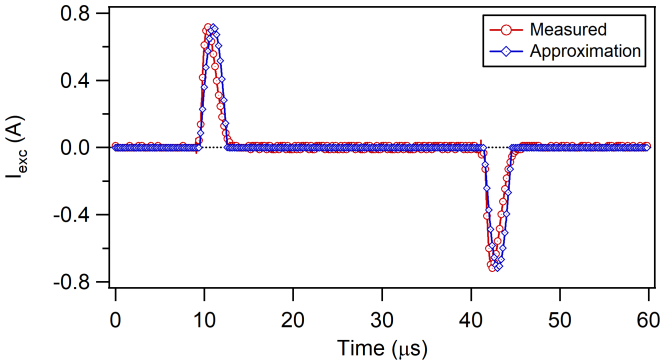

Figure 4.12: Excitation signal and its approximation.

From the approximation, the excitation signal function is obtained, that is

$$i(t) = \begin{cases} 0 & 0 \leq t < \left(\frac{T_{exc}}{4} - \frac{T_1}{2}\right) \\ i_m \sin(\omega_p t) & \left(\frac{T_{exc}}{4} - \frac{T_1}{2}\right) \leq t < \left(\frac{T_{exc}}{4} + \frac{T_1}{2}\right) \\ 0 & \left(\frac{T_{exc}}{4} + \frac{T_1}{2}\right) \leq t < \left(\frac{3T_{exc}}{4} - \frac{T_2}{2}\right) \\ -i_m \sin(\omega_p t) & \left(\frac{3T_{exc}}{4} - \frac{T_2}{2}\right) \leq t < \left(\frac{3T_{exc}}{4} + \frac{T_2}{2}\right) \\ 0 & \left(\frac{3T_{exc}}{4} + \frac{T_2}{2}\right) \leq t < T_{exc} \end{cases} \tag{4.47}$$

T_1 is the time for positive current period, T_2 is the time for negative current period, and T_{exc} is the excitation signal period. If the pulses are symmetric, T_1 and T_2 are equal and can be denoted as T_p. Because it is an odd function, the second harmonic current amplitude can be calculated by

$$i_{nf_0} = \frac{4}{T_{exc}} \int_c^d i(t) sin(n\omega_0 t) dt, \tag{4.48}$$

$$= \frac{2 \cdot i_{max}}{T_{exc}} \left[\frac{1}{\omega_1} \sin(\omega_1)t - \frac{1}{\omega_2} \sin(\omega_2)t\right]_c^d, \tag{4.49}$$

where

$$c = \frac{T_{exc}}{4} - \frac{T_p}{2} \tag{4.50}$$

$$d = \frac{T_{exc}}{4} + \frac{T_p}{2} \tag{4.51}$$

$$\omega_1 = (\omega - n\omega_0) \tag{4.52}$$

$$\omega_2 = (\omega + n\omega_0). \tag{4.53}$$

ω_p is determined by the T_{pulse} by

$$\omega_p = \frac{\pi}{T_p} \tag{4.54}$$

4.3.3 Measurement

Primary Coil Inductance

The primary coil inductances are measured using our FG Analyzer [133]. It has been calibrated and validated using the impedance analyzer Agilent 4294A. It also provides the inductance measurement with a DC offset on

its source aimed to saturate the fluxgate core. The inductance is measured using small current signal to avoid distortion and current dependent measurement result. Based on [133], the maximum allowed current for correct inductance measurement is 0.05 mA for frequencies less than 1 kHz and could be higher for higher frequency. Because the frequency in this measurement is quite high, which is about 15.625 kHz, the current source of 0.1 mA is used for the inductance measurement in order to get a large signal to noise ratio. The offset is incremented from 0 to 50 mA with increment steps of 0.1 mA. Five different fluxgate sensors are tested.

Sideband Sensitivity

The sideband sensitivity of the fluxgate is focused at the second harmonic frequency. The second harmonic sideband sensitivity is measured by obtaining the second harmonic FFT value of the unloaded fluxgate output voltage. A modulated external magnetic field is generated as a testing external field H_{ext}. This external field is set at about 4 μT and frequency $f_{H_{ext}} = 63$ Hz. By modulating the external magnetic field on the fluxgate, the second harmonic sideband of fluxgate output voltage appears beside the second harmonic of excitation frequency, that is at $2f_{exc} \pm f_{H_{ext}}$. The modulated external magnetic field is generated using a solenoid with a coil constant of 4 μT/mA. The modulation signal is derived from a spectrum analyzer Agilent 35670A and the output signal is also measured using the Agilent 35670A.
The excitation signal for the fluxgate is driven by a square voltage signal with an amplitude u_{exc}. The excitation frequency is 15.625 kHz derived from the quartz crystal and buffered by an H-bridge MOSFET transistor. The fluxgate primary coils are connected to the source with a series capacitor on an electronics board.
Figure 4.13 shows the experimental setup of sideband sensitivity measurement. The fluxgate sensor is placed in the middle of the solenoid to ensure the fluxgate sensor senses the homogeneous modulated magnetic field.

4.3.4 Inductance

The inductance measurements of the sample sensors with the parameters in table 4.4 give the results as depicted in figure 4.14, 4.15, 4.16, and 4.17. The coil inductance is the response to the applied offset current. The coil has the highest inductance at low current and then decreases towards a constant value for current depends above 10 mA. The measurement is performed in static conditions. Despite of that, the result would not be much different with the measurement at excitation frequency because it is still in the low frequency regime [134].
The inductance curves show a small flat area at the very low current smaller than 1 mA, then it decreases until it reaches the asymptotic area at the current above 10 mA. The flat area at the very low current indicates that the core is not yet in saturation, and the inductance in this area has the largest value. The decreasing curve implies the core starts to enter

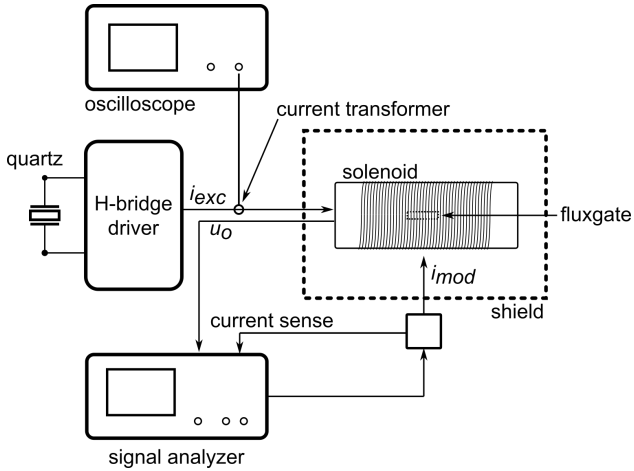

Figure 4.13: Experiment setup.

Table 4.4: Physical parameters of the used fluxgate sensor for sensitivity measurement.

Sensor	N_p (turns)	N_s (turns)	l_c (mm)	d_c (mm)	d_s (mm)	Core layers
FG-01	210	1348	30	3.0	10	3
FG-02	208	621	30	3.0	10	3
FG-03	208	929	30	3.0	10	3
FG-04	212	1027	30	3.0	10	3
FG-06	363	1716	60	3.0	10	2
FG-07	380	2741	50	3.0	10	2

the saturation regime, where it locates at the corner of magnetization curve. The asymptotic region at the current larger than 10 mA is where the core experiences saturation and the inductance value does not change much after this point. So the inductance has the smallest value in this range.

The curves in figures 4.14, 4.15, 4.16, and 4.17 are fitted using equation (4.45). The p and q from fitting process are used to approximate the curve. The p is associated with the maximum inductance, while the q is associated with the inductance decrease slope. From several sensors under test, we obtained some different curves and from the fitting some p and q values are obtained. The largest maximum inductance is obtained for FG-02, while the largest slope is obtained for FG-07. It is obvious because FG-02 has more core layers and FG-07 has more coil turns.

From the figures, it is seen that the fitting of FG-02 and FG-03 give rather

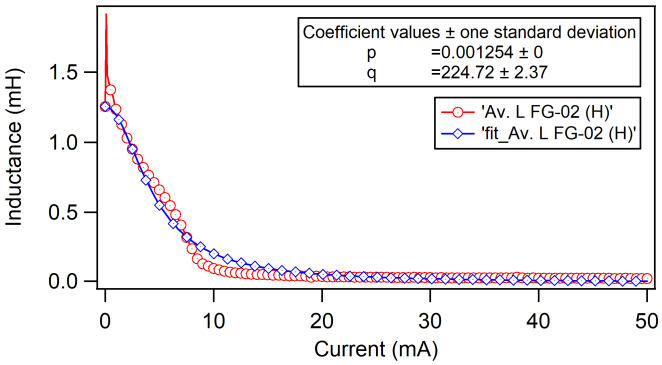

Figure 4.14: Fluxgate inductance fitting for FG-02.

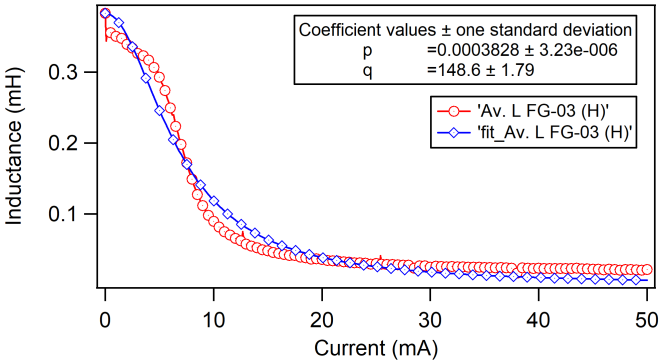

Figure 4.15: Fluxgate inductance fitting for FG-03.

larger deviations if compared to FG-06 and FG-07. The deviations remain the same if the adopted equation (4.23) is in the original form. The cause of these deviations is the inductance measurement error when measuring low impedance coil at low offset current. The obtained p and q value from fitting are then used to calculate the sensitivity of the fluxgate sensor. The measurement results are listed in table 4.5.

4.3.5 Output Voltage Signal

The output voltage signal follows equation (4.38). This equation differs from the fluxgate output equations in literature, which utilize the permeability parameter. In equation (4.38), it utilizes the inductance parameter instead of permeability. The utilization of inductance provides simplicity

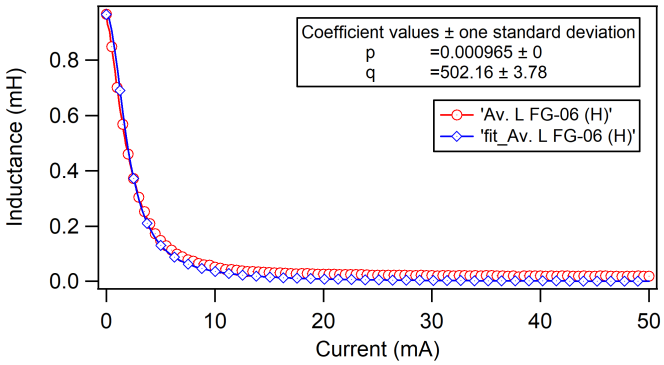

Figure 4.16: Fluxgate inductance fitting for FG-06.

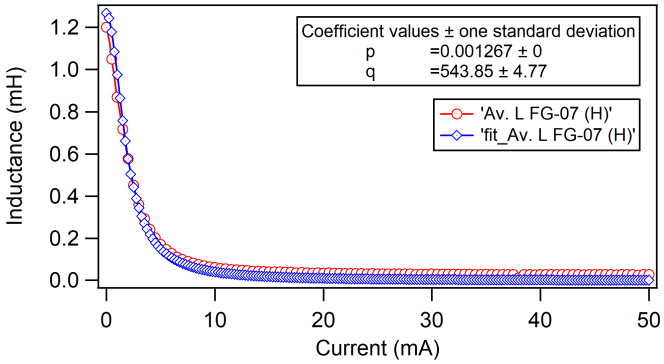

Figure 4.17: Fluxgate inductance fitting for FG-07.

in the measurement, which only needs one coil instead of two coils as in the permeability measurement. Moreover, the application of inductance measurement eases the determination of fluxgate output signal because the inductance as a function of current can be obtained and can then be transformed to time domain.

The calculated output signal is obtained using the data of the excitation current and inductance measurement. The excitation current measurement provides the current peak and pulse width, while the inductance measurement provides the p and q values. The other parameters are obtained from the fluxgate physical parameters. Figure 4.18 shows the signal of the simulated excitation current and calculated fluxgate output signal. It is seen that the output signal has a minimum and maximum value at the onset and offset of the excitation current. This can easily

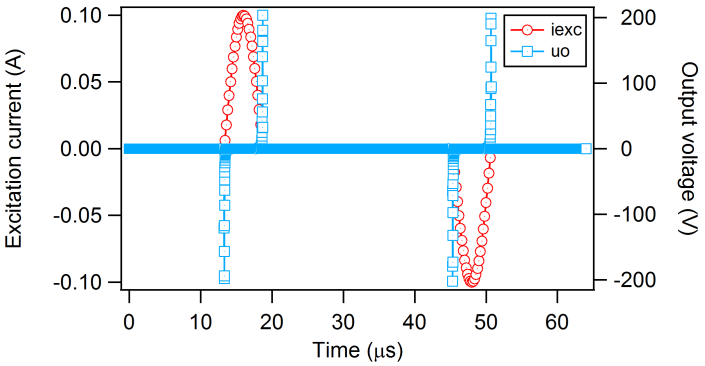

Figure 4.18: Calculated fluxgate output voltage signal.

be understood since the maximum rate of the inductance change occurs at this point. The signal between the maximum and minimum points is equal to zero since there is only a small change of inductance on the saturation. The output signal also shows that its frequency is twice of the excitation frequency. This explains the output signal is an even signal and has the maximum value at the second harmonic of excitation frequency. Figure 4.19 shows the excitation current and fluxgate output signal from the oscilloscope. This signals can be compared to the signal obtained from the calculation. It is seen from figure 4.19 that the signals have the same

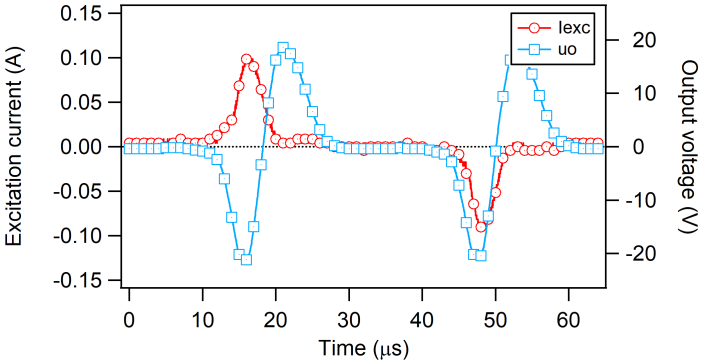

Figure 4.19: Measured fluxgate output voltage signal.

pattern and frequency with the signals from the calculation (figure 4.18). The only difference is on the width of minimum and maximum cycles of the output signal. The width from the measurement is wider than from the calculation. This is probably due to the self-resonance phenomenon in

the secondary coil, that creates a resonance frequency close to the pulse frequency.

4.3.6 Sideband Sensitivity

The example of sideband output voltage of the second harmonic near $2f_{exc}$ is shown in figure 4.20. The figure shows two peaks beside the second

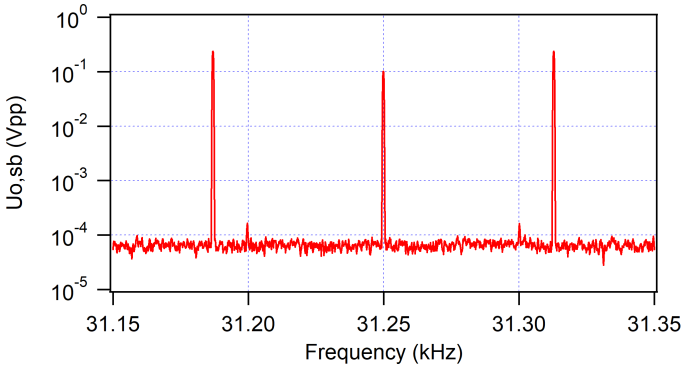

Figure 4.20: Fluxgate output sideband amplitude.

harmonic of fluxgate output voltage ($2f_{exc} = 31.25$ kHz). These peaks are at 31.187 kHz and 31.313 kHz (31.25 kHz ± 63 Hz). The sideband sensitivity is calculated using equation (4.42). The results of sensitivity calculation are depicted in figure 4.21.

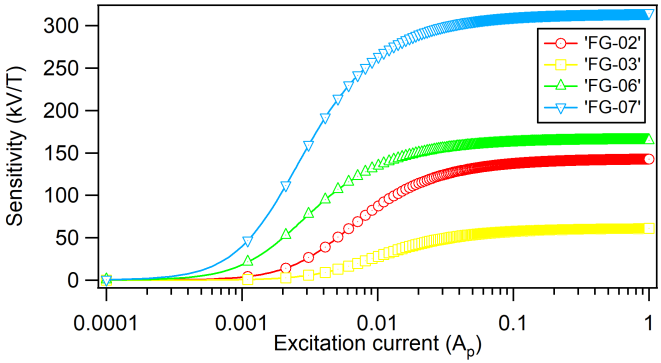

Figure 4.21: Calculated fluxgate output sensitivity.

To verify the calculation result, it is then compared to the measurement result. Figure 4.22 shows the calculated and measured sideband sensitivity comparison of FG-06 sensor.

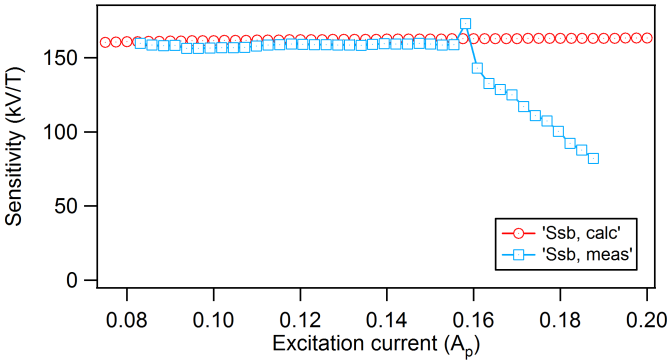

Figure 4.22: Calculated and measured sideband sensitivity comparison of FG-06.

The curves in the figure show the similarity of calculated and measured sensitivity for the excitation current below 0.16 A_p, but it also shows big differences for the excitation current above 0.16 A_p, because the excitation is distorted for the current above 0.16 A_p. The flat response of the sensitivity on the current is caused by the compensation between the peak value and pulse width of output signal. If the current is higher, the peak value would be higher but on the other hand the pulse width would be narrower. And the integration would give the same value for this change.
The calculated and measured sensitivity of the fluxgate sensors as well as the p and q values are listed in table 4.5. These results show the sensitivity at the same excitation current of 0.1 A_p. We can see that the results are quite similar. From the calculation it is obtained that the inductance decrease slope q does not affect the output voltage sensitivity but only the peak value of output signal. The same is seen for the current effect. This peak value is compensated by the width of signal. Therefore, the sensitivity stays the same for different q values.
The result shows that the calculated sensitivity using equation (4.38) agrees with the measurement result. Both results are proportionally related to the secondary winding number and the inductance change as included in the equation. It can be seen that fluxgate sensors with large secondary winding number and high inductance change would have large sensitivity. This is seen for FG-07 sensor, which has the highest secondary winding number and the highest inductance change and this is the sensor with the highest sensitivity. The FG-02 sensor, which has quite large inductance change and small secondary winding number, shows a high sensitivity as well.

Table 4.5: Fluxgate sensitivity calculation and measurement results.

Sensor	p ($\times 10^{-3}$)	q	T_{pulse} (μs)	Sideband sensitivity (V/T)	
				Calculated	Measured
FG-02	1.254	224.7	6.21	136280	141104
FG-03	0.383	148.6	5.76	58042	57771
FG-06	0.965	502.2	5.42	162350	156186
FG-07	1.267	543.9	6.54	310470	334729

4.3.7 Fluxgate Sensor Response on Magnetic Field

The fluxgate sensor response on magnetic field is performed to see how the fluxgate output voltage behaves in response to the input magnetic field. Both, calculation and measurement are shown. The excitation current for this test is set at the same current of 0.1 A_p. The external field is varied with some increments, where the increment for calculation is 10 nT with linear step and the increment for measurement is 10 nT with logarithmic step. The calculation process is done by inserting the field value into equation (4.38) and then it is integrated in (4.41). This can be done in Matlab with array data. The calculation result of fluxgate sensor response on magnetic field for FG-06 is shown in figure 4.23. The

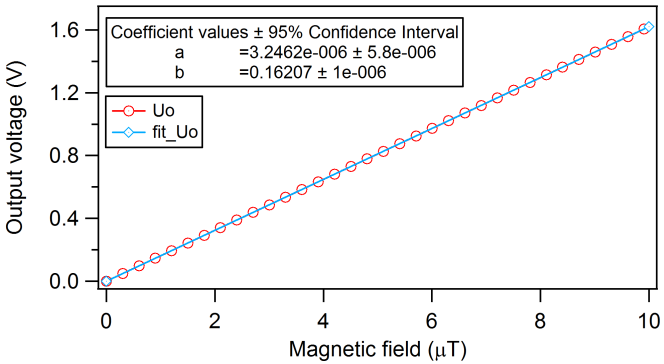

Figure 4.23: Magnetic field calculation response using FG-06.

figure shows a very linear curve between output voltage and magnetic field. The sensitivity can also be obtained by fitting this curve instead of using equation (4.42). The linear regression is used as the fitting function as seen in the figure. The linear regression equation of this function is

$$u_o = 3.25 \times 10^{-6} + 0.16207 \cdot B_{ext} \approx 0.16207 \cdot B_{ext}, \tag{4.55}$$

B_{ext} is the external flux density in μT.

The result shows that the obtained sensitivity from this fitting is very similar to the calculated sensitivity from equation (4.42) or in table 4.5, which is 162070 V/T from the fitting and 162350 V/T from the equation. The measurement is carried out by providing some field values using the solenoid to the sensor, and the sideband output voltage is measured at the same time. The field is an ac modulated function with a frequency of 63 Hz. The measurement result of fluxgate sensor response to magnetic field for FG-06 is shown in figure 4.24. The curve in figure 4.24 shows a

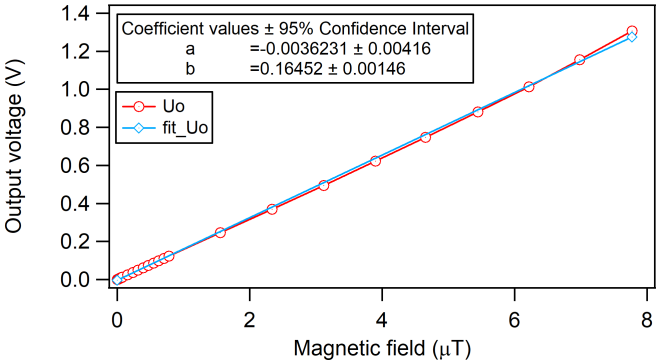

Figure 4.24: Magnetic field measurement response using FG-06.

linear curve of the measured magnetic field. The same with the calculated result, the measured result is fitted using linear regression to obtain the sensitivity. The fitting result shows a little bit difference with respect the values in table 4.5, which is 164520 V/T from the fitting and 156186 V/T from table 4.5. It is clearly true because the fitting is the result of averaging and the value in table 4.5 is only shown for one magnetic field value.
Figure 4.25 shows the comparison between calculation and measurement result for FG-06. It is seen that both curves coincide and have quite similar sensitivity, that is 162070 V/T from the calculation and 164520 V/T from the measurement.

4.4 Fluxgate Sensor Symmetry

The first harmonic of the fluxgate output signal appears as a consequence of asymmetry of the fluxgate sensor [73, 135]. The asymmetry causes the fundamental frequency signal to be not balanced, therefore, there is some signal with this fundamental frequency, which leaks to the output signal of the fluxgate sensor.
The fluxgate output signal consists of several harmonics. It is starting from the fundamental frequency of the excitation up to higher order harmonics. Normally the odd harmonics will not appear on the fluxgate output, but

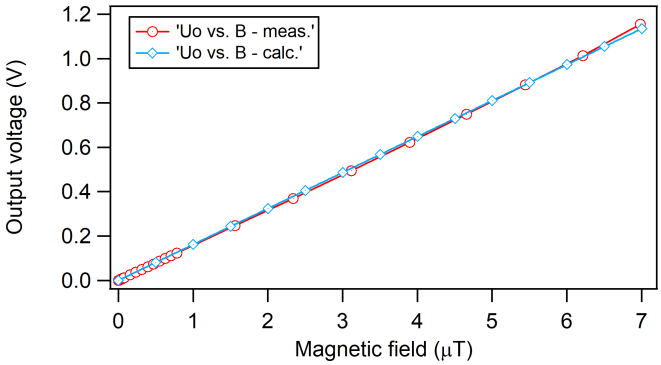

Figure 4.25: Output voltage of magnetic field calculation and measurement response using FG-06.

will be compensated by the other pair of the fluxgate. Only the even harmonics will remain. But, due to the asymmetry of the fluxgate sensor, the odd harmonics appear. As equations (2.9) and (2.10) show, the odd harmonics will be canceled if the fluxgate sensor is symmetric.

4.5 Fluxgate Sensor Closed-loop Circuit

4.5.1 Fluxgate Closed-loop Principle

The fluxgate sensor is operated in a closed-loop circuit, where the output is fed back to the sensor through a compensation coil. The field from the compensation coil is in the opposite direction to the external field. Thus, the field from the compensation coil counters the external magnetic field to make it zero [73]. Figure 4.26 shows the simple closed-loop diagram of fluxgate sensor system. On the sensor part, there are three coils denoted as primary (Pri.), secondary (Sec.) and compensation (Comp.) coil. Here, the compensation is done with a dedicated feedback coil, while other fluxgate readout systems sometimes share the secondary coil for the compensation. An amplifier amplifies the signal from the sensor. The amplifier is a non-inverting type. A gain of 2 is good enough for the amplification because the sensor's output voltage is already large and does not need high gain. Moreover, the purpose of the amplifier is mostly to be used as a buffer rather than as amplifier itself. Then, to demodulate the output signal from the sensor, a phase-sensitive detector (PSD) is implemented. The PSD is synchronized with the excitation frequency f_{exc} to get the same phase reference. The PSD would pass the harmonic of sensor's output associated with the PSD's input frequency. In this study, the second harmonic of excitation frequency is used, since the second harmonic is the largest amplitude representation of external magnetic

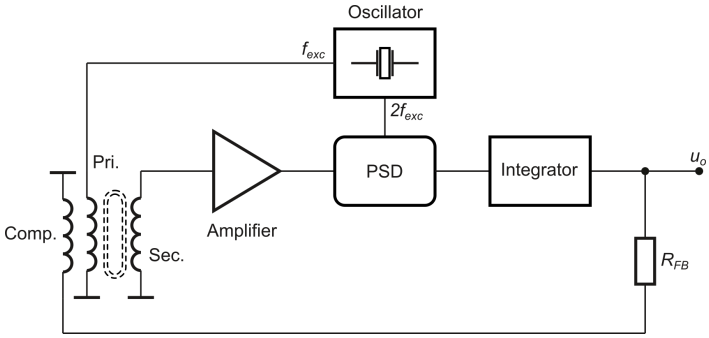

Figure 4.26: Fluxgate closed-loop circuit.

field. An integrator sums the passed signal from the PSD to a DC voltage as a representation of measured external magnetic field. In this circuit, a low-pass filter with a pole far below the second harmonic frequency is used and determines the desired measurement bandwidth of 3 kHz. Therefore, the filter would effectively integrate the second harmonic signal and passes the desired measurement bandwidth. A quartz crystal oscillator generates a square wave signal for the excitation and the PSD. The signal is divided by a clock divider before it is delivered to the excitation coil driver and the PSD. The output voltage is fed back to the compensation coil through a feedback resistor R_{fb}, where the function of the resistor is to convert the output voltage to a feedback current for the compensation coil, which later changes the current to the magnetic field in order to counter the external magnetic field in the sensor.
When the output voltage is fed back to the compensation coil, the output noise is also fed back to the compensation coil in the form of current noise. But it is divided by the resistor value and converted to a magnetic field noise by the compensation coil's constant S_{FB}. The current noise at the compensation follows equation (4.56).

$$\sqrt{S_{i,FB}} = \frac{\sqrt{S_{u_o}}}{R_{FB}} \tag{4.56}$$

where $\sqrt{S_{i,FB}}$ is the current noise and $\sqrt{S_{u_o}}$ is the output noise. Since the output voltage is proportionally related to the noise, equation (4.56) is also applicable for the output signal and the feedback current. In spite of that, the equation can be used to adjust the sensitivity of the closed-loop circuit by changing the R_{FB} value.

4.5.2 Closed-loop Circuit Stability

The fluxgate closed-loop circuit provides a cyclic gain between input and output. The gain at open-loop must be compensated by the feedback

resistor to make a balance in the closed-loop. And the closed-loop would work well if there is no phase delay between input and output. The phase delay, which might be present in the circuit tends to cause an instability in the loop. At the end, this causes the noise to be higher than the open-loop one. Therefore, it is important to optimize the circuit by making a zero phase delay to suppress the noise at the output. However, most of the circuit parts create some phase delay such as the amplifier and the integrator. By incorporating all the parts, the sum of phase delay in the closed-loop must be π, as shown in (4.57):

$$\sum \Delta\phi = \pi = \Delta\phi_{amp} + \Delta\phi_{PSD} + \Delta\phi_{Int} + \Delta\phi_{FB}. \tag{4.57}$$

where $\Delta\phi_{amp}$ is the amplifier phase delay, $\Delta\phi_{PSD}$ is the PSD phase delay, $\Delta\phi_{Int}$ is the integrator phase delay, and $\Delta\phi_{FB}$ is the feedback phase delay.
The phase delay of the amplifier is almost zero. There are only some real external components involved since the gain is only obtained from two resistors. The possible imaginary component is the internal input capacitance, which its value is relatively small. The phase delay of the PSD is also zero, since it is synchronized with the excitation source. The possibility of high phase delay could occur in the integrator because of the capacitor, which could create a pole. The phase delay of the integrator can be minimized by shifting the pole of the filter to higher frequencies to accommodate the desired bandwidth, but on the other hand it reduces the ability to block the second harmonic output frequency. So the pole should be set at where there is no delay within the desired bandwidth. The feedback circuit also creates the phase delay due to the used compensation coil. High resistance compensation coil should be used to reduce the feedback phase delay.
The phase delay of all parts are fix. So, the sum of phase delays might not be π. In order to adjust the total phase delay, the phase of PSD is made adjustable by shifting its synchronization frequency phase. Therefore, the phase difference caused by the filter, feedback circuit, and others can be compensated by the PSD phase adjustment to make the total phase delay π.

4.5.3 Electronic Circuit Noise

The electronic circuit noise is the noise generated only by the electronic devices in the circuit. The main sources are the active components such as op-amps and the passive components such as resistors and so on. The active components produce flicker noise and white noise, while the passive components produce white noise. The total electronic noise is the sum of these noises.

4.5.4 Fluxgate Sensor Noise

The fluxgate sensor noise is derived from the sensor element without the electronics. The sensor is directly connected to the spectrum analyzer

while measuring its noise, so that only its intrinsic noise is measured. The sensors used in the noise test are listed in table 4.4. The noise measurement results of several tested sensors are depicted in figure 4.27. It is seen from the figure that the fluxgate has very low noise values, where

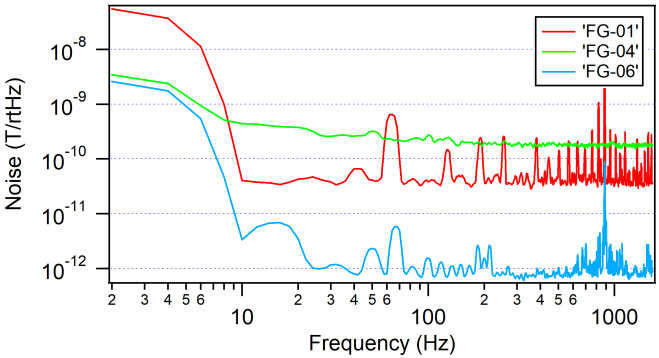

Figure 4.27: Fluxgate sensor noise.

the minimum noise is below 1 pT$\sqrt{Hz}$ for fluxgate FG-06.

4.5.5 Fluxgate Sensor System Noise

Fluxgate sensor system noise is the combination of fluxgate sensor noise and the electronic circuit noise. The noise measurement result of fluxgate sensor system is depicted in figure 4.28.

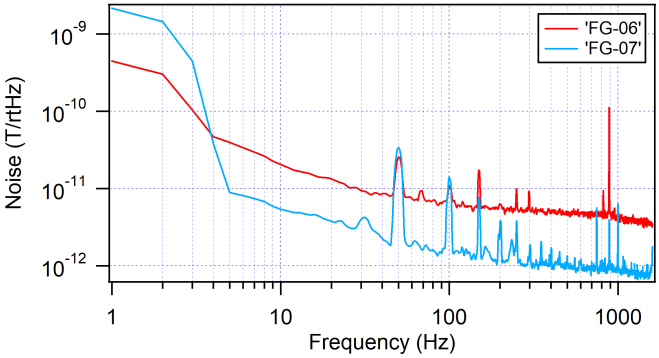

Figure 4.28: Fluxgate sensor system noise (closed-loop).

From the result, the low noise fluxgate sensor output for all sensors is obtained. The noise spectrum shows that a noise level below 10 pT/$\sqrt{Hz}$ at 1 kHz is achieved for both sensors FG-06 and FG-07. This results are comparable to the lowest noise of the commercially available fluxgate sensors [114, 136].

5 Conclusion

This thesis discussed about the fluxgate characterization by utilizing the impedance measurement in order to improve the fluxgate performance on its sensitivity and noise properties. To realize that purposes, several works have to be done. They are the development and characterization of the impedance measuring instrument, the development of the fluxgate output voltage theory, the construction of the fluxgate sensor based on the obtained theory, and the improvement of electronic circuit with feedback loop of the fluxgate sensor system.

On the instrument development, an instrument for fluxgate characterization by impedance measurement based on an auto-balanced circuit has been developed and characterized. Even the circuits for signal processing have been perfectly matched, the measurement error still emerges due to frequency-dependent gain and phase reading error. A linear calibrating function is implemented to diminish the error. Thus, the system works very well yielding the smaller error and better accuracy for fixed resistances and inductances measurements. All coils of the fluxgate sensor can be measured and show reliable results. The comparison results of each coil shows the coincidence when performing the resistance measurement using the FG Analyzer and multimeter HP 34401A and the inductance measurement using the FG Analyzer and Agilent 4294A.

The inductance measurement results for low frequency depend on the applied current if cores with high permeability are used. It yields the incorrect measurement results if the applied current exceeds a certain current limit in this frequency range. Therefore the measurement should not be performed above this limit. For the tested fluxgate sensor this current limit is very small, which is about 0.05 mA. This current limit can not be reached by the Agilent 4294A and the FG Analyzer can be used instead.

For the fluxgate output theory, it has also been developed the equation for fluxgate output calculation and it has also been shown that the measurement results agree with the calculation using a model to fit the primary

coils' inductance. The equation utilizes the inductance-change of the primary coil due to the saturation caused by the excitation current. The inductance is measured with the DC offset and the obtained function is used to determine the fluxgate output sensor.
Based on the obtained theory, several fluxgate sensors have been built. The sensitivity and noise measurement of these sensor show good results, where the obtained sensitivity and noise are high and low enough, respectively. The improvement of electronic circuit with feedback loop of the fluxgate sensor system also shows a good result. It works well although the obtained output sensitivity and noise are supposed to be a little bit lower than the obtained one from the sideband measurement.
From the results, it can prove that the developed methods can predict the sideband sensitivity of fluxgate sensor using inductance instead of permeability parameters. In addition, it can describe the signal and sensitivity function of the fuxgate output voltage in time or excitation current domain. In the end, the implementation of inductance measurement on fluxgate characterization offers a new approach to develop fluxgate sensor better.

List of Figures

List of Tables

References

[1] C. Shelton, "The ring fluxgate: A very modern 80-year old", *Sensor Review*, vol. 27, no. 4, pp. 332–340, 2007 (pages 1, 11).

[2] F. Jie, "Study of orthogonal fluxgate sensor in terms of sensitivity and noise", PhD Thesis, National University of Singapore, 2010 (pages 1, 29).

[3] P. Clarke. (2017). Magnetic sensor market on 7% CAGR, [Online]. Available: `http://www.eenewseurope.com/news/magnetic-sensor-market-7-cagr-0` (page 1).

[4] R. L. Fagaly and S. A. Macintyre, "Magnetic field measurement", in *Measurement, Instrumentation, and Sensors Handbook, Second Edition: Electromagnetic, Optical, Radiation, Chemical, and Biomedical Measurement*, J. G. Webster and H. Eren, Eds. CRC Press, 2014, p. 1921 (pages 2–3, 9).

[5] J. Lenz and A. S. Edelstein, "Magnetic sensors and their applications", *IEEE Sensors Journal*, vol. 6, no. 3, 2006 (pages 3, 26).

[6] R. L. Fagaly, "Superconducting quantum interference device instruments and applications", *Review of scientific instruments*, vol. 77, no. 10, p. 101 101, 2006 (page 3).

[7] D. Drung, "High-T_c and low-T_c dc SQUID electronics", *Superconductor science and technology*, vol. 16, no. 12, pp. 1320–1336, 2003 (page 3).

[8] M. Crescentini, M. Marchesi, A. Romani, M. Tartagni, and P. A. Traverso, "A broadband, on-chip sensor based on Hall effect for current measurements in smart power circuits", *IEEE Transactions on Instrumentation and Measurement*, vol. 67, no. 6, pp. 1470–1485, 2018 (page 3).

[9] M. Dąbek, P. Wiśniowski, T. Stobiecki, J. Wrona, S. Cardoso, and P. P. Freitas, "Sensitivity and 3 dB bandwidth in single and series-connected tunneling magnetoresistive sensors", *Sensors*, vol. 16, no. 11, p. 1821, 2016 (page 3).

[10] S. Tumanski, "Induction coil sensors - a review", *Measurement Science and Technology*, vol. 18, no. 3, R31–R46, 2007 (page 3).

[11] *Proton magnetometer - Brochure*, Gem Systems Inc., 2018 (page 3).

[12] V. Tiporlini and K. Alameh, "High sensitivity optically pumped quantum magnetometer", *The Scientific World Journal*, vol. 2013, no. 858379, p. 8, 2013 (page 3).

[13] R. Jiménez-Martínez and S. Knappe, "Microfabricated optically-pumped magnetometers", in *Smart sensors, measurement and instrumentation: High Sensitivity Magnetometers*, A. Grosz *et al.*, Eds. 2017 (page 3).

[14] S. Tumanski, *Handbook of magnetic field measurements, Magnetic sensors*. CRC Press, 2011 (pages 3, 10, 20–22).

[15] S. Tumanski, "A review of magnetic sensors", *Przegląd Elektrotechniczny*, vol. 80, pp. 74–80, 2004 (page 3).

[16] P. Ripka, *Magnetic sensors and magnetometers*. Artech House, 2001 (pages 3, 10).

[17] S. Tumanski, "Modern magnetic field sensors - a review", *Przegląd Elektrotechniczny*, no. 10, 2013 (page 3).

[18] P. Ripka and M. Janosek, "Advances in magnetic field sensors", *IEEE Sensors Journal*, vol. 10, no. 6, 2010 (pages 3–4, 15, 33).

[19] C. Hinnrichs, J. Stahl, K. Kuchenbrandt, and M. Schilling, "Dependence of sensitivity and noise of fluxgate Sensors on Racetrack Geometry", *IEEE Transactions on Magnetics*, vol. 37, no. 4, 2001 (pages 5, 13, 26, 28–30, 61, 73, 75).

[20] D. Ciudad, M. Díaz-Michelena, L. Pérez, and C. Aroca, "Small fluxgate magnetometers: Development and future trends in spain", *Sensors*, vol. 10, pp. 1859–1870, 2010 (pages 5, 15, 61).

[21] K. Klopfer, U. Niedermayer, H. Klingbeil, W. Ackermann, H. G. König, and T. Weiland, "Measurement of the magnetic material properties for ferrite-loaded cavities", *Physical Review Accelerators and Beams*, vol. 18, p. 010 101, 2015 (pages 5, 62).

[22] V. Dumbrava and L. Svilainis, "Measurement of complex permeability of magnetic materials", *Matavimai*, vol. 37, no. 1, 2006 (pages 5, 62).

[23] V. Dumbrava and L. Svilainis, "The automated complex impedance measurement system", *Elektronika Ir Elektrotechnika*, vol. 76, no. 4, 2007 (pages 5, 62).

[24] B. Hu, J. Wang, G. Song, and F. Zhang, "A compact wideband precision impedance measurement system based on digital auto-balancing bridge", *Measurement Science and Technology*, vol. 27, no. 5, p. 055 902, 2016 (pages 5, 62).

[25] J. Wissenwasser, M. J. Vellekoop, W. Kapferer, G. Lepperdinger, and R. Heer, "Multifrequency impedance measurement technique for wireless characterization of microbiological cell cultures", *Review of Scientific Instruments*, vol. 82, p. 115 110, 2011 (pages 5, 62).

[26] P. Ripka, "Advances in fluxgate sensors", *Sensors and Actuators A: Physical*, vol. 106, pp. 8–14, 2003 (pages 10, 15, 22, 78).

[27] P. Ripka, F. Primdahl, O. V. Nielsen, J. R. Petersen, and A. Ranta, "A.C. magnetic-field measurement using the fluxgate", *Sensors and Actuators A: Physical*, vol. 46, no. 1–3, pp. 307–311, 1995 (page 10).

[28] C.-C. Lu, J. Huang, P.-K. Chiu, S.-L. Chiu, and J.-T. Jeng, "High-sensitivity low-noise miniature fluxgate magnetometers using a flip chip conceptual design", *Sensors*, vol. 14, pp. 13 815–13 829, 2014 (page 10).

[29] D. Rühmer, S. Bögeholz, F. Ludwig, and M. Schilling, "Vector fluxgate magnetometer for high operation temperatures up to 250°C", *Sensors and Actuators A: Physical*, vol. 228, pp. 118–124, 2015 (pages 10, 13).

[30] F. Kaluza, A. Grueger, and H. Grueger, "New and future applications of fluxgate sensors", *Sensors and Actuators A: Physical*, vol. 106, pp. 48–51, 2003 (pages 11, 15).

[31] W. Li and J. Wang, "Magnetic sensors for navigation applications: An overview", *The Journal of Navigation*, vol. 67, pp. 263–275, 2014 (page 11).

[32] V. Petrucha, "An improved version of the fluxgate compass module", *Acta Polytechnica*, vol. 47, no. 4–5, 2007 (page 11).

[33] J. Kennedy, J. Leveneur, J. Turner, J. Futter, and G. V. M. Williams, "Applications of nanoparticle-based fluxgate magnetometers for positioning and location", in *2014 IEEE Sensors Applications Symposium (SAS)*, 2014, pp. 228–232 (page 11).

[34] D. G. Macharet, H. I. A. Perez-Imaz, P. A. F. Rezeck, G. A. Potje, L. C. C. Benyosef, A. Wiermann, G. M. Freitas, L. G. U. Garcia, and M. F. M. Campos, "Autonomous aeromagnetic surveys using a fluxgate magnetometer", *Sensors*, vol. 16, no. 12, p. 2169, 2016 (page 11).

[35] B. Instruments. (2018). Geosciences applications of fluxgate sensor, [Online]. Available: `http://www.bartington.com/geosciences-magnetic-field-instrument-applications.html` (visited on 05/14/2018) (pages 11–12).

[36] G. Bruno, A.-A. Rozan, M. Marc, C. Frédéric, and D. Catherine, "On the use of fluxgate 3-axis magnetometers in archaeology: Application with a multisensor device on the site of Qasr 'Allam in the western desert of Egypt", *Archaeological Prospection*, vol. 24, no. 1, pp. 59–73, 2016 (page 12).

[37] B. Instruments. (2018). Medical applications of fluxgate sensor, [Online]. Available: `http://www.bartington.com/medical.html` (visited on 06/21/2018) (page 12).

[38] P. Ripka, "Biomedical applications of fluxgate sensors", in *Progress in Electromagnetic Research Symposium*, 2004 (page 12).

[39] J. Tomek, A. Platil, P. Ripka, and P. Kaspar, "Application of fluxgate gradiometer in magnetopneumography", *Sensors and Actuators A: Physical*, vol. 132, no. 1, pp. 214–217, 2006 (page 12).

[40] R. Rybalko, J. Haueisen, and C. Hofmann, "New type of fluxgate magnetometer for the heart's magnetic field detection", *Current Directions in Biomedical Engineering*, vol. 1, pp. 22–25, 2015 (page 12).

[41] J. Wang and X. Chen, "A fluxgate magnetometer for navigation and sensing: Noise character and digital filtering", in *Sensors, 2015 IEEE*, 2015 (page 12).

[42] D. M. Miles, J. R. Bennest, I. R. Mann, and D. K. Millling, "A radiation hardened digital fluxgate magnetometer for space applications", *Geoscientific Instrumentation, Methods and Data Systems*, vol. 2, no. 2, pp. 213–224, 2013 (page 13).

[43] P. Sharma, "Magnetic method applied to mineral exploration", *Ore Geology Reviews*, vol. 2, no. 4, pp. 323–357, 1987 (page 13).

[44] P. Ripka, "Magnetic sensors for industrial and field applications", *Sensors and Actuators A: Physical*, vol. 42, no. 1, pp. 394–397, 1994 (page 13).

[45] F. Förster, "A method for the measurement of dc field differences and its application to nondestructive testing", *Nondestructive Test*, vol. 13, p. 31, 1955 (page 13).

[46] W. Bornhofft and G. Trenkler, "Magnetic Field Sensors : Flux Gate Sensors", in *Sensors, a Comprehensive Survey*, W. Gopel, J. Hesse, and J. Zemel, Eds. VCH, 1989 (page 13).

[47] R. H. Koch and J. R. Rozen, "Low-noise flux-gate magnetic-field sensors using ring- and rod-core geometries", *Applied Physics Letters*, vol. 78, no. 13, 2001 (pages 13, 30).

[48] C. Hinnrichs, C. Pels, and M. Schilling, "Noise and linearity of a fluxgate magnetometer in racetrack geometry", *Journal of Applied Physics*, vol. 87, no. 9, 2000 (pages 13, 22).

[49] J. Kubik and P. Ripka, "Racetrack fluxgate sensor core demagnetization factor", *Sensors and Actuators A: Physical*, vol. 143, pp. 237–244, 2008 (pages 13, 23, 71).

[50] A. Baschirotto, E. Dallago, M. Ferri, P. Malcovati, A. Rossini, and G. Venchi, "A 2D micro-fluxgate earth magnetic field measurement systems with fully automated acquisition setup", *Measurement*, vol. 43, pp. 46–53, 2010 (page 13).

[51] C. Lei, J. Lei, Z. Yang, T. Wang, and Y. Zhou, "A low power micro fluxgate sensor with improved magnetic core", *Microsystem Technologies*, vol. 19, pp. 591–598, 2013 (page 13).

[52] P. Ripka, S. Kawahito, S. O. Choi, A. Tipek, and M. Ishida, "Micro-fluxgate sensor with closed core", *Sensors and Actuators A: Physical*, vol. 91, pp. 65–69, 2001 (pages 13–14).

[53] C. Lei, Y. Liu, X.-C. Sun, T. Wang, Z. Yang, and Y. Zhou, "Improved performance of integrated solenoid fluxgate sensor chip using a bilayer Co-based ribbon core", *IEEE Sensors Journal*, vol. 15, no. 9, 2015 (page 13).

[54] S. Schoinas, A.-M. E. Guamra, F. Moreillon, and P. Passeraub, "A flexible pad-printed fluxgate sensor", *Proceedings*, vol. 1, no. 4, p. 615, 2017 (page 14).

[55] M. Janošek and P. Ripka, "PCB sensors in fluxgate magnetometer with controlled excitation", *Sensors and Actuators A: Physical*, vol. 151, pp. 141–144, 2009 (page 14).

[56] A. Tipek, P. Ripka, T. O'Donnell, and J. Kubik, "PCB technology used in fluxgate sensor construction", *Sensors and Actuators A: Physical*, vol. 115, pp. 286–292, 2004 (page 14).

[57] I. Vincueria, M. Tudanca, C. Aroca, E. Lopez, M. C. Sanchez, and P. Sanchez, "Flux-Gate Sensor Based on Planar Technology", *IEEE Transactions on Magnetics*, vol. 30, no. 6, 1994 (page 15).

[58] P. Ripka, "Review of fluxgate sensors", *Sensors and Actuators A: Physical*, vol. 33, pp. 129–141, 1992 (page 16).

[59] F. Ludwig, "Induktionsspulen und fluxgate-sensoren", in *Presentation Handout*, (pages 16, 18).

[60] F. Liorzou, B. Phelps, and D. L. Atherton, "Macroscopic models of magnetization", *IEEE Transactions on Magnetics*, vol. 36, no. 2, 2000 (page 16).

[61] Y. Wang, S. Wu, Z. Zhou, D. Cheng, N. Pang, and Y. Wan, "Research on the dynamic hysteresis loop model of the residence times difference (RTD) - fluxgate", *Sensors*, vol. 13, pp. 11 539–11 552, 2013 (page 16).

[62] F. Preisach, "Ueber die magnetische nachwirkung", *Zeitschrift fuer Physik*, vol. 94, pp. 277–302, 1935 (page 16).

[63] A. Globus, P. Duplex, and M. Guyot, "Determination of initial magnetization curve from crystallites size and effective anisotropy field", *IEEE Transactions on Magnetics*, 1971 (page 17).

[64] D. C. Jiles and D. L. Atherton, "Theory of ferromagnetic hysteresis (invited)", *Journal of Applied Physics*, vol. 55, no. 6, 1984 (page 17).

[65] M. A. Zaman and M. A. Matin, "Optimization of Jiles-Atherton hysteresis model parameters using Taguchi's method", *IEEE Transactions on Magnetics*, vol. 51, no. 5, 2015 (page 17).

[66] D. Gordon, R. Lundsten, and R. A. Chiarodo, "Factors affecting the sensitivity of gamma-level ring-core magnetometers", *IEEE Transactions on Magnetics*, vol. 1, no. 4, 1965 (page 17).

[67] S. V. Marshall, "An analytic model for the fluxgate magnetometer", *IEEE Transactions on Magnetics*, 1967 (page 17).

[68] F. Primdahl, "The fluxgate mechanism, part I: The gating curves of parallel and orthogonal fluxgates", *IEEE Transactions on Magnetics*, vol. 6, no. 2, 1970 (page 17).

[69] J. R. Burger, "The theoretical output of a ring core fluxgate sensor", *IEEE Transactions on Magnetics*, vol. 8, no. 4, 1972 (page 17).

[70] J. G. Deak, R. H. Koch, G. E. Guthmiller, and R. E. F. Jr., "Dynamic calculation of the responsivity of monodomain fluxgate magnetometers", *IEEE Transactions on Magnetics*, vol. 36, no. 4, 2000 (page 17).

[71] H. How and C. Vittoria, "Generation of high-order harmonics in insulator magnetic fluxgate sensor cores", *IEEE Transactions on Magnetics*, vol. 37, no. 4, 2001 (page 17).

[72] A. L. Geiler, V. G. Harris, C. Vittoria, and N. X. Sun, "A quantitative model for the nonlinear response of fluxgate magnetometers", *Journal of Applied Physics*, vol. 99, 2006 (pages 17–20).

[73] M. Janoseˇk, "Parallel Fluxgate Magnetometers", in *Smart sensors, measurement and instrumentation: High sensitivity magnetometers*, A. Grosz *et al.*, Eds. 2017 (pages 17, 20, 22, 90–91).

[74] S. X. Wang and A. M. Taratorin, *Magnetic information storage technology*. 1999 (page 18).

[75] F. Primdahl, B. Hernando, O. V. Nielsen, and J. R. Petersen, "Demagnetising factor and noise in the fluxgate ring-core sensor", *Journal of Physics E: Scientific Instruments*, vol. 22, pp. 1004–1008, 1989 (pages 20, 23).

[76] F. Primdahl, P. Brauer, J. M. G. Merayo, and O. V. Nielsen, "The fluxgate ring-core internal field", *Measurement Science and Technology*, vol. 13, 2002 (pages 20, 23).

[77] M. H. Acuna, "Fluxgate magnetometers for outer planets exploration", *IEEE Transactions on Magnetics*, vol. 10, no. 3, pp. 519–523, 1974 (page 23).

[78] W. Ye, W. Zhu, L. Zhang, and G. Fang, "A quantitative model for the sensitivity of untuned voltage output fluxgate sensors", *IEEE Sensors Journal*, vol. 16, no. 22, 2016 (page 23).

[79] P. Ripka and W. G. Hurley, "Excitation efficiency of fluxgate sensors", *Sensors and Actuators A: Physical*, vol. 129, pp. 75–79, 2006 (page 24).

[80] S. C. Tang, M. C. Duffy, P. Ripka, and W. Hurley, "Excitation circuit for fluxgate sensor using saturable inductor", *Sensors and Actuators A: Physical*, vol. 113, pp. 156–165, 2004 (pages 24–26).

[81] Z.-C. Gao and R. D. Russell, "Fluxgate sensor theory: Sensitivity and phase plane analysis", *IEEE Transactions on Geoscience and Remote Sensing*, vol. 25, no. 6, 1987 (page 26).

[82] Y. Cao and D. Cao, "Theory of fluxgate sensor: Stability condition and critical resistance", *Sensors and Actuators A: Physical*, vol. 233, pp. 522–531, 2015 (page 27).

[83] P. Ripka and F. Primdahl, "Tuned current-output fluxgate", *Sensors and Actuators A: Physical*, vol. 82, pp. 161–166, 2000 (page 27).

[84] M. van Exter, "Noise and signal processing", in *Extra syllabus for course "Signaalverwerking & Ruis" Universiteit Leiden*, 2003 (pages 27–28).

[85] R. H. Koch, J. G. Deak, and G. Grinstein, "Fundamental limits to magnetic-field sensitivity of flux-gate magnetic-field sensors", *Applied Physics Letters*, vol. 75, no. 24, 1999 (pages 28, 30, 73).

[86] W. M. Leach, "Fundamentals of low-noise analog circuit design", *Proceedings of the IEEE*, vol. 82, no. 10, pp. 1515–1538, 1994 (page 29).

[87] M. Butta and I. Sasada, "Sources of noise in a magnetometer based on orthogonal fluxgate operated in fundamental mode", *IEEE Transactions on Magnetics*, vol. 48, no. 4, 2012 (pages 29–30).

[88] C.-G. Stefanita, "Barkhausen Noise as a Magnetic Nondestructive Testing Technique", in *From Bulk to Nano: The Many Sides of Magnetism*, R. Hull, Ed. Berlin, Heidelberg: Springer Berlin Heidelberg, 2008, pp. 19–40 (pages 29–30).

[89] B. Cerruti and S. Zapperi, "Barkhausen noise from zigzag domain walls", *Journal of Statistical Mechanics: Theory and Experiment*, vol. 2006, no. 08, P08020, 2006 (page 29).

[90] R. M. Bozorth, *Ferromagnetism*. Wiley-IEEE Press, 1993 (page 29).

[91] W. Theiner and H. Williams, "Determination of Microstructural Parameters by Magnetic and Ultrasonic Quantitative NDE", in *Nondestructive Methods Material Property Determination*, C. O. Ruud and R. E. Green Jr., Eds. Plenum Press, New York, 1984 (page 29).

[92] S. Chikazumi and C. Graham, *Physics of Ferromagnetism*. Clarendon Press, 1997 (page 29).

[93] J. L. M. J. van Bree, J. A. Poulis, and F. N. Hooge, "Barkhausen noise in fluxgate magnetometers", *Applied Scientific Research*, vol. 29, no. 4, 1974 (page 30).

[94] O. Ozatay, T. Hauet, P. Braganca, L. Wan, P. Mather, M. Schneider, and J.-U. Thiele, "Spin-Based Data Storage", in *Reference Module in Materials Science and Materials Engineering*, Elsevier, 2016 (page 30).

[95] J. Deak, A. H. Miklich, J. Slonczewski, and R. H. Koch, "A low-noise single-domain fluxgate sensor", *Applied Physics Letters*, vol. 69, no. 8, 1996 (page 30).

[96] B. B. Narod, "The origin of noise and magnetic hysteresis in crystalline permalloy ring-core fluxgate sensors", *Geoscientific Instrumentation, Methods and Data Systems*, vol. 3, pp. 201–210, 2014 (page 30).

[97] *Impedance Measurement Handbook: A guide to measurement technology and techniques - Application Note*, 6th Edition, Keysight Technologies, Nov. 2016 (page 31).

[98] Vacuumschmelze, *Soft Magnetic Materials and Semi-finished Products*, Application note, 2002 (pages 33, 74).

[99] A. Baschirotto, E. Dallago, P. Malcovati, M. Marchesi, and G. Venchi, "Precise vector-2D magnetic field sensor system for electronic compass", *Proceedings of IEEE Sensors*, vol. 2, p. 1028, 2004 (pages 33, 71, 74).

[100] A. Platil and P. Ripka, "Fluxgate sensor and real operating-mode B-H curve", *Journal of Electrical Engineering*, vol. 63, no. 7s, pp. 118–121, 2012 (pages 38–39).

[101] D. W. Knight, "The self-resonance and self-capacitance of solenoid coils: applicable theory, models and calculation methods", Experiment and measurement, 2016 (page 42).

[102] H. Nagaoka, "The inductance coefficients of solenoids", *Journal of The College of Science*, vol. 27, no. 6, p. 18, 1909 (pages 42, 75).

[103] M. J. Schauber *et al.*, "Measurement of mutual inductance from frequency dependence of impedance of AC coupled circuits using a digital dual-phase lock-in amplifier", *American Journal of Physics*, vol. 76, no. 2, pp. 129–132, 2008 (page 44).

[104] P. Ripka and W. G. Hurley, "Excitation tuning in fluxgate sensors", in *IMTC/2002. Proceedings of the 19th IEEE Instrumentation and Measurement Technology Conference (IEEE Cat. No.00CH37276)*, vol. 1, 2002, pp. 677–680 (page 54).

[105] L. Hasselgren, E. Moeller, and Y. Hamnerius, "Calculation of magnetic shielding of a substation at power frequency using FEM", *IEEE Transactions on Power Delivery*, vol. 9, no. 3, 1994 (page 58).

[106] I. Altarev *et al.*, "A magnetically shielded room with ultra low residual field and gradient", *Review of Scientific Instruments*, vol. 85, p. 075 106, 2014 (page 59).

[107] I. Altarev *et al.*, "A large-scale magnetic shield with 106 damping at millihertz frequencies", *Journal of Applied Physics*, vol. 117, p. 183 903, 2015 (page 59).

[108] V. O. Kelhä *et al.*, "Design, construction, and performance of a large-volume magnetic shield", *IEEE Transactions on Magnetics*, vol. 18, no. 1, 1982 (page 59).

[109] E. A. Donley, E. Hodby, L. Hollberg, and J. Kitching, "Demonstration of high-performance compact magnetic shields for chip-scale atomic devices", *Review of Scientific Instruments*, vol. 78, no. 8, p. 083 102, 2007 (page 59).

[110] Z. Sun, A. Schnabel, M. Burghoff, and L. Li, "Calculation of an optimized design of magnetic shields with integrated demagnetization coils", *AIP Advances*, vol. 6, p. 075 220, 2016 (page 59).

[111] D. Cohen, "Magnetocardiograms taken inside a shielded room with a superconducting point-contact magnetometer", *Applied Physics Letters*, vol. 16, no. 7, 1970 (page 59).

[112] K. Harakawa, G. Kajiwara, K. Kazami, H. Ogata, and H. Kado, "Evaluation of a high-performance magnetically shielded room for biomagnetic measurement", *IEEE Transactions on Magnetics*, vol. 32, no. 6, 1996 (page 59).

[113] A. K. Thomas, "Magnetic shielded enclosure design in the DC and VLF region", *IEEE Transactions on Electromagnetic Compatibility*, vol. EMC-10, no. 1, pp. 142–152, 1968 (page 59).

[114] *Mag-03® Three-Axis Magnetic Field Sensors - Brochure*, DS0013, Bartington Instruments Limited, 2018 (pages 59, 95).

[115] V. V. Yashchuk, S.-K. Lee, and E. Paperno, "Magnetic shielding", in *Optical Magnetometry*, D. Budker and D. F. J. Kimball, Eds. Cambridge: Cambridge University Press, 2013, pp. 225–248 (page 59).

[116] V. Kuhlmann, A. Sinton, M. Dewe, and C. Arnold, "Effects of sampling rate and ADC width on the accuracy of amplitude and phase measurements in power-quality monitoring", *IEEE Transactions on Power Delivery*, vol. 22, no. 2, 2007 (page 62).

[117] J.-G. Liu, U. Fruehauf, and A. Schoenecker, "Accuracy improvement of impedance measurements by using the self-calibration", *Measurement*, vol. 25, no. 3, p. 213, 1999 (pages 62, 69).

[118] F. Overney and B. Jeanneret, "Calibration of an LCR-meter at arbitrary phase angles using a fully automated impedance simulator", *IEEE Transactions on Instrumentation and Measurement*, vol. 66, no. 6, 2017 (page 62).

[119] Q. S. H. Chui, "Uncertainties related to linear calibration curves: A case study for flame atomic absorption spectrometry", *Journal of the Brazilian Chemical Society*, vol. 18, no. 2, pp. 424–430, 2007 (page 63).

[120] *NI 6221 (37-Pin) Device Specifications*, National Instruments, 2016 (page 65).

[121] I. Farrance and R. Frenkel, "Uncertainty of measurement: A review of the rules for calculating uncertainty components through functional relationships", *The Clinical Biochemist Reviews*, vol. 33, no. 2, p. 49, 2012 (pages 66, 70).

[122] *Evaluation of measurement data - Guide to the expression of uncertainty in measurement*, Joint Committee for Guides in Metrology (JCGM), 2008 (page 66).

[123] *Keysight 34401A 6 1/2 Digit Multimeter Service Guide*, Keysight Technologies, 2014 (pages 66–67).

[124] *Agilent 4294A Precision Impedance Analyzer Technical Overview*, Agilent Technologies Inc., 2004 (pages 70–71).

[125] L. C. C. Benyosef *et al.*, "Optimization of the magnetic properties of materials for fluxgate sensors", *Materials Research*, vol. 11, no. 2, p. 145, 2008 (page 71).

[126] W. Jiang, Y. Shi, W. Zhao, and X. Wang, "Parameters identification of fluxgate magnetic core adopting the biogeography-based optimization algorithm", *Sensors*, vol. 16, no. 7, p. 979, 2016 (page 71).

[127] R. Valenzuela, "Inductance spectroscopy", in *Advanced Topics in Materials Science and Engineering*. Boston, MA: Springer US, 1993, p. 187 (page 72).

[128] S. Motoasca *et al.*, "Improved evaluation of losses in soft magnetic material", *Bulletin of the Transilvania*, vol. 2, no. 51, 2009 (page 72).

[129] K. M. Chowdary and S. A. Majetich, "Frequency-dependent magnetic permeability of Fe10Co90 nanocomposites", *Journal of Physics D: Applied Physics*, vol. 47, p. 175 001, 2014 (page 72).

[130] *Agilent 4294A Precision Impedance Analyzer Data Sheet*, Agilent Technologies Inc., 2008 (page 73).

[131] P. Ripka, "Race-track fluxgate with adjustable feedthrough", *Sensors and Actuators A: Physical*, vol. 85, pp. 227–231, 2000 (pages 73, 75).

[132] S. Yang, S. Liu, W. Feng, B. Guo, X. Hou, and J. Li, "SPICE circuit model of voltage excitation fluxgate sensor", *IET Science, Measurement and Technology*, vol. 7, no. 3, pp. 145–150, 2013 (page 76).

[133] R. N. Setiadi and M. Schilling, "Inductance analyzer based on autobalanced circuit for precision measurement of fluxgate impedance", *Measurement Science and Technology*, vol. 29, no. 5, p. 055 007, 2018 (pages 79, 81–82).

[134] R. Hilzinger and W. Rodewald, *Magnetic materials*. Erlangen, Germany: Publicis Publishing, 2013 (pages 79, 82).

[135] O. V. Nielsen, J. R. Petersen, F. Primdahl, P. Brauer, B. Hernando, A. Fernández, J. M. G. Merayo, and P. Ripka, "Development, construction and analysis of the 'Ørsted' fluxgate magnetometer", *Measurement Science and Technology*, vol. 6, pp. 1099–1115, 1995 (page 90).

[136] *Sensys FGM3D Matrix of Technical Parameters*, Version 1.03, Sensys Sensorik & Systemtechnologie GmbH, 2018 (page 95).

Own Publications and Presentations

Publications in Journal

R. N. Setiadi and M. Schilling, "Inductance analyzer based on auto-balanced circuit for precision measurement of fluxgate impedance", in *Measurement Science and Technology*, vol. 29, no. 5, p. 055007, 2018

R. N. Setiadi and M. Schilling, "Sideband sensitivity of fluxgate sensors theory and experiment", in *Sensors and Actuators A: Physical*, vol. 285, p. 573-580, 2019

Presentations in Poster

R. N. Setiadi, F. Ludwig, and M. Schilling, "Optimization and Characterization of Fluxgate Sensor", *International Summer School on Metrology*, 2015, Drübeck

R. N. Setiadi, F. Ludwig, and M. Schilling, "Sensitivity and Noise Properties of Fluxgate Sensor", *Summer School on Nanometrology*, 2016, Drübeck

R. N. Setiadi, F. Ludwig, and M. Schilling, "Fluxgate Magnetic Sensor Properties", *International Summer School on Metrology*, 2017, Drübeck